

AN ABSTRACT OF THE THESIS OF

Joseph W. Ku for the degree of Doctor of Philosophy in Electrical and Computer Engineering presented on June 12, 1981.

Title: Defects and Transport Properties in $\text{In}_{1-x}\text{Ga}_x\text{As}_y\text{P}_{1-y}$ and

$\text{Ga}_{1-x}\text{Al}_x\text{As}$ *Redacted for Privacy*
Abstract Approved: *Redacted for Privacy*

() Dr. S.J.T. Owen

The electrical and optical properties of the III-V semiconductor alloys $\text{In}_{1-x}\text{Ga}_x\text{As}_y\text{P}_{1-y}$ and $\text{Ga}_{1-x}\text{Al}_x\text{As}$, grown by liquid-phase and vapor-phase epitaxial techniques, have been investigated by different measurement techniques. Several electron and hole traps, with activation energies, ΔE_T , varying from 0.26 to 0.82 eV, have been detected in $\text{In}_{1-x}\text{Ga}_x\text{As}_y\text{P}_{1-y}$ by transient capacitance and photocapacitance measurements. The density and capture cross section of the traps were measured. In particular, electron trapping centers with $\Delta E_T = 0.82$ eV have emission and capture properties identical to the dominant 0.83 eV electron trap present in bulk and VPE GaAs and are probably associated with a Ga vacancy. Hall measurements were performed on the same quaternary crystals in the temperature range 20-600°K. The temperature dependence of the Hall mobility and carrier concentration were measured as a function of crystal composition. Analysis of the mobility data has yielded values of several transport parameters, including the alloy scattering potential ΔU , as a function of composition. The maximum value of $\Delta U \approx 0.8$ eV corresponding to a band gap $E_g \approx 0.95$ eV. Photo-Hall measurements at low temperatures show the presence of donor- and acceptor-like defects

in the LPE and VPE alloys, respectively. These centers exhibit persistent photoconductivity at low temperatures and have a high barrier energy (~ 0.2 eV) associated with electron capture. Defects, which are possibly located in the interconduction valley region, have been identified from analyses of the mobility and concentration data for $T \geq 350^\circ\text{K}$.

The electrical properties of nonintentionally doped LPE $\text{Ga}_{1-x}\text{Al}_x\text{As}$ are dominated by nonshallow defect levels which behave as electron trapping centers. Optical lineshape, thermally stimulated capacitance, and Hall measurements have been performed to investigate and understand the existing differences between the properties of these defects and similar defects reported to be present in intentionally doped crystals. The experimental results show that the defect centers exhibit a large Stokes shift with a Franck-Condon energy $d_{\text{FC}} = 0.75 \pm 0.05$ eV, and strong persistent photoconductivity which can only be quenched thermally. The thermal binding energy $E_0 = 0.12 \pm 0.05$ eV obtained from lineshape analysis agrees fairly well with Hall-effect data and both disagree with the activation energy in the direct band gap region. Interpretation of photo-Hall data indicates that the defect centers are acceptor-like, in sharp contrast to the donor-like behavior exhibited in intentionally doped crystals. Large lattice relaxation associated with the observed Stokes shift accounts for the persistent photoconductivity. A model has been proposed in which the most likely microstructure of the defect in the nonintentionally doped crystals is an impurity-vacancy complex. The vacancies are most probably in the anion sublattice, V_{As} , while the impurity is thought to be C.

Defects and Transport Properties in
 $\text{In}_{1-x}\text{Ga}_x\text{As}_y\text{P}_{1-y}$ and $\text{Ga}_{1-x}\text{Al}_x\text{As}$

by

Joseph W. Ku

A THESIS

submitted to

Oregon State University

in partial fulfillment of
the requirements for the
degree of

Doctor of Philosophy

Commencement June 1982

APPROVED:

Redacted for Privacy

Professor of Electrical & Computer Engineering
in charge of major

Redacted for Privacy

Head of Department of Electrical & Computer Engineering

Redacted for Privacy

Dean of Graduate School

Date thesis is presented June 12, 1981

Typed by Laurie Campbell for Joseph W. Ku

ACKNOWLEDGEMENTS

I wish to express my deep gratitude to Professor P.K. Bhattacharya and Professor S.J.T. Owen, my co-major advisors, for their guidance and encouragement. I would also like to express my sincere appreciation to J.K. Rhee, my associate, for his help in the laboratory. I am indebted to Laurie Campbell for her excellent typing.

Finally, I wish especially to thank my wife, Esther Yu-Tsuan, for her patience, encouragement and assistance in many ways.

TABLE OF CONTENTS

I.	INTRODUCTION	1
II.	THEORETICAL CONSIDERATIONS	11
	2.1 Characteristics of Deep Levels	11
	2.1.1 Recombination and Trapping at Deep Levels	11
	2.1.2 Theory of the Thermal Capture Process	15
	2.1.3 Theory of Thermal Emission from Traps	17
	2.1.4 Theory of Electron Photoionization Cross Section Spectrum	23
	2.2 Theory of Transport Measurements	26
III.	EXPERIMENTAL TECHNIQUE	31
	3.1 Material Description	31
	3.2 Fabrication of Schottky Diodes on Epitaxial Layers	32
	3.2.1 Schottky Diodes on $\text{In}_{1-x}\text{Ga}_x\text{As}_y\text{P}_{1-y}$	32
	3.2.2 Schottky Diodes on $\text{Ga}_{1-x}\text{Al}_x\text{As}_y$	33
	3.3 Fabrication of van der Pauw Samples	33
	3.4 Transient Capacitance Measurements	33
	3.4.1 Trap Emission Measurement	33
	3.4.2 Trap Capture Measurements	37
	3.5 Thermally Stimulated Capacitance (TSCAP) Measurements	38
	3.6 Optical Lineshape Measurements	40
	3.7 Hall and Photo-Hall Effect Measurements	41
	3.8 Measurement of Photoconductivity Spectra	43
	3.9 Discussion	44
IV.	TRAPS IN $\text{In}_{1-x}\text{Ga}_x\text{As}_y\text{P}_{1-y}$	47
	4.1 Traps Identified From the Transient Capacitance Measurements	47
	4.1.1 Electron Traps	47
	4.1.2 Hole Traps	52
	4.2 Capture Measurements for the 0.83 eV Electron Trap	52
	4.3 Electron Traps Identified From Photoconductivity Spectrum	57
	4.4 Discussion	59
V.	TRANSPORT PROPERTIES IN $\text{In}_{1-x}\text{Ga}_x\text{As}_y\text{P}_{1-y}$	62
	5.1 Results of Hall Mobility and Carrier Concentration	62
	5.2 Analysis of Transport Data	70
	5.3 Discussion	79
VI.	DEFECT CENTERS IN LPE $\text{Ga}_{1-x}\text{Al}_x\text{As}$	81
	6.1 Review of the Defect Properties	81
	6.1.1 Electrical Properties	81
	6.1.2 Optical Properties	85

6.2	Experimental Results	86
6.2.1	Hall and Photo-Hall Measurements	86
6.2.2	Thermally Stimulated Capacitance Measurements	86
6.2.3	Electron Photoionization Cross Section	91
6.3	Analysis of Optical Lineshape Data	91
6.4	Discussion	97
6.5	Physico-Chemical Origin of the Defects	102
VII.	CONCLUSIONS	104
	REFERENCES	108
	APPENDICES	
	Appendix A	115
	Appendix B	129
	Appendix C	132

LIST OF FIGURES

<u>Figure</u>	<u>Page</u>
1.1 The band structure of GaAs at 300°K	2
1.2 Band gap versus lattice constant for the $\text{In}_{1-x}\text{Ga}_x\text{As}_y\text{P}_{1-y}$ alloy system	4
1.3 The conduction band structure of $\text{Ga}_{1-x}\text{Al}_x\text{As}$ as a function of Al content	8
2.1 Band diagram for a reverse biased Schottky barrier on an n-type semiconductor showing occupation of electron and hole traps in the steady state	13
2.2 Filling and emptying of electron traps	19
2.3 Filling and emptying of hole traps	21
2.4 Normalized photoionization cross section versus normalized photon energy calculated from Lucovsky's model	25
2.5 A van der Pauw sample of arbitrary shape	29
2.6 A van der Pauw sample of "clover-leaf" shape	29
3.1 Mounting of sample inside insulated chamber for capacitance measurements	35
3.2 Schematic diagram for transient capacitance measurements	36
3.3 Schematic diagram for thermally stimulated capacitance measurement	39
3.4 Schematic diagram for Hall and photo-Hall measurements	42
4.1 Transient capacitance measurement for electron traps in $\text{In}_{0.90}\text{Ga}_{0.10}\text{As}_{0.21}\text{P}_{0.79}$ crystal	48
4.2 Temperature dependence of emission time constant for electron traps in LPE and VPE $\text{In}_{1-x}\text{Ga}_x\text{As}_y\text{P}_{1-y}$	50
4.3 Transient capacitance measurements for hole traps in $\text{In}_{0.90}\text{Ga}_{0.10}\text{As}_{0.21}\text{P}_{0.79}$ crystal	53
4.4 Temperature dependence of emission time constant for hole traps in LPE and VPE $\text{In}_{1-x}\text{Ga}_x\text{As}_y\text{P}_{1-y}$	54
4.5 Temperature dependence of electron capture rates for 0.83 eV electron trap in GaAs and the 0.82 ± 0.01 eV electron trap in $\text{In}_{1-x}\text{Ga}_x\text{As}_y\text{P}_{1-y}$	56

<u>Figure</u>	<u>Page</u>
4.6 Spectral variation of photoconductivity at different temperatures	58
4.7 Dependence of the concentration of the dominant 0.82 ± 0.02 eV electron trap on the As/Ga ratio in OMVPE GaAs material	61a
5.1 Variation of the room-temperature electron mobility with band gap in $\text{In}_{1-x}\text{Ga}_x\text{As}_y\text{P}_{1-y}$	63
5.2 Variation of the room-temperature electron mobility with carrier concentration	64
5.3 Mobility versus temperature data for LPE and VPE samples in the low temperature region	65
5.4 Mobility versus temperature data in the high temperature region for (a) VPE samples (b) LPE samples	67
5.5 Hall carrier concentration as a function of reciprocal temperature for (a) LPE and (b) VPE quaternary samples	68
5.6 Mobility variation with temperature in LPE and VPE samples in the dark and upon photoexcitation	69
5.7 Temperature dependence of the decay time constant of the photoexcited carrier concentration assuming an exponential decay law	71
5.8 Hall scattering factor versus $\mu_d B$ in $\text{In}_{0.77}\text{Ga}_{0.23}\text{As}_{0.49}\text{P}_{0.51}$ ($E_g = 0.95$ eV)	73
5.9 Experimented and calculated mobilities as a function of temperature in $\text{In}_{0.67}\text{Ga}_{0.33}\text{As}_{0.71}\text{P}_{0.29}$	75
5.10 Variation of the alloy scattering potential with (a) band gap E_g , and (b) alloy composition y	76
6.1 The conduction band structure at 300°K and the energy position of defect levels in LPE $\text{Ga}_{1-x}\text{Al}_x\text{As}$	83
6.2 Variation of defect binding energy with composition in nonintentionally and intentionally doped crystals as determined by different workers	84
6.3 Variation of electron mobility with temperature	87
6.4 Thermally stimulated capacitance data for samples of nonintentionally doped LPE $\text{Ga}_{1-x}\text{Al}_x\text{As}$ with varying compositions	89

<u>Figure</u>	<u>Page</u>
6.5 Theoretical fit to the normalized electron photoionization cross section of the defect centers in LPE $\text{Ga}_{1-x}\text{Al}_x\text{As}$ with $x = 0.32, 0.34, 0.36$ using Lucovsky's model	93
6.6 Theoretical fit to the normalized electron photoionization cross section of the defect centers in LPE $\text{Ga}_{1-x}\text{Al}_x\text{As}$ with $x = 0.47, 0.50, 0.78$ using Lucovsky's model	94
6.7 Theoretical fit to the normalized electron photoionization cross section of the defect centers in LPE $\text{Ga}_{1-x}\text{Al}_x\text{As}$ with $x = 0.32$ using the Huang and Rhys model	95
6.8 Theoretical fit to the normalized electron photoionization cross section of the defect centers in LPE $\text{Ga}_{1-x}\text{Al}_x\text{As}$ with $x = 0.50$ using the Huang and Rhys model	96
6.9 Models to explain the measured binding energy, E_0 , the thermal activation energy, ΔE_T , and the optical ionization energy, E_n , of the defects in (a) direct band gap, and (b) indirect band gap nonintentionally doped LPE $\text{Ga}_{1-x}\text{Al}_x\text{As}$	100
6.10 Configuration coordinate diagrams for the defects in (a) direct band gap, and (b) indirect band gap nonintentionally doped LPE $\text{Ga}_{1-x}\text{Al}_x\text{As}$	101
B.1 Variation of electron density-of-state effective mass with Al content in the conduction minima of $\text{Ga}_{1-x}\text{Al}_x\text{As}$	131

LIST OF SYMBOLS

B	Magnetic flux density (Tesla)
$C(t)$	Instantaneous depletion layer capacitance (F)
C_0, C_∞	Depletion layer capacitance at $t=0, \infty$ (F)
c_n^t, c_p^t	Thermal capture rate for electron and hole (s^{-1})
c_n^o, c_p^o	Optical capture rate for electron and hole (s^{-1})
d	Thickness of epitaxial layer (μm)
d_{FC}	Franck-Condon shift (eV)
E_{DP}	Deformation potential (eV)
E_F, E_{FM}	Fermi energy in semiconductor (bulk), metal (eV)
E_c, E_v	Energy corresponding to conduction band edge, valence band edge (eV)
E_Γ, E_L, E_X	Energy measured from valence band edge to Γ conduction minimum, L minima, X minima (eV)
E_g	Energy gap (eV)
E_p	Average optical gap (eV)
E_T	Energy depth with respect to band edges (eV)
E_n	Optical ionization energy
E_A	Acceptor ionization energy (eV)
E_o	Binding energy (eV)
$\Delta E_T^o, \Delta E_T$	Thermal activation energy at $T=0, T$ (eV)
ΔE_B	Energy associated with deep level (eV)
$\Delta E_{\Gamma L}$	Energy separation between conduction band minimum of Γ and L (eV)
e_n^t, e_p^t	Thermal emission rate of electron and hole
e_n^o, e_p^o	Optical emission rate of electron and hole

e_{14}	Piezoelectric constant (coul./m ⁻²)
g_n, g_p	Spin degeneracy factor for electrons and holes.
h, \hbar	Planck's constant (6.625×10^{-27} erg s) reduced Planck's constant ($h/2\pi$)
k	Boltzmann's constant (1.38×10^{-16} erg k ⁻¹)
L_D	Debye length (μm)
M_c	Number of equivalent minima in the conduction band.
m_o, m_c, m_d	Free electron mass (9.11×10^{-28} g), conductivity mass for electrons, density of states mass for elec- trons (g)
m_p^*	Effective mass for holes (g)
m_T	Mass of bound electrons (g)
N_c	Effective density of state in conduction band (cm ⁻³)
N_T, N_T^+	Total trap density, ionized electron trap density (cm ⁻¹)
N_D, N_A	Shallow donor, acceptor density (cm ⁻³)
n, p	Electron concentration in conduction band, hole concentration in valence band (cm ⁻³)
n_T	Concentration of the occupied traps (cm ⁻³)
$p_t(o)$	Hole population in the hole trap when $t=0$
q	Electronic charge (1.6×10^{-19} coul.)
R_H	Hall coefficient (cm ³ .coul ⁻¹)
T	Temperature ($^{\circ}\text{K}$)
t_f	Trap filling time (s)
ΔU	Alloy scattering potential (eV)
v_{th}	Electron thermal velocity (cm.s ⁻¹)
W	Depletion layer width (μm)

α	Temperature coefficient of thermal activation energy (eV·(K ⁻¹))
$h\nu$	Photon energy (eV).
$\hbar\omega$	Phonon energy (eV)
θ	Optical phonon temperature (K)
ϵ_0, ϵ_r	Free space permittivity (8.854 x 10 ⁻¹⁴ F cm ⁻¹) di- electric constant
$\phi(h\nu)$	Light intensity (photons·cm ⁻¹ ·s ⁻¹)
ϕ_b	Metal-semiconductor barrier height (V)
σ_n^t, σ_p^t	Thermal capture cross section of electrons, holes (cm ²)
σ_n^o, σ_p^o	Optical capture cross section of electrons, holes (cm ²)
$\sigma_{n^\infty}, \sigma_{p^\infty}$	Thermal capture cross section of electrons, holes at T=∞ or the capture cross section for carrier emission (cm ²)
τ_n, τ_p	Thermal emission time constant of electrons, holes (s)
τ_n^o, τ_p^o	Optical emission time constant of electrons, holes (s)
λ	The distance from metal-semiconductor surface to the point where Fermi-level crossing over trap level in the band diagram of a Schottky diode (μm)
μ_H	Hall mobility (cm ² ·V ⁻¹ ·s ⁻¹)
μ_d	Drift mobility (cm ² ·V ⁻¹ ·s ⁻¹)
ρ	Specific resistivity (Ω-cm)

DEFECTS AND TRANSPORT PROPERTIES IN $\text{In}_{1-x}\text{Ga}_x\text{As}_y\text{P}_{1-y}$
AND $\text{Ga}_{1-x}\text{Al}_x\text{As}$

CHAPTER I

INTRODUCTION

Although the discovery of the semiconducting properties of the III-V compound InSb was made in the early 50's, detailed investigation of the fundamental properties of compound semiconductors has not been undertaken until it was recognized that such properties could be utilized in microwave and optoelectronic devices. The particular features of III-V compound semiconductors which attracted interest were the small effective mass of carriers, direct band structure, and the possibility of forming alloys. For example, a small electron effective mass and consequent high electron mobility enables the realization of high-speed microwave devices such as the Metal-Epitaxy-Semiconductor Field Effect Transistor (MESFET)⁽¹⁾. A direct band structure, such as the one for GaAs shown in Figure 1.1, results in high quantum efficiencies in optoelectronic devices such as a Light Emitting Diode (LED). In addition, the direct band structure allows the transfer of "hot" electrons from the central conduction minimum Γ , where the effective mass is small, to satellite minima L or X, where the effective masses are about 9-10 times larger. The transfer electron effect results in the reduction of carrier velocity, eventually leading to Gunn oscillations in planar devices⁽²⁾. Semiconducting alloys can be formed from the binary compounds by replacing a known percentage of the host atoms from their sublattice sites with the elements of the same group in the

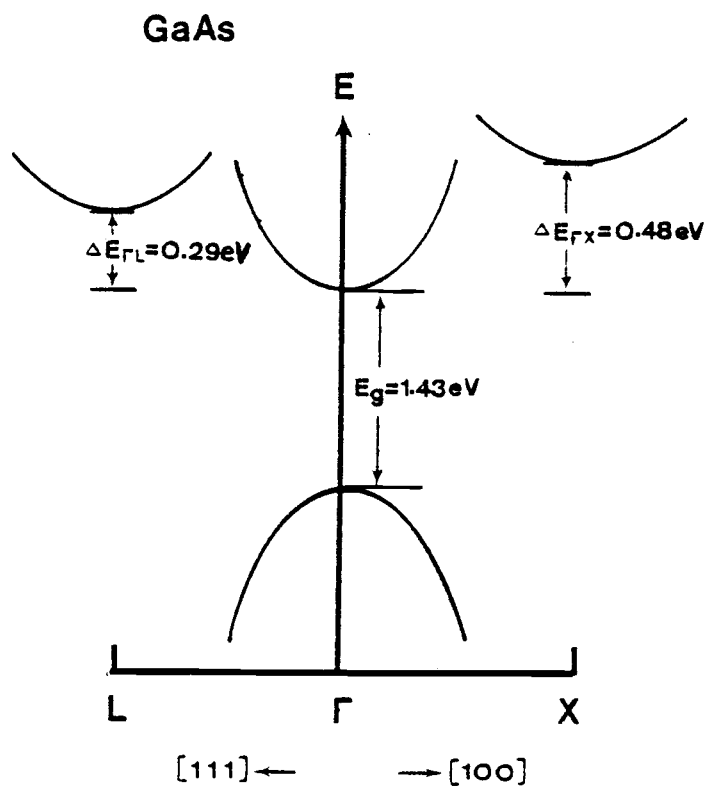


Figure 1.1. The band structure of GaAs at 300°K ($E_g = 1.425 \text{ eV}$).

periodic table. Binary, ternary and quaternary compound semiconductors have direct band gaps covering a wide spectral range from InSb (0.16 eV) to $\text{In}_{0.27}\text{Ga}_{0.73}\text{P}$ (2.21 eV). Some of these compounds are useful for the fabrication of semiconductor lasers⁽³⁾, LEDs⁽⁴⁾, and solar cells⁽⁵⁾. The dependence of the band gap on the lattice constant for the constituent binary compounds is shown in Figure 1.2. In alloy systems such as $\text{Ga}_{1-x}\text{Al}_x\text{As}$ and $\text{GaAs}_{1-x}\text{P}_x$, the band structure can be varied continuously from a direct to an indirect energy gap by varying the mixed crystal composition. Such compounds can be successfully grown on binary substrates due to minimal lattice mismatch with the substrate materials.

Growth and fabrication of heterostructure devices impose stringent requirements on substrate and active layer growth. Novel techniques of crystal growth, such as Organometallic Vapor Phase Epitaxy (OMVPE)⁽⁶⁾ and Molecular Beam Epitaxy (MBE)⁽⁷⁾, are being widely used in addition to bulk growth⁽⁸⁾, Liquid Phase Epitaxy (LPE)^(9,10), and conventional Vapor Phase Epitaxy (VPE)⁽¹¹⁾.

The application of III-V semiconductors in the field of fiber-optical communication has recently received considerable attention. Silica optical fibers have minimal transmission loss⁽¹²⁾ and minimal dispersion⁽¹³⁾ in the spectral range 1.3 to 1.55 μm . It is clear from Figure 1.2 that the optimal spectral range for optical fiber communication closely matches the band gap range of $\text{In}_{1-x}\text{Ga}_x\text{As}_y\text{P}_{1-y}$ alloys grown on InP substrates. Burnham, et al.⁽¹⁴⁾ have shown that it is possible to vary the energy gap of a semiconductor and still maintain a completely lattice matched system with the substrate by utilizing alloyed quaternary layers. Heterostructure sources and detectors utilizing the $\text{In}_{1-x}\text{Ga}_x\text{As}_y\text{P}_{1-y}/\text{InP}$ alloy system are therefore being grown and fabri-

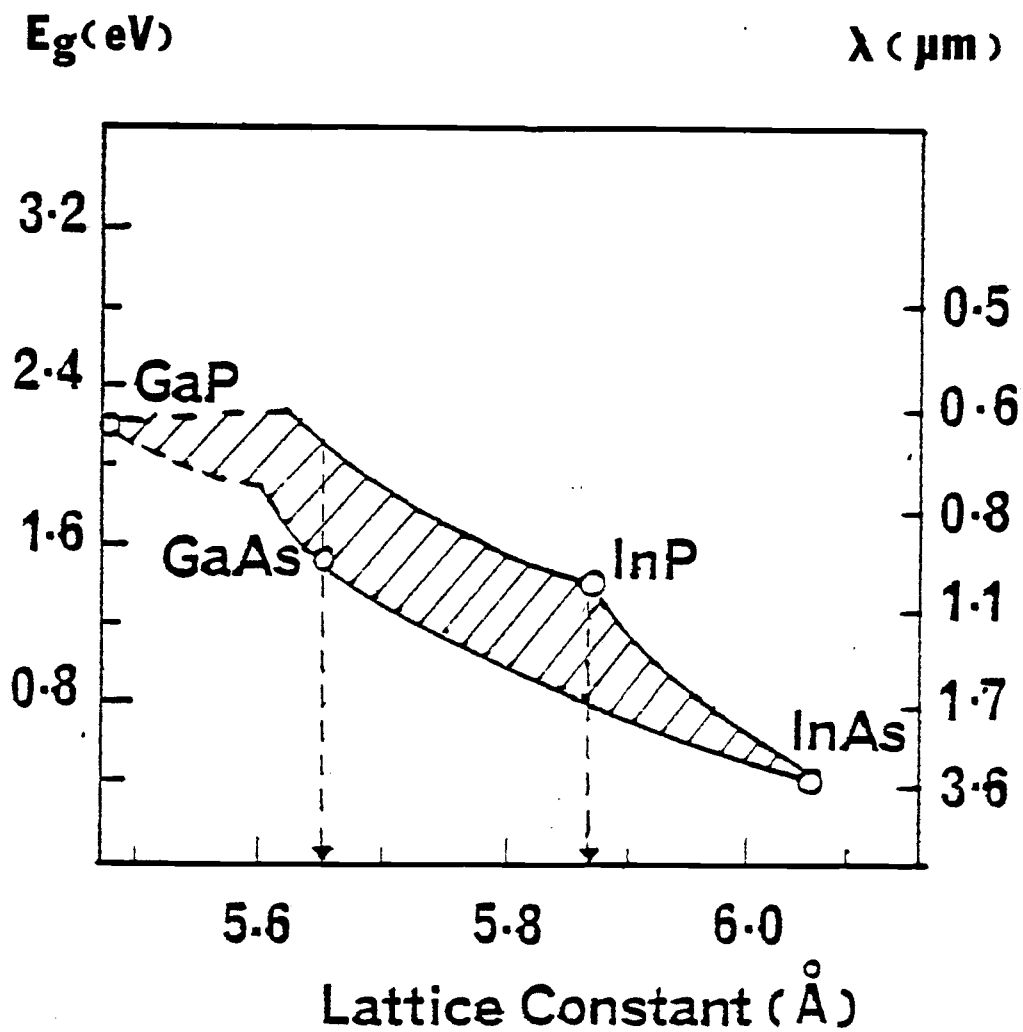


Figure 1.2. Band gap versus lattice constant for the $\text{In}_{1-x}\text{Ga}_x\text{As}_y\text{P}_{1-y}$ quaternary alloy system. The dotted lines within the shaded regions correspond to the quaternary compositions lattice-matched to GaAs and InP.

cated in several laboratories. However, the electrical and optical properties of these materials have not been investigated in detail and there is a need to resolve or understand significant discrepancies between the results obtained by some early workers. The low-field and high-field transport properties of the quaternary alloys have been predicted from Monte Carlo calculations by Littlejohn, et al.⁽¹⁵⁾. The compositional dependence of the band gaps have been determined by Nahory, et al.⁽¹⁶⁾. The effective masses of carriers have been determined by Nicholas, et al.^(17,18). The low-field transport properties of the alloys as a function of composition have been determined by Leheny, et al.⁽¹⁹⁾ for LPE grown crystals, but their experimental results are not in good agreement with the theoretical predictions of Littlejohn, et al.⁽¹⁵⁾. Similarly the electron mobilities in LPE crystals, as reported by Greene, et al.⁽²⁰⁾, are lower than the theoretical values. Anomaly also exists in the literature regarding the value of the alloy scattering potential, ΔU , which is a measure of the randomness of the alloy constituents. The values of ΔU determined from Hall-effect data for two compositions ($E_g = 0.98$ and 1.00 eV) by Greene, et al.⁽²⁰⁾ are different from those calculated and estimated by Littlejohn, et al.^(21,22) for the same compositions.

Defects in the material which can give rise to deep trapping centers in the forbidden energy gap, and other inhomogeneous defects such as clusters in the lattice, significantly affect the electrical properties of a semiconducting material and produce deleterious effects in devices. It has been reported that the increased junction leakage in avalanche photodiodes⁽²³⁾ and the temperature dependence in the performance of double heterostructure lasers⁽²⁴⁾ might be related to such

defects.

Thus, it was felt that a detailed investigation of the transport properties, and identification and characterization of defects in the $\text{In}_{1-x}\text{Ga}_x\text{As}_y\text{P}_{1-y}$ alloys would lead to a better understanding of the material properties, improved crystal growth, and more reliable device performance.

The mixed alloy composition of the LPE and VPE layers investigated in the course of this work varied from $\text{In}_{0.53}\text{Ga}_{0.47}\text{As}$ ($E_g = 0.75$ eV) to InP ($E_g = 1.35$ eV). Hall measurements were made on the samples using the van der Pauw method⁽²⁵⁾ over the temperature range 20-600°K. Photo-Hall measurements were performed at low temperatures with band gap and sub-band gap (0.7 eV) filtered light. The temperature variation of the mobility for various crystal compositions were analyzed in detail to determine the relative importance of the various mobility limiting scattering mechanisms. The variation of the alloy scattering potential with composition has been determined and the results have been explained. The results of photo-Hall measurements indicate the presence of donor-like and acceptor-like defect centers in the VPE and LPE materials, respectively, which exhibit persistent photoconductivity below 100°K. Anomalous behavior in the crystals at temperature greater than 300°K have been observed from Hall measurements. A significant change in the slope of the temperature variation of electron mobility for $T > 400^\circ\text{K}$ has been observed in both VPE and LPE samples with band gaps $E_g = 0.9$ to 1.0 eV. The sharp fall in the electron mobility was not observed for layers with higher or lower energy band gaps. A model considering electron transfer from the central Γ valley to a localized defect level with high density of states, situated in the intervalley region, has been proposed. Such defect levels are thought to be related to in-

homogeneous clusters⁽²⁴⁾ in the lattice.

Trap levels in the alloys were detected and characterized by transient capacitance, photocapitance, and carrier-capture measurements on Schottky diodes made on the epitaxial layers. Thin interfacial oxide films were used⁽²⁶⁾ to enhance the barrier height of these materials. The significant result obtained is the presence of a deep electron trap with an activation energy of 0.82 eV in some n-type LPE and VPE layers. The emission and capture properties of this center are identical with those of the dominant 0.83 eV electron trap observed in bulk and VPE GaAs⁽²⁷⁾. Transitions involving the same center have been identified in the photoconductivity spectra. In order to study the origin of the 0.83 eV electron trap, organometallic VPE GaAs, in which the center is also dominant, with varying As/Ga ratios was investigated⁽²⁸⁾. A linear dependence of the trap concentration on As/Ga ratio in the material which indicates the involvement of a Ga vacancy in the formation of the center.

Ternary semiconducting alloys also have a wide range of applications in heterostructure optoelectronic and microwave devices. The $\text{Ga}_{1-x}\text{Al}_x\text{As}$ alloy system is important technologically and its material properties have been extensively investigated. The band structure of the alloys as a function of composition has now been fairly well documented as shown in Figure 1.3. The alloys have a direct band gap for $0 \leq x \leq 0.43$ and an indirect band gap for $x > 0.43$, where the X conduction minima are lowest in energy. In addition, the L conduction minima crossover with the X minima at $x = 0.37$ and with the Γ minimum at $x = 0.47$. Such a dramatically changing band structure has a marked influence on the electrical and optical properties of the alloy system.

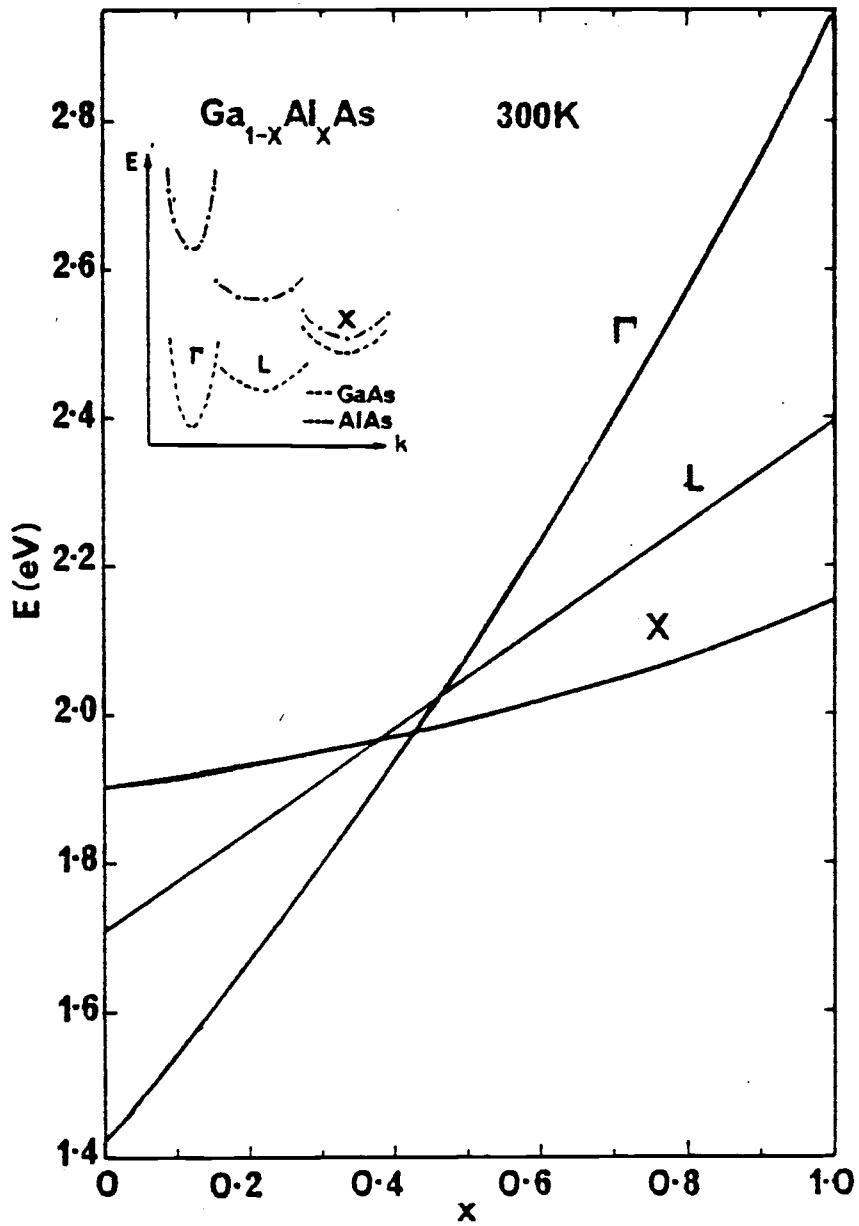


Figure 1.3. The conduction band structure of $\text{Ga}_{1-x}\text{Al}_x\text{As}$ as a function of Al content.⁽³⁹⁾

A feature which is rather unique in the ternary $\text{Ga}_{1-x}\text{Al}_x\text{As}$ crystals grown by LPE is the emergence of a nonshallow defect level which dominates the electrical properties of the alloys with $x \geq 0.25$. Similar levels have not been observed in $\text{Ga}_{1-x}\text{Al}_x\text{As}$ grown by VPE⁽²⁹⁾ or MBE⁽³⁰⁾. It has been suggested from experimental evidence⁽³¹⁾ that these centers are the prime source of point defects for $\langle 100 \rangle$ dark-line defect formation, which leads to degradations in heterostructure laser performance. Bhattacharya, et al.⁽³²⁾ have shown that the centers, unlike similar ones in the $\text{GaAs}_{1-x}\text{P}_x$ alloys, are nonradiative. Capacitance-voltage measurements on Schottky diodes and Hall-effect measurements on van der Pauw samples confirm that in most cases the concentration of the nonshallow centers, which act as electron traps, is equal to or greater than the shallow donor density in the crystals.

Although the general features of the nonshallow defects are very similar in nonintentionally and intentionally doped LPE $\text{Ga}_{1-x}\text{Al}_x\text{As}$, some differences have been observed in their electrical properties. It is believed that these differences are related to the physico-chemical origin of the centers. In this study, the optical lineshapes of the defects in nonintentionally doped LPE $\text{Ga}_{1-x}\text{Al}_x\text{As}$ have been measured and analyzed. Hall and Photo-Hall measurements have also been made on the same crystal, in order to provide a further basis to understand the difference in the properties of the same (or related) centers observed by several workers. Finally, a model for the microstructure of the defect has been proposed to explain the experimental results.

The theoretical considerations are presented in Chapter II. The experimental techniques will be described in Chapter III. Results related to trap levels in $\text{In}_{1-x}\text{Ga}_x\text{As}_y\text{P}_{1-y}$ quaternary compounds and the

analysis of these results are presented in Chapter IV. Carrier transport data in quaternary compounds and the analysis and discussion based on these results are presented in Chapter V. The experiment and analytical studies related to the defect centers in LPE $\text{Ga}_{1-x}\text{Al}_x\text{As}$ are included in Chapter VI. Some concluding remarks and suggestions for future work are summarized in Chapter VII.

CHAPTER II

THEORETICAL CONSIDERATIONS

Transient spectroscopy and transport measurements are important techniques to characterize the properties of a semiconductor material. In this chapter, the theory of these measurements are briefly reviewed and the limitations associated with them are discussed.

2.1 Characteristics of Deep Levels

Deep levels are usually located in the forbidden energy gap of a semiconductor at an energy position of more than about 0.1 eV from either band edge and are not significantly thermally ionized at room temperature. Deep levels are usually caused by defects in the crystal such as vacancies, interstitials, substitutional impurities or impurity-vacancy complexes. In compound semiconductors, additional antisite defects may be formed when atoms of one kind substitute for the other. Deep levels act as carrier recombination centers or traps in a semiconductor.

2.1.1 Recombination and Trapping at Deep Levels

Carrier recombination in a semiconductor can either be an intrinsic or an extrinsic process. In the latter case, recombination occurs at a deep level in the forbidden energy gap. The excess energy may be dissipated by photons, excitons, phonons, Lax⁽³³⁾ or Auger⁽³⁴⁾ processes, or combinations of these mechanisms. Deep levels can act as electron or hole trapping centers according to their charge state before and after capturing an electron or a hole. The convention normally used is listed

in Table 2.1. The parameters which specify the behavior of any particular center are:

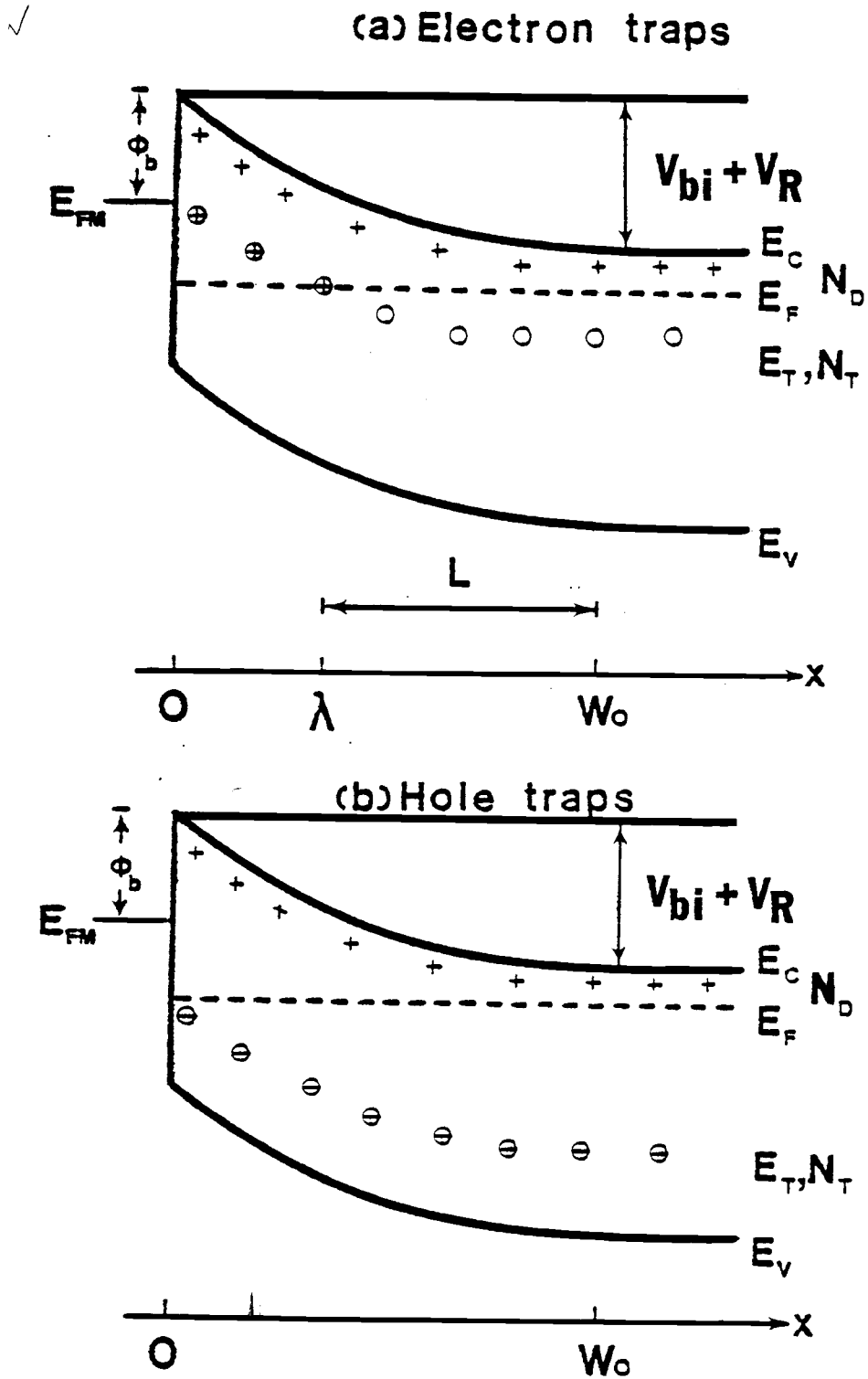
- (a) Its energy depth E_T with respect to the band edge.
- (b) Its energy barrier ΔE_B associated with carrier capture.
- (c) Its optical threshold energy E_n with respect to the band edge.
- (d) Its thermal and optical capture cross sections for electrons, σ_n^t , σ_n^o , and for holes, σ_p^t , σ_p^o , respectively.
- (e) Its thermal and optical emission rates for electrons, e_n^t , e_n^o , and for holes, e_p^t , e_p^o , respectively.
- (f) Its thermal and optical capture rate for electrons, c_n^t , c_n^o , and for holes, c_p^t , c_p^o , respectively.

The role of a center depends on the charge state, relative occupation by electrons and holes, and the relative capture cross sections for electrons and holes.

Table 2.1. Charge State of Deep Levels

	Full	Empty
Electron Trap	Neutral	Positive
Hole Trap	Negative	Neutral

The band diagram of a Schottky barrier on n-type material under reverse bias condition is shown in Figure 2.1(a) and (b). The charge state of electron and hole traps are indicated in this figure. There are two important features associated with the use of a reverse biased Schottky diode to characterize deep levels. First, the relatively high electric field present sweeps away any mobile carriers which may be generated by trap emptying and thus removes the complication of possible retrapping. Second, carrier trapping and detrapping change the total



charge content within the depletion layer and this may be detected as a change in depletion-layer capacitance.

Under thermal equilibrium conditions, the steady state occupation function of a single level without photoexcitation is governed by the Schokley-Read-Hall recombination equation^(35,36)

$$f_T = \frac{c_n^t e_n^t + c_p^t e_p^t}{c_n^t e_n^t + c_p^t e_p^t + c_p^t e_n^t + c_n^t e_p^t} \quad (2.1)$$

This equation can be simplified in the case of a Schottky diode as shown in Figure 2.1. In the depletion region $n=p=0$, Eqn. (2.1) becomes

$$f_T = \frac{e_p^t}{e_p^t + e_n^t} \quad (2.2)$$

- (i) for an electron trap $e_n^t \gg e_p^t$ and within the region $0 < x < \lambda$ at equilibrium,

$$f_T = 0 \quad (2.3)$$

Thus all the traps are ionized whereas in the region $\lambda < x < w$, the trap level is below the Fermi level, so they are full.

- (ii) for a hole trap $e_p^t \gg e_n^t$ and

$$f_T = 1 \quad (2.4)$$

Hole traps are filled with electrons everywhere.

2.1.2 Theory of the Thermal Capture Process

The thermal capture rate of electrons by deep levels can be expressed by the equation,

$$c_n^t = n \sigma_n^t v_{th} \quad (2.5)$$

where n is the electron concentration in a conduction minimum, $v_{th} = (3kT/m_c)^{1/2}$ is the thermal velocity of carriers, and m_c is the conductivity effective mass for electrons. Capture cross sections are usually temperature dependent and can be expressed as

$$\sigma_n^t = \sigma_{n,\infty} \exp(-\Delta E_B/kT) \quad (2.6)$$

where $\sigma_{n,\infty}$ is the capture cross section at $T = \infty$, and ΔE_B is the energy barrier associated with the deep center. The capture cross section, $\sigma_{n,\infty}$, is strongly dependent on the charge state of the center, as indicated in Table 2.2. An attractive center has a much larger cross section than an initially neutral center which, in turn, has a much larger cross section than a repulsive center. Several models have been proposed to explain trapping by centers of different cross sections. In a model postulated by Lax⁽³³⁾,

Table 2.2. Order of Magnitude of Capture Cross Section for Deep Centers.

Center Type	$\sigma_{n(p),\infty}$ (cm ²)
Attractive	$>10^{-14}$
Neutral	$10^{-16} - 10^{-17}$
Repulsive	$<10^{-19}$

electrons are captured by traps of large cross section through a cascade of excited states, emitting a phonon at every step. This theory is applicable only to relatively shallow centers with closely spaced excited states between which single phonons can be emitted in a cascade of electronic transitions. In the case of neutral and repulsive centers which do not have excited states, multiphonon emission (MPE) is the only possible mechanism other than Auger and optical processes. An MPE model has been proposed by Lang and Henry⁽³⁷⁾, in which electron capture results from large lattice vibrations. Such vibrations cause the trap level to cross into the conduction band and capture an electron. Immediately after capture the lattice equilibrium position changes in a way that leaves the captured carrier in a highly excited vibrational state which rapidly decays by the emission of lattice phonons.

In a typical thermal capture measurement the capture rate of the traps at different temperature is measured. At each temperature, the traps are filled by varying amounts by injection pulses of varying durations. Assuming an exponential capture process, the thermal capture rate, $c_{n,(p)}^t$ can be theoretically estimated by the relation:

$$\Delta C(\infty) - \Delta C(t_f) = \Delta C(\infty) \exp(-c_{n,(p)}^t t_f) \quad (2.7)$$

where $\Delta C(\infty)$ is the saturation value of the transient capacitance change for a large value of filling time, t_f , i.e., it is the maximum value of $\Delta C(t_f)$. ΔC can be measured accurately from the transient capacitance measurements. The electron capture rate at a particular temperature can be determined by the plot of $\ln(1 - \Delta C(t_f)/\Delta C(\infty))$ versus t_f and the corresponding values of σ_n^t may be determined by using Eqn. (2.5).

Thus the energy barrier, ΔE_B , may be obtained from the plot of $\ln \sigma_n^t$ versus $1/T$.

2.1.3 Theory of Thermal Emission from Traps

In thermal equilibrium, the thermal emission rate of electrons from deep levels to any conduction minima can be written as

$$e_n^t = \sigma_n^t v_{th} N_c \exp(-\Delta E_T/kT) \quad (2.8)$$

where $N_c = 2M_c (2\pi m_d kT/h^2)^{3/2}$ is the effective density of states in the conduction minima, M_c is the number of equivalent minima in the conduction band, m_d is the density of state effective mass, ΔE_T is the thermal activation energy of the deep level. Introducing a temperature coefficient of temperature dependence for the thermal activation energy depth, α , defined by $\Delta E_T(T) = \Delta E_T^0 - \alpha T$, and a spin degeneracy factor of the level, g_n , and combining Eqns. (2.6) and (2.8) leads to the relation:

$$e_n^t/T^2 = \epsilon_n \exp(-(\Delta E_T^0 + \Delta E_B)/kT) \quad (2.9)$$

where

$$\epsilon_n = 3.26 \times 10^{21} M_c g_n \sigma_\infty [(m_d/m_0)^{3/2} / (m_c/m_0)^{1/2}] \exp(\alpha/k) \quad (2.10)$$

In transient capacitance measurements the emission rates of electrons from a deep level are measured at different temperatures. From Eqn. (2.9), the plot of $\ln(T^2/e_n^t)$ versus $1/T$ gives the thermal activation energy with energy barrier $(\Delta E_T^0 + \Delta E_B)$ and the constant ϵ_n . Knowing ϵ_n , the capture cross section σ_∞ for $T \rightarrow \infty$ may be determined, provided α is

known. Equations for the thermal emission rate of holes from the hole traps are similar except that parameters related to electrons should be replaced by those for holes.

In the energy band diagram of a Schottky diode shown in Figure 2.2 it is assumed that the n-type semiconductor contains both shallow donors with concentration, N_D , and electron traps with concentration, N_T . In the steady state, the traps above the Fermi-level are all ionized and positively charged. The traps below the Fermi-level are full and neutral. By changing the bias applied to the junction, the width of the depletion region, W , will be changed. A small forward bias applied to the junction will reduce the band-bending and the empty traps in the region $0 \leq x \leq \lambda$ are filled by electrons. When the junction is switched back again to a reversed bias condition, the filled traps in the region $0 \leq x \leq \lambda$ are above the Fermi-level and the captured electrons thermally emit to the conduction band according to:

$$N_T^+ = N_T(1 - \exp(-e_n^t t)) \quad (2.11)$$

As a result, the space charge density in the depletion region increases and so does the junction capacitance. For a quantitative analysis of the capacitance transients, it should be assumed that the depletion region is well defined and no excess carriers are generated within it. With a quiescent reverse bias V_R applied to the diode, the space charge concentration in the depletion region is given by

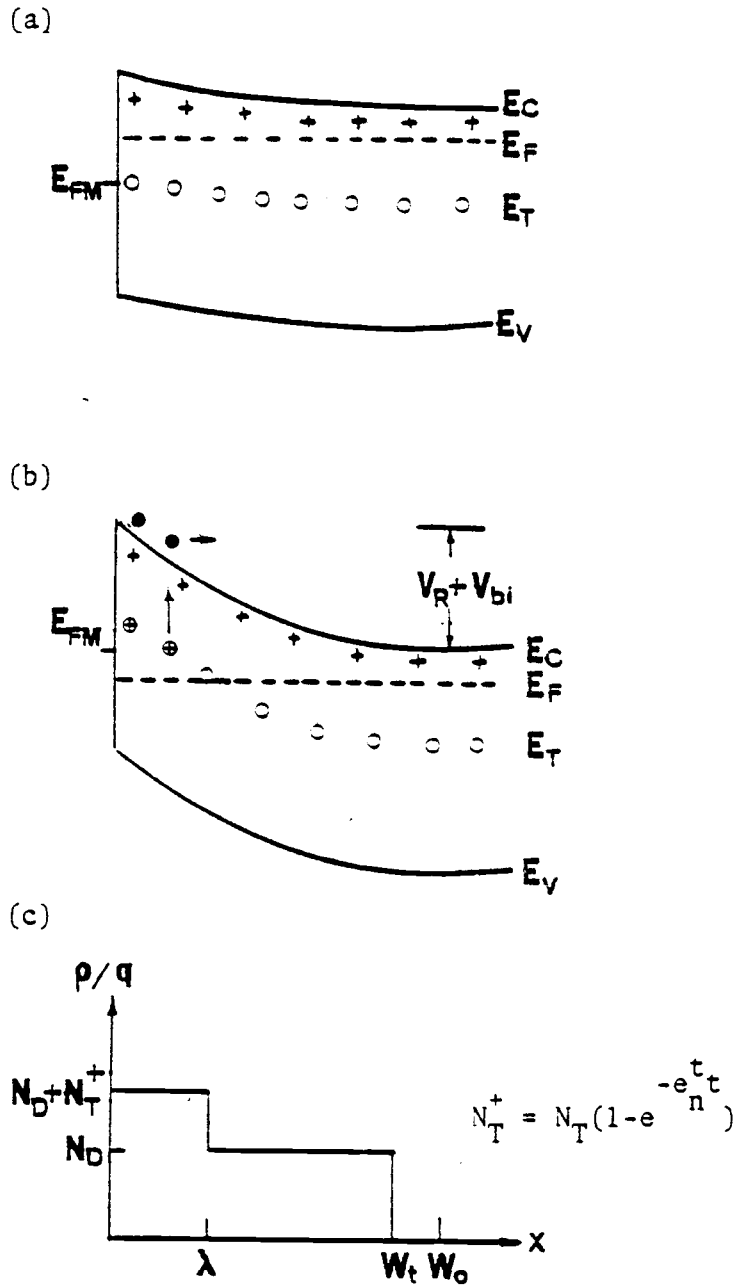


Figure 2.2. (a) Filling of electron traps in the depletion region of a Schottky barrier on an n-type semiconductor due to a forward bias pulse. (b) Thermal electron emission after bias switched back to quiescent reverse value. (c) Instantaneous charge density in the depletion region.

$$\begin{aligned}
\rho(x) &= N_D + N_T^+ & , 0 < x < \lambda \\
&= qN_D & , \lambda < x < w \\
&= 0 & , x > w
\end{aligned}
\tag{2.12}$$

From a double integration of Poisson's equation and application of the above boundary conditions, the depletion width, w , can be obtained. The time dependent capacitance due to electron trap emission for a small value of N_T/N_D and a large reverse bias is approximately given by⁽³⁷⁾

$$C(t) = C_\infty - (C_\infty - C_0)e^{-\frac{t}{\tau_n}} \tag{2.13}$$

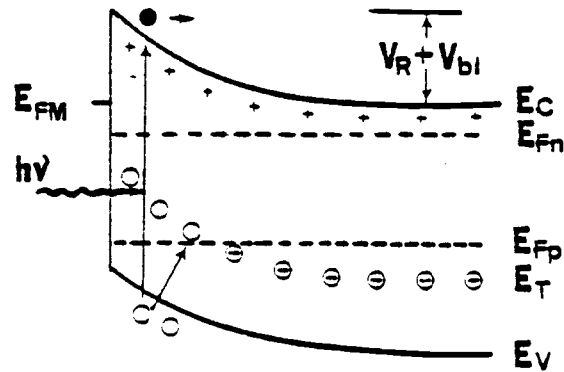
where C_0 and C_∞ are the diode capacitances when $t = 0^+$ and ∞ , respectively. The trap concentration can also be approximately estimated by

$$N_T \approx \frac{2\Delta C(0)}{C_\infty} N_D \tag{2.14}$$

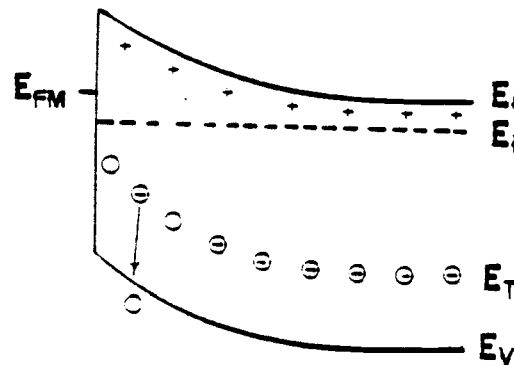
where $\Delta C(0) = C_\infty - C_0$ is the capacitance change when $t = 0^+$. The capacitance transients are nonexponential when the trap densities are comparable to N_D . For such cases a correction factor⁽³⁸⁾ or measurement of the long-term decay constants⁽³⁹⁾ is necessary for deriving more accurate emission rates.

The technique to initiate thermal emission from minority carrier traps differs from that for majority carrier traps. Minority carrier traps in the depletion region of Schottky diodes can only be filled by optical excitation. With reference to Figure 2.3, which shows the energy band diagram of a metal-n-type semiconductor junction under illumination by intrinsic light, the occupancy of hole traps in the

(a)



(b)



(c)

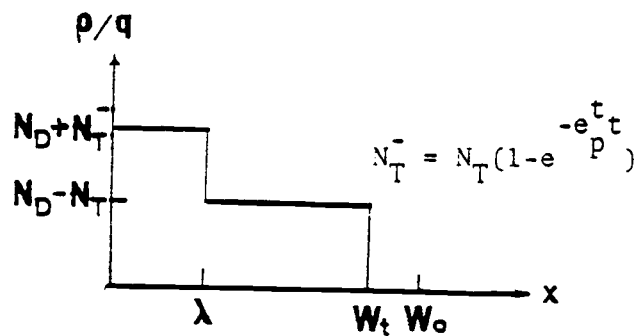


Figure 2.3. (a) Filling of hole traps in the depletion region of a Schottky barrier on an n-type semiconductor due to intrinsic photo-excitation.
 (b) Thermal emission of holes from hole traps in the dark.
 (c) Instantaneous charge density in the depletion region.

depletion region is determined by the hole quasi-Fermi level. Traps above the hole quasi-Fermi level are filled by the excess holes and become neutral, and the traps below it still remain negatively charged. At the instant when the illumination is removed, the hole quasi-Fermi level no longer exists and the filled hole traps emit holes thermally to the valence band. Thus, the photocapacitance gradually decays to a quiescent value. With the assumptions of $N_T \ll n$ and an abrupt depletion region, the transient capacitance, can be approximately estimated by⁽⁴⁰⁾

$$C(t) \approx C_0 (1 + (P_t(0) \exp(-e_p^t t)) / 2n) \quad (2.15)$$

where $P_t(0)$ is the hole population in the hole trap when $t = 0^+$, and C_0 is the steady state value of the junction capacitance.

The capacitance transients due to hole emission from hole traps are always found to be nonexponential, irrespective of the trap density. This is because the edge of the depletion region is not abrupt, the free carrier density $n(x)$ at distance x from the edge falls off according to the law

$$n(x) \approx n e^{-x^2 / 2L_D^2} \quad (2.16a)$$

with

$$L_D = (\epsilon_r \epsilon_0 kT / q^2 n)^{1/2} \quad (2.16b)$$

where L_D is the Debye length. This tail of free carriers, which can even penetrate the space charge region depending on the free carrier

density and the position of the hole quasi-Fermi level, would affect the trapping and detrapping from the centers. Consequently, the electric field profile would be affected, leading to nonexponential capacitance transients. In addition, greater deviations from the exponential behavior occur when the trap densities are comparable to the background carrier concentration. The time constants of emission for hole traps are calculated in the same way as for electron traps with large densities.

2.1.4 Theory of Electron Photoionization Cross Section Spectrum

For negligible thermal emission and capture rates, the optical emission from a trap level with total concentration N_T is given by

$$\frac{dn}{dt} = -e_n^0 n_T \quad (2.17)$$

where n_T is the concentration of occupied centers and e_n^0 is the optical emission rate for electrons. Thus the occupancy of the level is governed by the equation

$$n_T(t) = N_T \exp(-e_n^0 t) \quad (2.18)$$

The optical emission rates are related to the photoionization cross sections, σ_n^0 , by

$$e_n^0(h\nu) = \sigma_n^0(h\nu) \Phi(h\nu) \quad (2.19)$$

where Φ is the illumination intensity in photons $\cdot \text{cm}^{-2} \cdot \text{sec}^{-1}$.

The photoionization cross section can be theoretically estimated from the potential which binds the charged carrier to the atomic system. Lucovsky⁽⁴¹⁾ calculated the cross section taking into account transitions from a deep level to a parabolic band with the assumption of a delta-function potential for the impurity. The cross section so calculated can be expressed by:

$$\sigma_n^o(h\nu) \propto \frac{(E_n)^{1/2} (h\nu - E_n)^{3/2}}{(h\nu)^3} \quad (2.20)$$

where E_n is the optical ionization energy of the deep level, which is not necessarily equal to the thermal activation energy, ΔE_T , obtained from the transient capacitance measurements or the depth E_T obtained from Hall measurements. The normalized optical capture cross section as a function of normalized photon energy is shown in Figure 2.4. The peak occurs at $h\nu/E_n = 2$. This model has been used with considerable success for intermediate level centers. However, if the assumption is made that all carrier masses used in the calculations are not equal to the effective mass in the parabolic band into which the electron is optically excited, the cross section is given by⁽⁴²⁾

$$\sigma_n^o(h\nu) \propto \frac{(E_n)^{1/2} (h\nu - E_n)^{3/2}}{h\nu [h\nu + E_n (m_T/m_d - 1)]^2} \quad (2.21)$$

where m_T is the mass of the bound particle. It is seen that Eqn. (2.21) reduces to Eqn. (2.20) when $m_T = m_d$. There is no temperature dependence included in Lucovsky's model and hence it may not be applicable to deep levels which have strong coupling with the lattice. Huang and Rhys⁽⁴³⁾ have made similar calculations in which the temperature dependence has

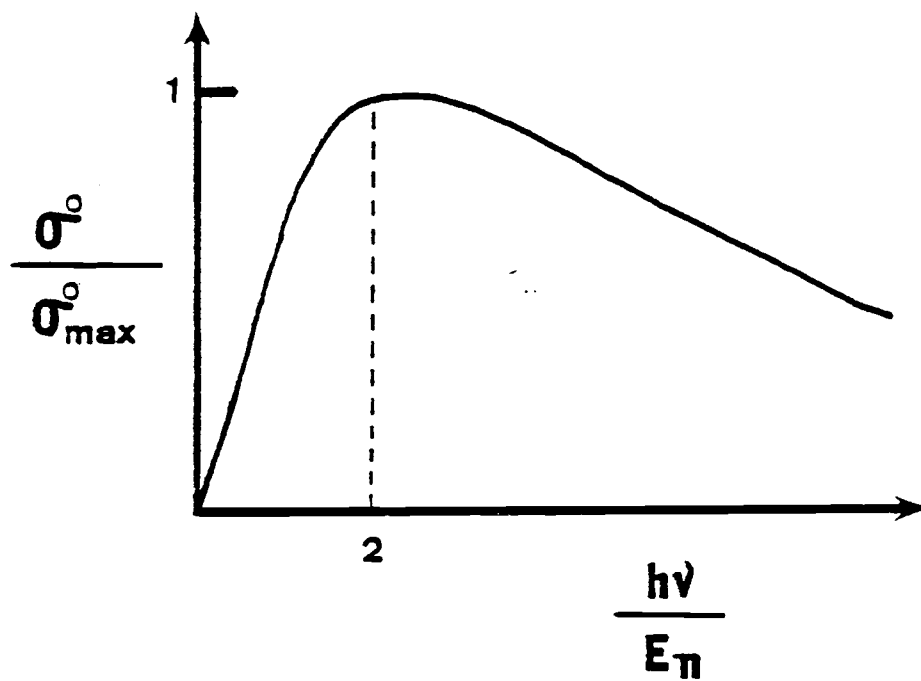


Figure 2.4. Normalized photoionization cross section versus normalized photon energy calculated from Lucovsky's model.

been included. Using their model, Jaros⁽⁴⁴⁾ expressed the photoionization cross section in the following form:

$$\sigma_n^o(h\nu) \sim \frac{1}{h\nu} \int_0^\infty dE \rho(E) \left| \frac{(1 \pm \eta) E^{1/2}}{|E_n| + E} + \frac{(1 \mp \eta) (E_F)^{1/2}}{|E_n| - E - (E_g + E_p)/2} \right|^2 \times U^{-1/2} \exp\left(-\frac{[h\nu - (|E_n| + E)]^2}{U}\right) \quad (2.22)$$

where $U = 2 d_{FC}(\hbar\omega)/\tanh(\hbar\omega/2kT)$

and $E_n = E_o + d_{FC}$.

Here d_{FC} is the Franck-Condon shift, E_o is the binding energy, $\rho(E)$ is the density of electron states, E_F is the free-electron Fermi energy, and E_p is the average optical gap, which is a measure of the strength of the crystal potential. $\eta(E)$ is a function which takes a value of unity near the band edges and tends to 0 when $(h\nu - |E_n|) \rightarrow \infty$. Usually the form $\eta(E) = \exp(-2E/E_p)$ is chosen. The basic assumptions in the derivation of Eqn. (2.22) are: a strong coupling between the defect and the lattice, linear electron-phonon interactions in the lattice coordinates, and negligible temperature dependence of $\rho(E)$ and E_o . Knowing the values of the different parameters, the photoionization cross section can be calculated by virtue of Eqn. (2.19).

2.2 Theory of Transport Measurements

Of the wide variety of charge transport phenomena, the galvanomagnetic effects have proved to be most valuable for semiconductor characterization. The galvanomagnetic effects relevant to this study are Hall effect and associated specific resistivity measurements. The Hall coefficient, R_H , is of prime importance because of the direct re-

relationship between R_H and the free carrier concentrations, n or p , in a semiconductor. The relation is given by⁽⁴⁵⁾

$$R_H = \frac{r}{q} \frac{p - b^2 n}{(p + bn)^2} \quad (2.23)$$

where b is the ratio of electron and hole mobility, μ_n/μ_p , and $r = \langle \tau^2 \rangle / \langle \tau \rangle^2$ is the scattering factor, which is of the order of unity. It is also the ratio of the Hall and drift mobilities. The parameter τ is the carrier relaxation time associated with scattering processes. If one type of carrier predominates in the material, Eqn. (2.23) may be simplified to

$$R_H = - \frac{r}{qn} \quad , \quad n \gg p \quad (2.24)$$

or

$$R_H = \frac{r}{qp} \quad , \quad p \gg n \quad (2.25)$$

The carrier concentration, as measured by the Hall coefficient, can be combined with the resistivity, ρ , to obtain the Hall carrier mobility, μ_H , which differs from the drift mobilities, μ_n or μ_p . The relation is given by

$$\mu_H = \frac{|R_H|}{\rho} \quad (2.26)$$

van der Pauw⁽²⁵⁾ has derived the theory for measuring the resistivity and the Hall coefficient of uniformly flat sample of arbitrary shape. The requirements are that the contact areas should be small compared to the sample dimensions and located at the circumference of the sample.

The resistivity can then be expressed as:

$$\rho = \frac{\pi d}{\ln 2} \frac{(R_{AB,CD} + R_{BC,AD})}{2} f\left(\frac{R_{AB,CD}}{R_{BC,DA}}\right), \quad (2.27)$$

where d is the thickness of the layer. With reference to Figure 2.5, $R_{AB,CD}$ is the average resistance obtained by passing in both directions a current through the dots A and B and measuring the voltage across C and D. $R_{BC,AD}$ is similarly defined. The value of the function f depends on the ratio of $R_{AB,CD}$ to $R_{BC,AD}$ and has been calculated by van der Pauw⁽²⁵⁾. The Hall coefficient is given by

$$R_H = \frac{d}{B} \Delta R_{AC,BD} \quad (2.28)$$

where $\Delta R_{AC,BD}$ is the change in resistance $R_{AC,BD}$ due to the application of the magnetic field with a flux density equal to B .

In order to obtain the free carrier concentration, n or p , the Hall scattering factor, r , must be known. The value of r tends to unity for large values of applied magnetic field. This provides an experimental method of measuring r . It should be cautioned that this condition will not necessarily be true if the bands are nonparabolic and have non-spherical constant energy surfaces, or if carriers in more than one band contribute to conduction⁽⁴⁶⁾.

The major difficulty encountered in Hall measurements is the fabrication of ohmic contacts at the edges of the sample. van der Pauw⁽²⁵⁾ has outlined correction factors for various imperfect contacts. The problem can also be minimized by using a clover-leaf pattern for the sample as shown in Figure 2.6, in which the contacts need not necessarily

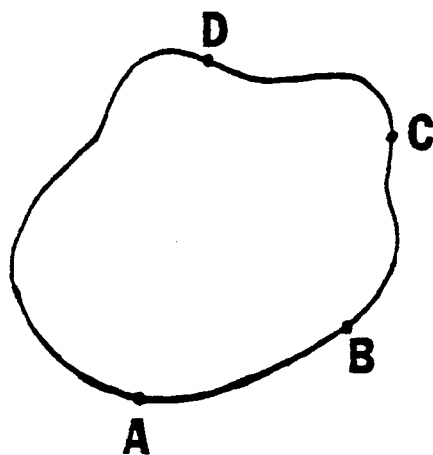


Figure 2.5. A van der Pauw sample of arbitrary shape with four small contacts along the circumference.

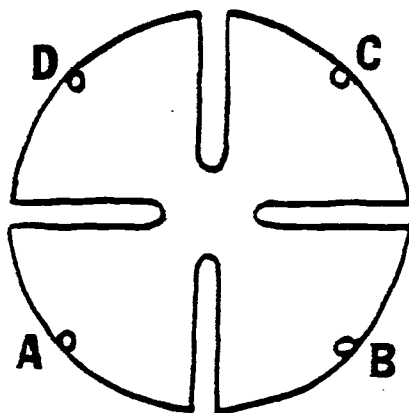


Figure 2.6. The "clover-leaf" pattern in which influence of the contact geometry can be reduced considerably.

be at the edges.

The important parameters obtained from the low-field transport measurements are carrier concentration and mobility of carriers. The temperature dependence of the Hall carrier concentration can be analyzed taking into account the charge neutrality condition. Donor and acceptor densities, ionization energies and the Fermi energy can be estimated and parameters related to the band structure determined. From analysis of the temperature dependence of mobility, the degree of compensation and the influence of different scattering mechanisms which limit the mobility are exposed.

CHAPTER III

EXPERIMENTAL TECHNIQUES

In this chapter, the compound semiconductor materials used, and the processes to fabricate Schottky diodes and van der Pauw samples on the epitaxial layers are first described. This is followed by descriptions of the techniques used to identify and characterize traps and a description of the low-field transport measurements. Limitations of some of these techniques are discussed at the end.

3.1 Material Description

The epitaxial layers of $\text{In}_{1-x}\text{Ga}_x\text{As}_y\text{P}_{1-y}$ were grown on both semi-insulating and heavily doped InP substrates. The layers were grown by conventional liquid and vapor phase epitaxial growth techniques at Varian Associates and RCA Laboratories, respectively. The band gap in these layers varied from 0.75 eV ($\text{In}_{0.53}\text{Ga}_{0.47}\text{As}$) to 1.35 eV (InP). The room-temperature carrier concentrations were in the range $(1.3 - 9.4) \times 10^{16} \text{ cm}^{-3}$ for the LPE layers and $(0.3 - 1.4) \times 10^{16} \text{ cm}^{-3}$ for the VPE layers. The epitaxial layers of $\text{Ga}_{1-x}\text{Al}_x\text{As}$ were grown without intentional doping by the LPE technique at the Standard Telecommunication Laboratories (UK) on Cr-doped semi-insulating GaAs or Si-doped conducting GaAs substrates. The room-temperature carrier concentrations were in the range $(5 - 15) \times 10^{15} \text{ cm}^{-3}$. The AlAs content, x , in these layers varied from 0.19 to 0.78 and was determined by converting measured room-temperature cathodoluminescence band gap energies into compositions with the aid of the data reported by Panish⁽⁴⁷⁾.

3.2 Fabrication of Schottky Diodes on Epitaxial Layers

3.2.1 Schottky Diodes on $\text{In}_{1-x}\text{Ga}_x\text{As}_{1-y}\text{P}_y$

Experimental samples having dimensions of $5 \times 5 \text{ mm}^2$ were degreased by boiling several times in Trichloroethylene (TCE), Acetone, Methanol, and Isopropyl alcohol (IPA). This was followed by an etch for 15 sec. in 0.2% Bromine-Methanol at 40°C . For epitaxial layers grown on heavily doped InP substrates, 1000 \AA of Sn and then 5000 \AA Ag were evaporated at pressures below 2×10^{-6} Torr to form two parallel strip contacts on the substrate. The contacts were alloyed in an ultra high purity N_2 atmosphere at a temperature of 450°C for 5 min. For epitaxial layers grown on semi-insulating substrates, the ohmic contacts were formed on the epitaxial layers. In the case of p-type layers, 200 \AA of Au, 300 \AA of Zn, and then 1000 \AA of Au were evaporated and alloyed at 400°C for 5 min. For n-type layers, 2000 \AA of an In (10%) - Sn (90%) alloy was evaporated and alloyed at 350°C for 5 min. The ohmic nature of the contacts was checked by using a TEKTRONIX 576 Curve Tracer. To remove any oxide on the epitaxial layers which may have formed during alloying and subsequent I-V measurements, the samples were etched for 10-15 sec. in 0.2% Bromine-Methanol at 40°C with a protective wax on the ohmic contacts. The samples were then rinsed with de-ionized water and IPA and blown dry with ultra high purity N_2 gas. Thin ($300\text{-}500 \text{ \AA}$) Au dots with areas of $(1 - 2) \times 10^{-3} \text{ cm}^2$ were then evaporated on the epitaxial layers.

In some cases, thin interfacial oxide films were formed⁽²⁶⁾ before depositing the Au Schottky barriers in order to enhance the barrier height. The forward threshold voltage of the diodes varied from

0.3 to 0.5 V and the reverse breakdown voltage varied from 3 to 10 V depending on carrier concentration. Only those diodes which exhibited minimal leakage current under reverse-biased conditions were used for measurements.

3.2.2 Schottky Diodes on $\text{Ga}_{1-x}\text{Al}_x\text{As}$

The procedure followed to fabricate Schottky diodes on these epitaxial layers was the same as that for $\text{In}_{1-x}\text{Ga}_x\text{As}_y\text{P}_{1-y}$. The pre-etching and etching after alloying of the ohmic contacts were done in a mixture of 1 H_2SO_4 :1 H_2O_2 :160 H_2O at room temperature. Ohmic contacts were formed by evaporating 1000 Å Sn and then 5000 Å Ag and the contacts were alloyed in an ultra high purity N_2 atmosphere at 450°C for 5 min.

3.3 Fabrication of van der Pauw Samples

Samples of $\text{In}_{1-x}\text{Ga}_x\text{As}_y\text{P}_{1-y}$ and $\text{Ga}_{1-x}\text{Al}_x\text{As}$ with dimensions $3 \times 3 \text{ mm}^2$ were degreased and etched by the procedures outlined in Sec. 3.2. Ohmic contacts were made symmetrically at the four corners of the samples by vacuum evaporation and their ohmic nature was ensured.

All measurements described here were done in the dark except when the sample was intentionally illuminated.

3.4 Transient Capacitance Measurements

3.4.1 Trap Emission Measurement

The sample was mounted on a jig which consists of two copper plates separated by an insulating post. A heating element was clamped to the lower surface of the lower plate. The sample rested on the lower plate which made electrical contact with the ohmic contact of the device.

The probe which made contact with the Au Schottky diode consists of a short Au wire fixed to the end of a coiled tungsten wire with high conductivity silver epoxy. The tungsten coil is fixed to the upper plate and 50 ohm BNC coaxial cables formed the electrical leads from the two plates.

The jig with the mounted sample was placed inside a thermally insulated double-walled glass tube as shown in Figure 3.1. A circular window facilitated illumination of the sample, when necessary. The temperature of the sample could be varied from 100 to 400°K by means of a stream of cooled N₂ gas and the heating element. The temperature was accurately measured with a chromel-alumel thermocouple with the measuring junction placed close to the sample.

The schematics of the measurement system is shown in Figure 3.2. The equipment used in this system is described below.

- (a) BOONTON Model 72B Capacitance Meter capable of measuring capacitances in the range of 0.01 PF to 3000 PF with a 1V or 3V full scale analog output. The meter uses a test signal of 1 MHz with a response time of ~ 1 msec.
- (b) KEITHLEY Model 602 Electrometer used to amplify the output signal from the capacitance meter. The maximum gain obtainable is 1000 and being battery operated, the instrument has extremely low noise characteristics.
- (c) H-P Model 7035B X-Y Recorder is used for recording the transients after suitable amplification by the electrometer. The time scale is provided by an EXACT Type 251 Function Generator.

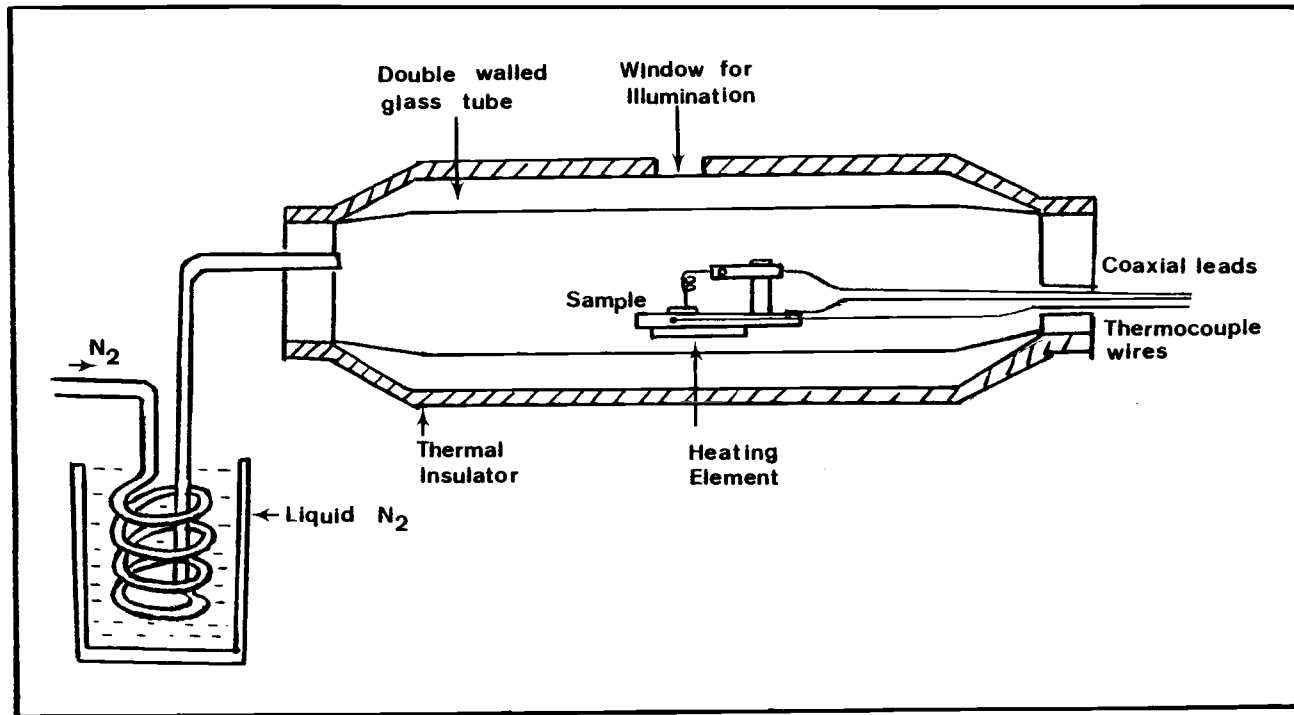
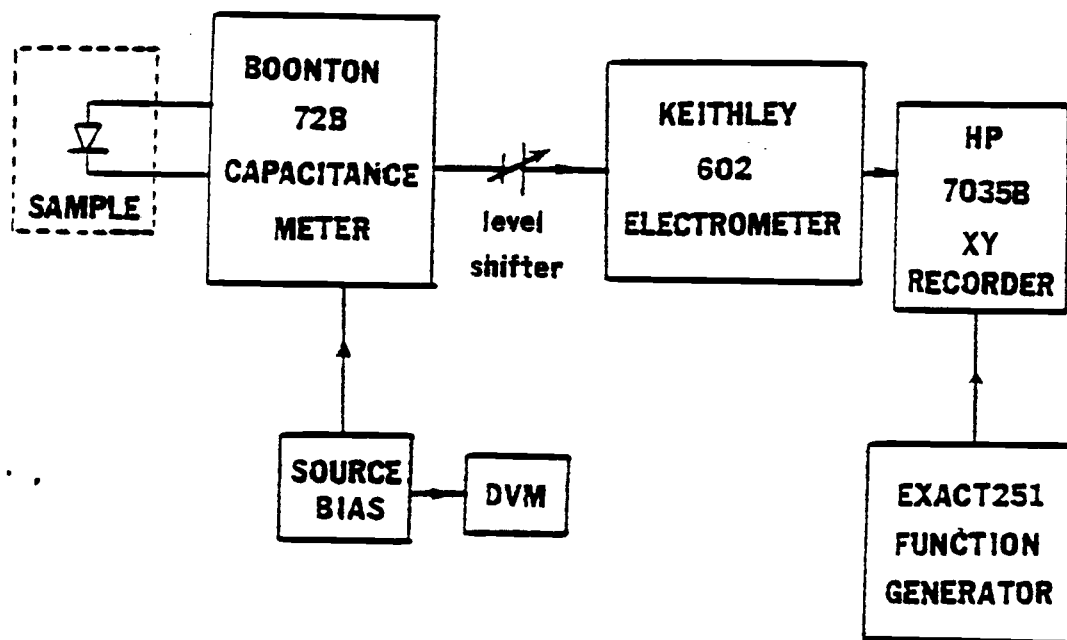


Figure 3.1. Mounting of sample inside insulating chamber for capacitance measurements.



Transient Capacitance Measurement

Figure 3.2. Schematic diagram for transient capacitance measurements.

Transients for electron traps at a particular temperature were initiated by switching the bias on the Schottky diode from a small forward value, to fill the traps in the depletion region to a large reverse value, when the electrons were thermally emitted to the conduction band with a characteristic time constant dependent on the temperature. Transients for hole traps at a particular temperature were initiated by illuminating the sample for a few seconds with intrinsic light, with zero or a small reverse bias applied to the diode. Since the magnitude of the incremental transient capacitance was of interest, the steady state capacitance of the depletion region and any other stray capacitances were offset by a voltage level shifter placed in series with the positive analog output terminal of the capacitance meter. The transient signal after suitable amplification was recorded by the X-Y recorder. The activation energy and the thermal capture cross-section of the trap can be obtained from the results of these measurements.

3.4.2 Trap Capture Measurements

The arrangement for the measurement of carrier capture rate by traps was the same as for emission measurements except that the trap-filling process was achieved by single injection pulses of varying durations. The capture rate was obtained from the incremental capacitance change at $t = 0$ after the application of the injection pulse.

The barrier energy associated with the trap, ΔE_B , can be obtained from the electron capture rates at different temperatures.

3.5 Thermally Stimulated Capacitance (TSCAP) Measurements

These measurements were performed to study the thermal and optical properties of defect centers present in LPE $\text{Ga}_{1-x}\text{Al}_x\text{As}$.

The sample was mounted on a circular copper plate 7 cm in diameter. A heating element was fixed in a cavity in the plate. Contacts to the Au and ohmic contact were made by two gold wire probes fixed to the ends of two copper strips which were supported on teflon blocks. Fifty ohm BNC coaxial cables were connected to these two terminals. The measuring junction of a chromel-alumel thermocouple was placed near the sample. An aluminum cover, with a circular window in the center to facilitate illumination, of the sample was placed on the copper plate. A brass rod 15 cm long was fixed to the lower surface of the copper plate and immersed in a bath of liquid N_2 when it was necessary to lower the temperature of the sample.

The experimental arrangement is shown in Figure 3.3. A JARRELL ASH monochromator with a tungsten light source was used to provide illumination with wavelengths varying in the range 0.6 to 2.1 μm . Appropriate filtering and focusing optics was provided between the exit slit of the monochromator and the sample.

The BOONTON capacitance meter and H-P X-Y recorder were used, respectively, to monitor and record the diode capacitance. A KEITHLEY Type 174 digital multimeter was used to monitor the temperature of the sample and the analog output of this meter provided the signal for the X-axis of the X-Y recorder.

A typical cycle of measurement is as follows. With zero bias applied to the diode, the temperature of the sample was lowered from 300 to 80°K and the capacitance values were recorded by the X-Y

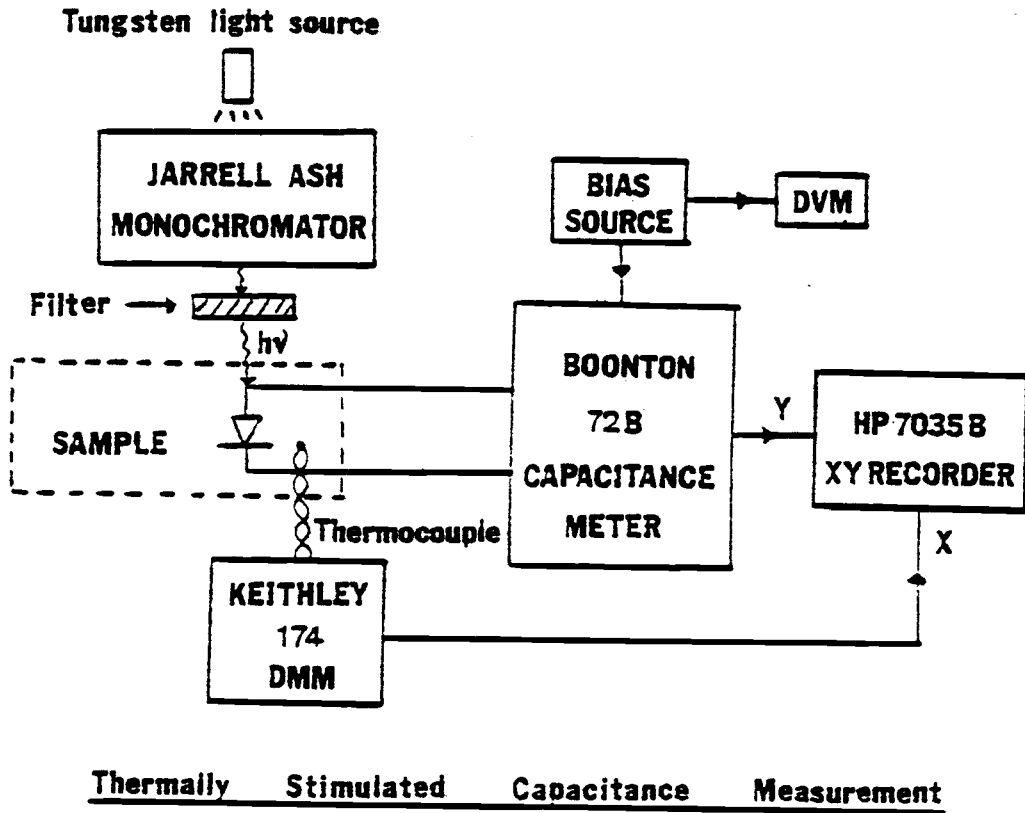


Figure 3.3. Schematic diagram for thermally stimulated capacitance measurements.

recorder. This constitutes step 1 and this step was found to be reversible, i.e., the capacitance profile was retraced when the sample temperature was increased again. Next a forward bias of ~ 1.0 V was applied to the diode and the temperature was lowered again. At the low-temperature limit of this step, the bias was switched back to zero and the temperature gradually raised at a rate of $6^\circ\text{C}/\text{min}$. The capacitance values were recorded by the X-Y recorder. This constitutes step 2. Finally, at the low temperature end of step 1, the sample was irradiated with 1.1 eV light, when an increase in capacitance was usually observed. At this point, step 3 was recorded by raising the temperature at the same rate of $6^\circ\text{C}/\text{min}$. to 300°K .

From the capacitance-temperature profiles, a qualitative understanding of the emptying and filling processes operative at defect centers in $\text{Ga}_{1-x}\text{Al}_x\text{As}$ could be obtained.

3.6 Optical Lineshape Measurements

The photoionization cross section $\sigma_n^\circ(h\nu)$, which is an important optical parameter of a defect center, can be obtained by this measurement. Most of the equipment used for these measurements were the same as those used for the TSCAP measurements described in Sec. 3.6 except that the X-axis of the recorder was driven by the EXACT type 251 Function Generator, instead of the KEITHLEY type 174 Digital Multimeter.

The procedure to determine $\sigma_n^\circ(h\nu)$ is as follows. The temperature of the sample was lowered to 80°K with zero bias applied to the Schottky diode so that all thermal emission and capture processes at the deep centers were inoperative. The diode was then irradiated with

monochromatic light of intensity ϕ and energy $h\nu$ in the range $0.7 \leq h\nu \leq 1.5$ eV. The defect centers were consequently depopulated and the capacitance of the diode increased due to optical emission with a characteristic time constant dependent on $h\nu$ and ϕ . The intensity of the radiation at the sample was estimated by using a PbS detector and a lock-in amplifier. Before repeating the experiment with a new radiation energy, the centers had to be refilled with electrons by thermal quenching to overcome any possible barrier which might be associated with electron capture.

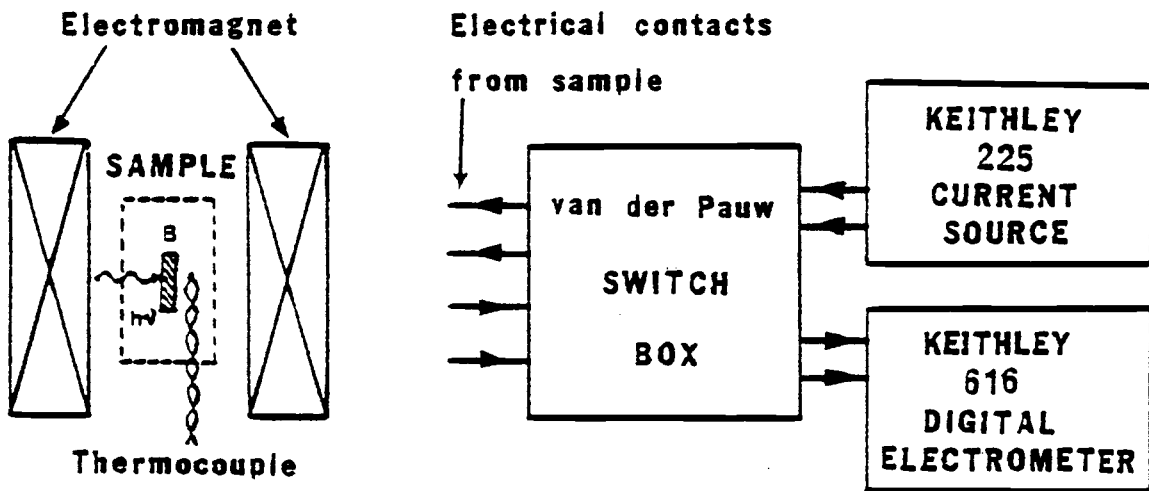
3.7 Hall and Photo-Hall Effect Measurements

These measurements were performed to obtain the Hall carrier concentration, n_H , and Hall mobility, μ_H . The data were subsequently analyzed to evaluate the transport properties in the different materials.

For measurements in the range 100-600°K, the van der Pauw sample was mounted on a gold-plated copper jig and held in place by four phosphor bronze probes on the ohmic contacts. The probes also served as electrical contacts. A heating element was housed in a cavity in the copper block and the measuring junction of a chromel-alumel thermocouple was located near the sample. The systems used to cool and illuminate the sample was the same as that used for the transient measurements. The sample was positioned symmetrically between the pole pieces of an electromagnet during the measurements.

The schematic diagram of the Hall and photo-Hall measurements is shown in Figure 3.4. The description of the equipment used is as follows:

- (a) A water-cooled electromagnet (made by Spectromagnetic Industries) which has the capability of producing a wide



Hall and Photo-Hall measurement

Figure 3.4. Schematic diagram for Hall and photo-Hall measurements.

range of magnetic flux densities by varying the gap between the pole pieces and the excitation current.

- (b) KEITHLEY Type 225 Current Source which can supply constant current in the range 10 pA - 10 mA in the reversible directions.
- (c) KEITHLEY Type 616 Digital Electrometer with very high input impedance can measure voltages down to 0.01 mV.
- (d) JARRELL ASH Monochromator and Light Source which have been described in an earlier section (Sec. 3.5).

The value of constant current used in these measurements was chosen to give the highest Hall-voltage reading without causing resistive heating in the sample, and was typically $\sim 100 \mu\text{A}$. The magnetic flux density was kept fixed at 0.5 Tesla for all the experiments in the course of this study. Measurements were performed at several fixed temperatures in the range of interest. At each measurement point the temperature was allowed to stabilize for 5 min. before the readings were taken. A flux of N_2 gas was made to flow over the sample during the high-temperature measurements. The measurements were extended to the temperature range 20-100°K by using the AIR PRODUCTS HELITRAN liquid He cryostat system.

3.8 Measurement of Photoconductivity Spectra

The spectral response of the photoconductivity was measured in an attempt to determine the location of the defect centers in the forbidden energy gap of $\text{In}_{1-x}\text{Ga}_x\text{As}_y\text{P}_{1-y}$. The measurements were performed at different constant temperatures. The apparatus used was essentially the same as for the Hall measurements. The photoconductivity in the

samples were induced by irradiation with monochromatic light with energy in the range $0.7 \leq h\nu \leq 1.1$ eV and the corresponding analog signals were recorded by an X-Y recorder.

3.9 Discussion

Amongst the many existing techniques, the transient capacitance measurements are perhaps the best for an accurate analysis and understanding of the trap properties. However, during the recording of capacitance transients, near-perfect isothermal conditions have to be maintained. Any temperature drift may result in wrong emission time constants and erroneous trap parameters from subsequent analyses of the data. Since the thermal capture cross section of the traps strongly depends on the electric field within the depletion region, consistency in the reverse bias voltage has to be maintained during measurements on different samples. The high field within the depletion region ensures that the rate of the recapture will be small. The shortest emission time constant which could be measured by the system described in Sec. 3.3.1 was limited by the response time of the X-Y recorder, which is about 1 sec. To record transients with smaller emission time constants, a transient recorder or a sampling oscilloscope is needed. The sensitivity of the measurements was determined by the noise added to the signal by the capacitance meter and the X-Y recorder. The KEITHLEY electrometer added very little noise to the signal. Traps with densities obeying $N_T/N_D = 10^{-3}$ could be detected with good accuracy.

Deep Level Transient Spectroscopy (DLTS)⁽⁴⁸⁾ offers the possibility of a rapid scan over a wide range of both majority and minority carrier traps with high sensitivity. However, for relatively large

trap densities which give rise to nonexponential transients, the DLTS technique would give rise to erroneous results⁽⁴⁹⁾. In the transient capacitance technique this difficulty can be overcome by a careful analysis of the transients. The TSCAP measurement technique provides an easy means for scanning majority carrier traps and, with different bias voltages applied to the diode, the trap concentration can be roughly estimated. A modified TSCAP method reported by Sah and Walker⁽⁵⁰⁾ known as "edge region TSCAP" can detect relatively shallow levels ($E_T < 200$ meV). Two drawbacks of the TSCAP method are poor resolution and low sensitivity. It is also difficult to maintain a constant scan rate for the temperature.

Measurement of the photoionization cross section and subsequent analysis of the optical lineshape provide important information related to the optical properties of defect centers, including their physico-chemical origin. However, stringent conditions have to be maintained during the measurements. The intensity of the photoexcitation has to be high enough so that the photocapacitance transients saturate before temperature drifts occur.

Hall-effect and resistivity measurements as functions of temperature are useful techniques for determining the different scattering processes responsible for limiting carrier mobilities in semiconductors. However, the following conditions need to be fulfilled⁽²⁵⁾:

- (a) The contacts have to be small, exhibit ohmic characteristics, and located on the circumference of the sample.
- (b) The sample thickness needs to be uniform.
- (c) The surface of the sample has to be singly connected, i.e., the sample does not have isolated holes.

Since a complete recording of the data at a particular temperature takes several minutes, considerable care has to be taken to maintain isothermal conditions. The speed of the measurements is constrained by the slow response of the electromagnet. High temperature measurements (over 600°K), which were not done in the course of this study, require special precautions against evaporation of As or p^(51,52). An electrometer with a high input impedance is required, especially for measurements at low temperature, in the quaternary material in which the resistivity was found to increase with the lowering of temperature below $T \sim 100^{\circ}\text{K}$.

CHAPTER IV

TRAPS IN $\text{In}_{1-x}\text{Ga}_x\text{As}_y\text{P}_{1-y}$

The results obtained from trap emission and capture studies on $\text{In}_{1-x}\text{Ga}_x\text{As}_y\text{P}_{1-y}$ are presented in this chapter. The experimental parameters determined by transient capacitance measurements are presented in Sec. 4.1. Carrier capture measurements and the results obtained therefrom, for a deep trap in the quaternary layers and a similar center in GaAs are presented in Sec. 4.2. Photoconductivity spectra for the quaternary layers are presented in Sec. 4.3. The results are discussed in Sec. 4.4.

4.1 Traps Identified From the Transient Capacitance Measurements4.1.1 Electron Traps

These measurements were performed to determine the activation energy and the capture cross section of traps. The X-Y plotter was used to record emission time constants which were ≥ 1.0 sec. Hence the temperatures of measurement had to be set in the appropriate range. Transients related to electron emission from electron traps were obtained in VPE and LPE quaternary layers at different temperature in the dark after injection of majority carriers by a forward bias pulse. The Schottky diode is usually biased in the reverse direction in the quiescent state. A typical transient for n-type VPE $\text{In}_{0.90}\text{Ga}_{0.10}\text{As}_{0.21}\text{P}_{0.79}$, recorded at 211°K for a quiescent reverse bias of -2.5V, is shown in Figure 4.1(a). The plots of $\ln \Delta C$ (where $\Delta C = C_\infty - C(t)$) versus time for this deep level at different temperatures, as shown in Figure 4.1(b), from which it is seen that the transients are nonexponential.

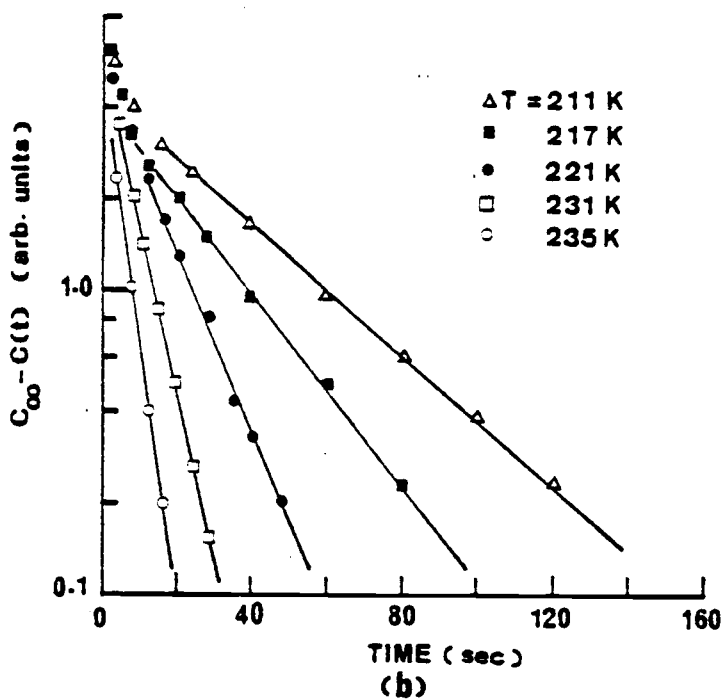
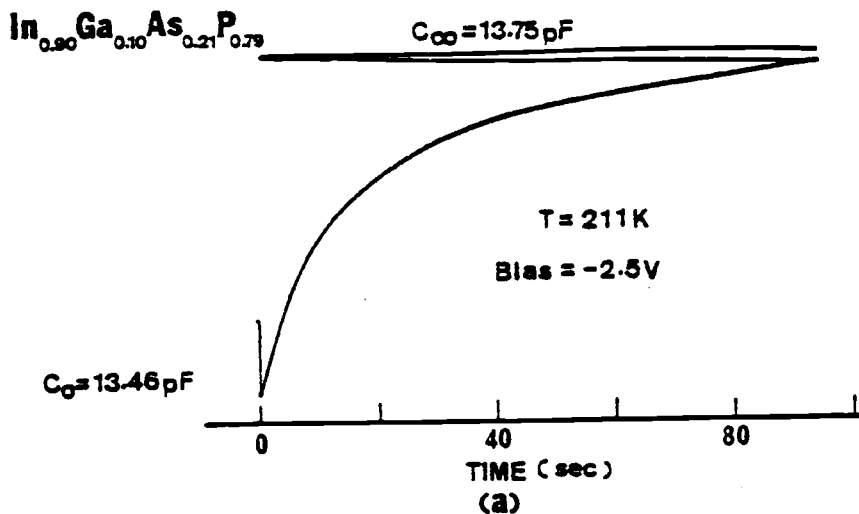


Figure 4.1. Transient capacitance measurement for electron traps in $\text{In}_{0.90}\text{Ga}_{0.10}\text{As}_{0.21}\text{P}_{0.79}$ crystal (a) capacitance transient obtained at 211°K ; and (b) plots of $\ln [C_{\infty} - C(t)]$ versus time at different temperatures.

The activation energy of the traps, and their thermal capture cross section for electron, were determined from the Arrhenius plots, as shown in Figure 4.2, by virtue of Eqn. (2.9). Linear regression analysis was used to derive the best fits of the experimental data. The value of α , which is the temperature coefficient of the trap activation energy ΔE_T in Eqn. (2.10), was assumed to be zero as a first approximation, and $g_n = 1/2$ was assumed for electron traps⁽⁵³⁾. The values of the effective mass m_n^*/m_0 were determined from the relation⁽¹⁸⁾

$$m_n^*/m_0 = 0.080 - 0.082y + 0.036y^2 \quad (4.1a)$$

with

$$x = 0.45y/(1 - 0.03y) \quad (4.1b)$$

The electron traps detected in the quaternary layers with different alloy compositions are depicted in Figure 4.2 and their characteristics were summarized in Table 4.1. It should be noted that the activation energies quoted in Table 4.1 and Figure 4.2 include the energy ΔE_B which reflects the temperature dependence of the thermal capture cross section. A value of $\Delta E_B = 0.04 - 0.08$ eV was determined for electron traps in $\text{In}_{1-x}\text{Ga}_x\text{As}$ alloys⁽⁵⁴⁾ and $\Delta E_B = 0.09$ eV was determined for electron traps in InP ⁽⁵⁵⁾. The values of ΔE_B could be of the same order for traps identified in the present investigation. The trap densities N_T were determined from the capacitance transients using the relation in Eqn. (2.14). Measurements were difficult to perform with samples having small band gaps as the corresponding low

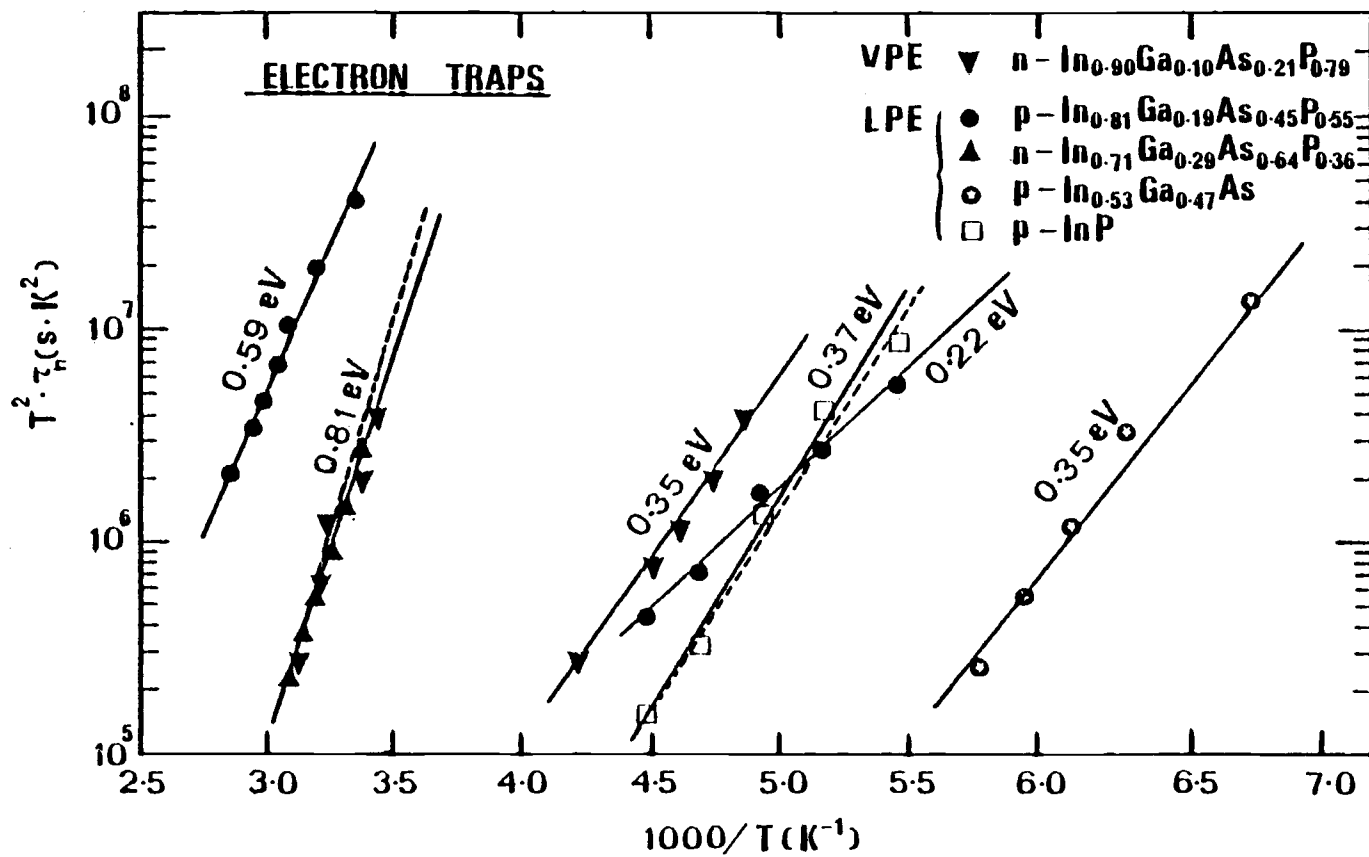


Figure 4.2. Temperature dependence of emission time constant for electron traps in LPE and VPE $\text{In}_{1-x}\text{Ga}_x\text{As}_y\text{P}_{1-y}$. The dashed lines indicate dominant traps in GaAs (see text).

TABLE 4.1. Parameters for trap levels identified in LPE and VPE $\text{In}_{1-x}\text{Ga}_x\text{As}_y\text{P}_{1-y}$

Material	E_g at 300°K (eV)	Electron Traps			Hole Traps							
		$(\Delta E_T + \Delta E_B)$ (eV)	N_T (cm^{-3})	σ_∞ (cm^2)	$(\Delta E_T + \Delta E_B)$ (eV)	N_T (cm^{-3})	σ_∞ (cm^2)					
VPE n- $\text{In}_{0.90}\text{Ga}_{0.10}\text{As}_{0.21}\text{P}_{0.79}$	1.19	0.81	5.9×10^{15}	5.9×10^{-14}	0.25	1.8×10^{14}	5.0×10^{-21}					
		0.35	3.1×10^{14}	9.0×10^{-19}								
p- $\text{In}_{0.81}\text{Ga}_{0.29}\text{As}_{0.45}\text{P}_{0.55}$	1.00	0.59	1.2×10^{15}	1.5×10^{-18}	-	-	-					
		0.22	5.0×10^{13}	4.3×10^{-21}								
LPE	n- $\text{In}_{0.71}\text{Ga}_{0.29}\text{As}_{0.64}\text{P}_{0.36}$	0.83	1.0×10^{13}	2.3×10^{-14}	0.27	3.0×10^{13}	2.5×10^{-21}					
		(0.81 eV trap may be present)						-	-	-		
		N- $\text{In}_{0.73}\text{Ga}_{0.27}\text{As}_{0.58}\text{P}_{0.42}$	0.98					-	-	-		
				0.75				6.8×10^{13}	9.4×10^{-16}	-	-	-
p- $\text{In}_{0.53}\text{Ga}_{0.47}\text{As}$	0.75	0.35	6.8×10^{13}	9.4×10^{-16}	-	-	-					
p-InP	1.35	0.37	3.0×10^{15}	1.1×10^{-17}	-	-	-					

barrier heights of the diodes gave rise to large reverse leakage currents.

4.1.2 Hole Traps

Transients for hole emission were observed in two VPE samples: n-type $\text{In}_{0.90}\text{Ga}_{0.10}\text{As}_{0.21}\text{P}_{0.79}$, and n-type $\text{In}_{0.71}\text{Ga}_{0.29}\text{As}_{0.64}\text{P}_{0.36}$. The transients at different temperatures were initiated by illuminating the sample with intrinsic light for a few seconds under a small reverse bias, and then recorded in the dark. The capacitance transient for n- $\text{In}_{0.90}\text{Ga}_{0.10}\text{As}_{0.21}\text{P}_{0.79}$ recorded at 184°K, for a quiescent reverse bias of -0.02 V is shown in Figure 4.3(a). The plots of $\ln \Delta C$ versus time for this hole trap at different temperatures are shown in Figure 4.3(b). The activation energy and the thermal capture cross section of the hole traps detected in these two samples were determined from the $T^2 \cdot \tau_p$ versus $1/T$ plots, as shown in Figure 4.4 by using linear regression analysis with reference to Eqn. (2.9). In this equation, the value of $m_p^*/m_0 = 0.72$ for $\text{InP}^{(56)}$ was used, α was assumed to be equal to zero and g_p equal to 2⁽⁵³⁾. The hole trap densities were estimated from Eqn. (2.10) as used in calculating electron trap densities. The characteristics of the hole traps are also listed in Table 4.1.

4.2 Capture Measurement for the 0.83 eV Electron Trap

It is observed that an electron trap with an activation energy of 0.82 ± 0.01 eV and a capture cross section $\sigma_{\infty} \sim 10^{-14} \text{ cm}^2$ is present in some of the quaternary samples. The density of the identified centers is small compared to the carrier concentration and this may be the reason for not observing emission from the center in the other samples. A dominant electron trap with identical activation energy and

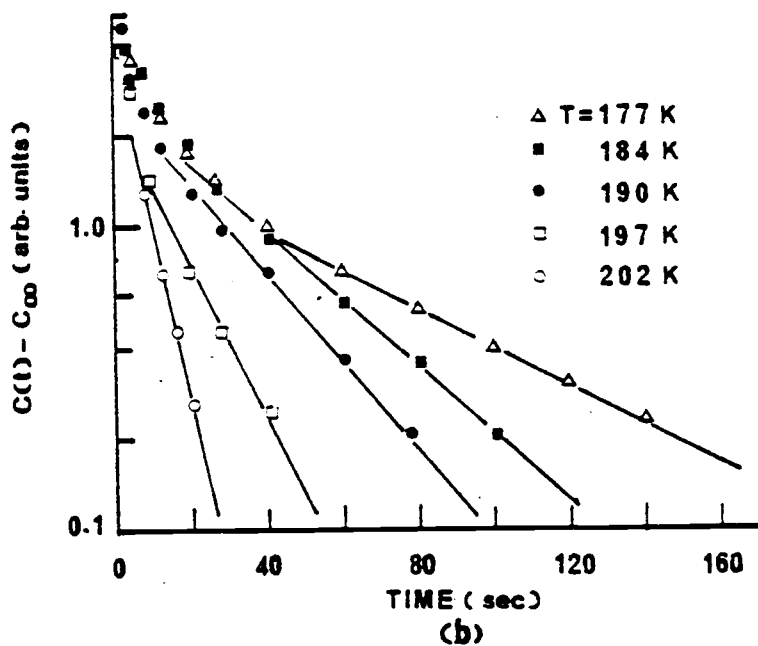
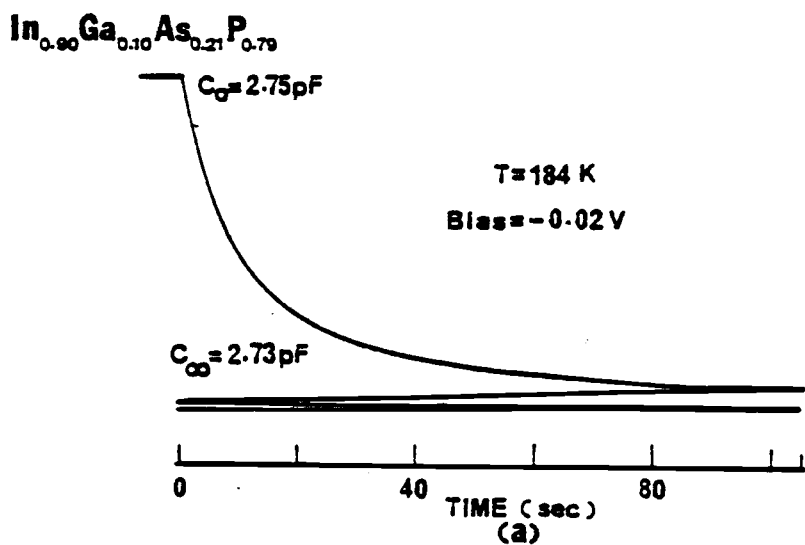


Figure 4.3. Transient capacitance measurements for hole traps in $\text{In}_{0.90}\text{Ga}_{0.10}\text{As}_{0.21}\text{P}_{0.79}$ crystal (a) capacitance transient at 184°K ; and (b) plots of $\ln[C(t) - C(\infty)]$ versus time at different temperatures.

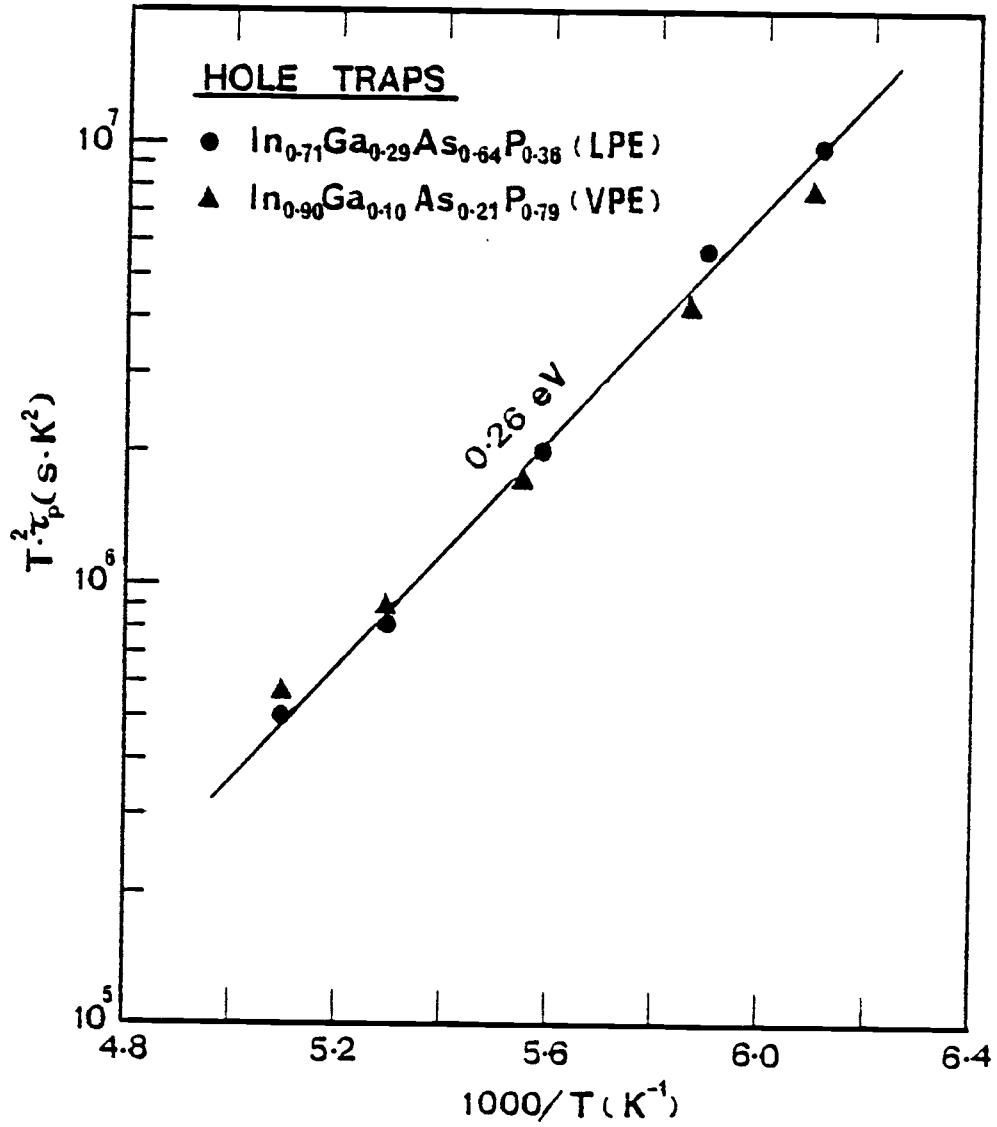


Figure 4.4. Temperature dependence of emission time constant for hole traps in LPE and VPE $\text{In}_{1-x}\text{Ga}_x\text{As}_y\text{P}_{1-y}$.

capture cross section, as depicted in Figure 4.2, is always observed in bulk and VPE GaAs⁽²⁷⁾. In order to make further comparisons between the centers in the binary and the quaternary materials, the capture rates at different temperatures were determined for the centers in a sample of organometallic VPE GaAs with a low trap density⁽²⁸⁾ and another of LPE $\text{In}_{1-x}\text{Ga}_x\text{As}_y\text{P}_{1-y}$ ($E_g = 0.95$ eV). The experiment is similar to the emission experiment, but the duration of the filling pulse t_f is varied from a very small value, when the traps are only partially filled, to a saturation value, which results in complete filling. The value of ΔC at $t = 0$ also changes accordingly. For small trap densities, which is true in the present case, the capture rate is given by Eqn. (2.7). Figure 4.5 shows the results obtained from the capture measurements. The capture rates for the trap in GaAs and that in the quaternary layer in the same temperature range, are almost identical. The capture cross section is related to the capture rate by Eqn. (2.5). Since the electron concentration in the conduction band is almost constant in the temperature range of interest, and the electron thermal velocity does not change appreciably, the slope of the plot of $\ln C$ versus $1/T$ is identical to that for the plot of $\ln \sigma$ versus $1/T$. It is of interest to observe that the energy of 0.085 eV, derived from the latter plot, for the electron trap in $\text{In}_{1-x}\text{Ga}_x\text{As}_y\text{P}_{1-y}$, is almost identical to that obtained for the 0.83 eV trap in GaAs, both in this study and by other workers⁽⁵⁷⁾. The energy corresponding to the slope has been interpreted as a barrier energy associated with the defect center⁽⁵⁷⁾.

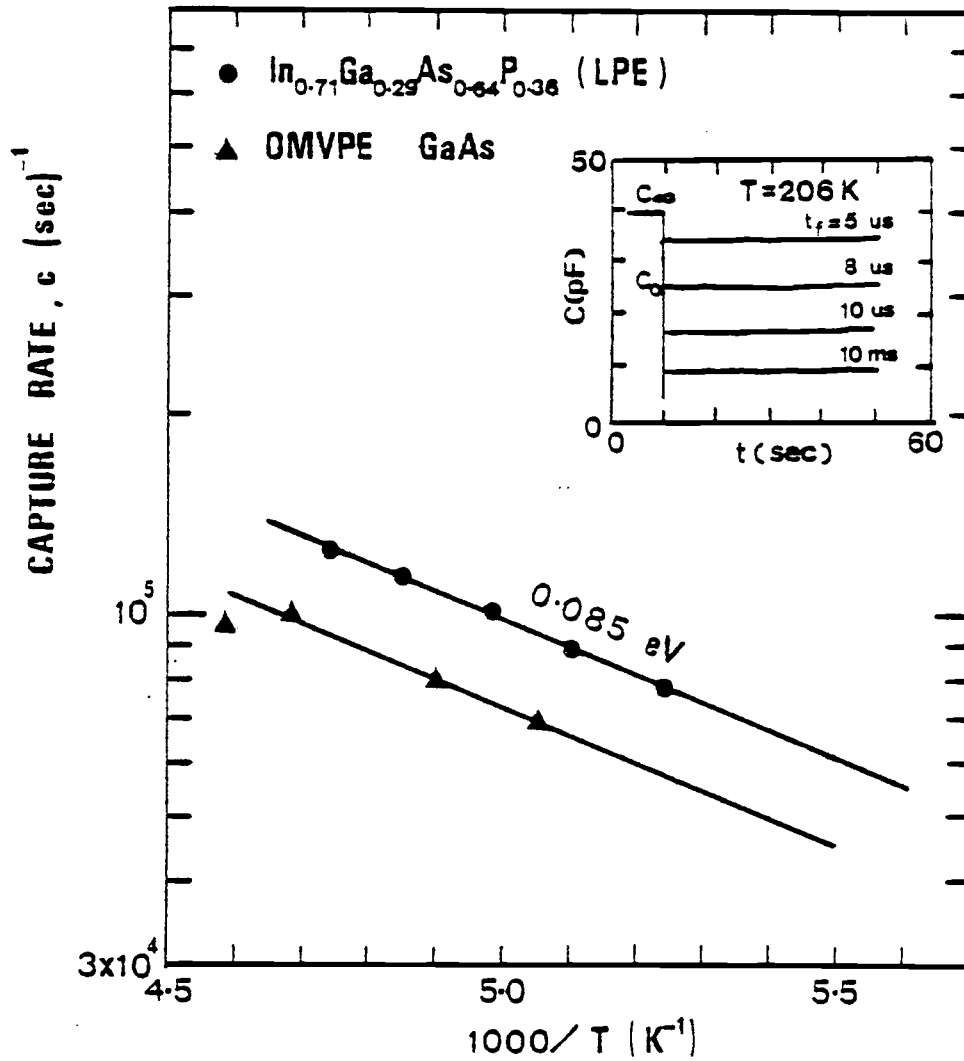


Figure 4.5. Temperature dependence of electron capture rates for 0.83 eV electron trap in GaAs and the 0.82 ± 0.01 eV electron trap in $\text{In}_{1-x}\text{Ga}_x\text{As}_y\text{P}_{1-y}$.

4.3 Electron Traps Identified From Photoconductivity Spectrum

Due to the inability to fabricate Schottky diodes with low reverse-leakage current on some quaternary samples, the defect levels in these layers were investigated by measuring the spectral response of photoconductivity. From the low-energy threshold of the photoconductivity spectrum, and a knowledge of the sign of the excited carriers from photo-Hall measurements, which will be described in Chapter V, it is possible to determine the location of the trap level. However, no such transition could be detected in the photoconductivity spectra of the VPE layers. This is perhaps due to the low concentration of the particular defects under consideration. Thresholds in the photoconductivity spectra are observed for the LPE layers. A typical spectral response of photoconductivity for an LPE quaternary layer with $E_g = 0.93$ eV is shown in Figure 4.6. Appropriate combinations of filters were used with the monochromator to eliminate higher orders of the incident light energy. A threshold at 0.89 eV is seen consistently at 141, 200 and 220°K. In addition, a threshold at 0.825 eV is observed at 141°K only. The threshold due to band edge absorption is seen to move to higher energies with lowering of temperature. An energy level model which explains the observed data is shown in the inset of Figure 4.6. An acceptor-like center which increases the low-temperature mobility upon photoexcitation, and is responsible for the observed persistent photoconductivity, is situated ~ 0.89 eV below the conduction band. In addition, the crystals have another center with a very low concentration for which a threshold is observed in the photoconductivity spectrum only at 141°K but not at the higher temperatures. The latter observation can only be explained by a donor-like deep level

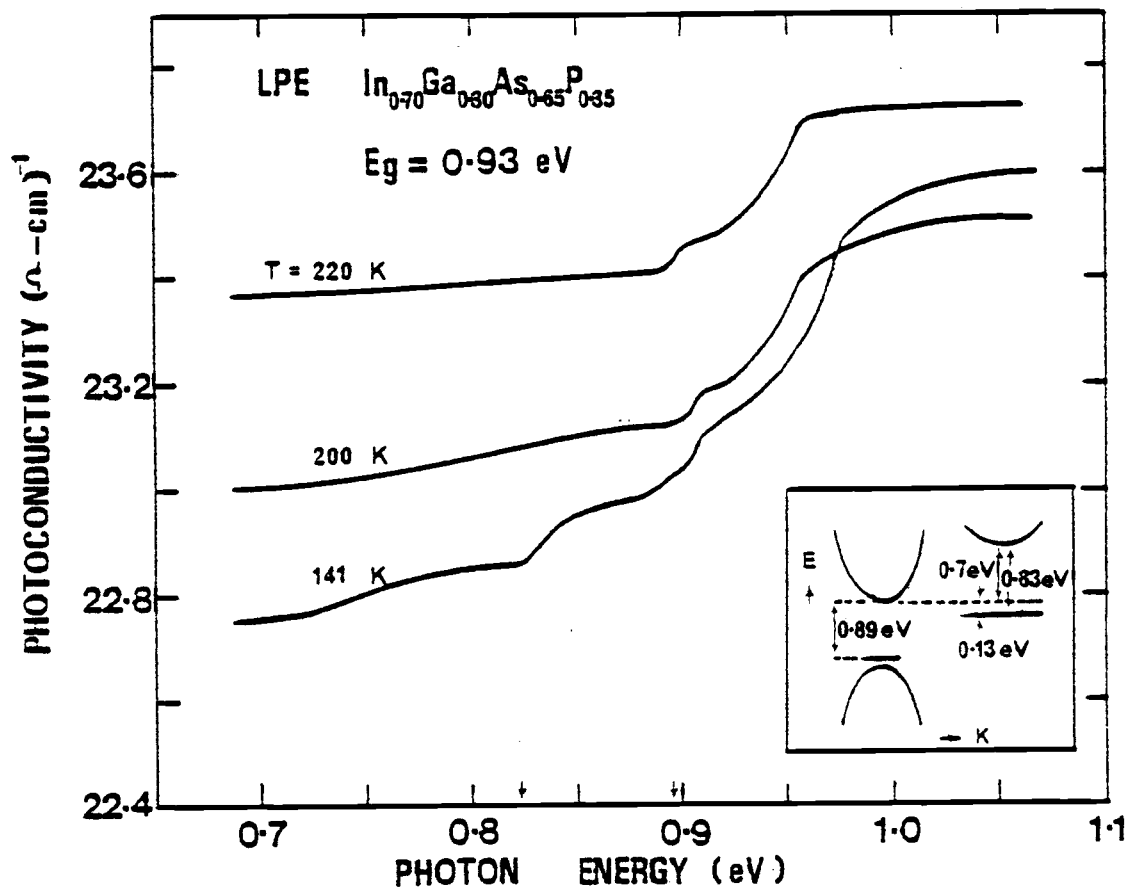


Figure 4.6. Spectral variation of photoconductivity at different temperatures. Inset shows the energy position of donor and acceptor levels in relation to the band edges.

below the Fermi-energy which emits electrons upon photoexcitation to an indirect conduction minimum. Such minima in the quaternary material are located ~ 0.7 eV above the Γ minimum⁽¹⁵⁾. This would place the donor level ~ 0.1 eV below the Γ valley edge and well below the Fermi level at 141°K. As the temperature is raised, the level is gradually ionized due to the lowering of the Fermi level in the gap and hence there are no electrons to be emitted upon photoexcitation.

4.4 Discussion

Most of the traps identified are not present consistently and have small concentrations. A result of some significance is the presence of the 0.82 ± 0.01 eV electron trap in at least three samples with different alloy compositions, grown by both LPE and VPE techniques. It is also quite possible that the donor-like deep level, with a threshold energy 0.83 eV, observed in the photoconductivity spectrum in the same center as the one found by the transient capacitance measurements. This, in effect, provides additional evidence to the fact the deep trap in $\text{In}_{1-x}\text{Ga}_x\text{As}_y\text{P}_{1-y}$, and in VPE and bulk GaAs, which were being compared in Sec. 4.2, are identical or related centers. Furthermore, since states near the valence band edge have a greater probability of being dominated by valence band wave functions, it is somewhat inconceivable for an electron trap to be located close to the valence band and interact with the central conduction minimum during the emission and capture processes. It is more likely that the center is linked to a higher indirect conduction minimum. Since the center is very deep, it would be delocalized in \vec{k} -space and the carrier transitions during emission and capture would be possible. It has been

established that the deep trap in GaAs is donor-like⁽⁵⁸⁾ and photo-ionization cross section⁽⁵⁹⁾ and capacitance⁽²⁷⁾ measurements indicate that the trap emits electron to indirect minima of conduction band. Other deep levels linked to higher conduction minima have been reported in InP⁽⁵⁵⁾, $\text{Al}_x\text{Ga}_{1-x}\text{As}$ ⁽⁶⁰⁾, and several other ternary alloys⁽⁶¹⁾. In order to study the origin of the 0.83 eV electron trap, organo-metallic VPE GaAs, in which the center is also dominant, with varying As/Ga ratios was investigated⁽²⁸⁾. A linear dependence of the trap concentration on As/Ga ratio in the material which is shown in Figure 4.7 indicates the involvement of a Ga vacancy in the formation of the center. If these two centers are the same, then the 0.83 eV center in the quaternary alloys is also related to a Ga vacancy⁽²⁸⁾.

The 0.59 eV electron trap identified in $\text{p-In}_{0.81}\text{Ga}_{0.19}\text{As}_{0.05}\text{P}_{0.55}$ with a large concentration was not detected in the other quaternary, ternary, or binary materials. It is suspected that impurities incorporated during growth or subsequent processing may be responsible for the presence of the state. Electron traps with an activation energy of 0.63 eV, trap A, and 0.68 eV, trap R⁽⁶²⁾, have been consistently observed in bulk and VPE InP. However, their capture cross sections, $\sim 1 \times 10^{-14} \text{ cm}^2$, vary widely from the value of $\sigma_\infty = 1.5 \times 10^{-18} \text{ cm}^2$ measured for the 0.59 eV trap in $\text{p-In}_{0.81}\text{Ga}_{0.19}\text{As}_{0.45}\text{P}_{0.55}$. This provides further support to the fact that the center in the quaternary alloy is related to an impurity. The nature of the 0.35 eV electron trap in $\text{p-In}_{0.53}\text{Ga}_{0.47}\text{As}$ has been discussed by Bhattacharya, et al.⁽⁶³⁾ and this center is possibly related to a native defect. All the other electron traps are possibly related to impurities and more studies are needed to establish their origins. The two hole traps indentified in

LPE, 0.95 eV, and VPE, 1.19 eV, quaternary materials, with activation energies of 0.26 ± 0.01 eV, are apparently the same center. Since they appear in both LPE and VPE material, one would be tempted to associate the involvement of a native defect but further study is necessary before definite assignments can be made. This is perhaps the first identification of hole traps in epitaxial $\text{In}_{1-x}\text{Ga}_x\text{As}_y\text{P}_{1-y}$. The small values, $10^{-18} - 10^{-21} \text{ cm}^2$, of the capture cross section for some of the electron traps identified in the quaternaries could reflect their acceptor-like nature or that the capture cross sections are very strongly activated thermally.

Sasai, et al.⁽⁶⁴⁾ have detected three electron traps with thermal activation energies of 0.27, 0.30 and 0.51 eV in n- $\text{In}_{0.85}\text{Ga}_{0.15}\text{As}_{0.39}\text{P}_{0.61}$ from DLTS measurements. However, the thermal capture cross section of the traps reported by them are very different from the values of the same parameter for traps with similar activation energies identified in this investigation.

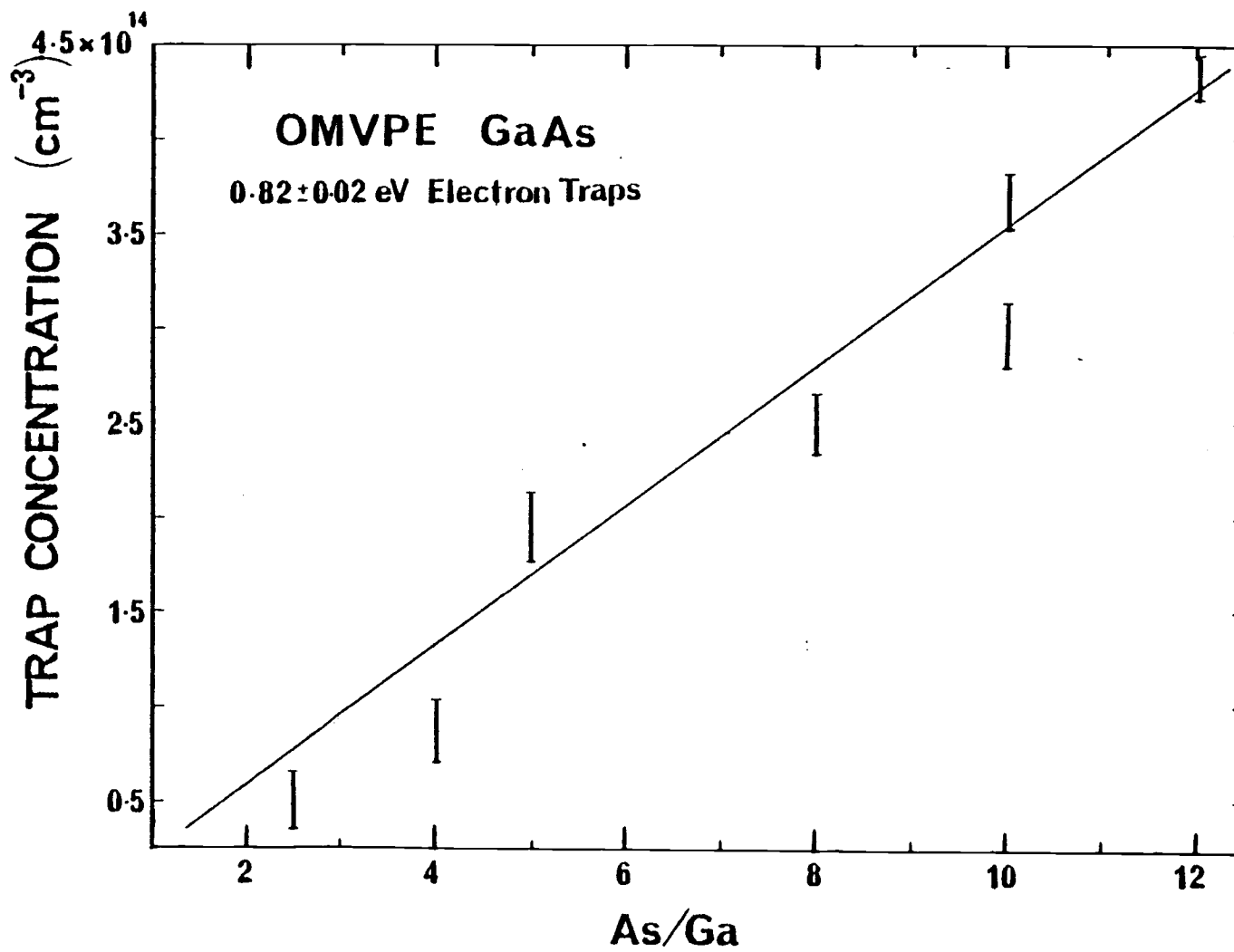


Figure 4.7. Dependence of the concentration of the dominant 0.82 ± 0.02 eV electron trap on the As/Ga ratio in the epitaxial layer. The bars indicate the dispersion in the value of N_T ⁽²⁸⁾.

CHAPTER V

TRANSPORT PROPERTIES IN $\text{In}_{1-x}\text{Ga}_x\text{As}_y\text{P}_{1-y}$

The results obtained from Hall and photo-Hall effect measurements on the quaternary epitaxial layers are presented in the first part of this chapter. The analysis of the temperature dependence of mobility and the summarized table of important transport parameters obtained from curve fittings follow thereafter. Different mechanisms involved in the carrier-scattering processes and related parameters are discussed at the end of the chapter.

5.1 Results of Hall Mobility and Carrier Concentration

The variation of the Hall mobility, μ_H , for electrons with band gap and composition at 300°K is shown in Figure 5.1 for LPE and VPE $\text{In}_{1-x}\text{Ga}_x\text{As}_y\text{P}_{1-y}$ layers. The general trend is similar for both classes of material, with the mobility going through a minimum at $E_g \sim 0.95$ eV. The scatter in the data is mostly due to the variation in the room-temperature carrier concentration which were in the range $(0.3 - 1.4) \times 10^{16} \text{ cm}^{-3}$ for the VPE layers and $(1.3 - 9.4) \times 10^{16} \text{ cm}^{-3}$ for LPE layers. A maximum room-temperature mobility of $10,000 \text{ cm}^2/\text{V}\cdot\text{s}$ was obtained for VPE $\text{In}_{0.53}\text{Ga}_{0.47}\text{As}$. The variations of μ_H with room-temperature carrier concentration in the quaternary materials are shown in Figure 5.2. Also shown in the figure are, for comparison, the results obtained by Greene, et al.⁽²⁰⁾ with LPE crystals and the mobility profiles of a set of LPE crystals⁽⁶⁵⁾ similar to those used in the present investigation. The variation of the Hall mobility with temperature in the range 20-300°K is shown in Figure 5.3. The maximum mobility occurs around 100°K for

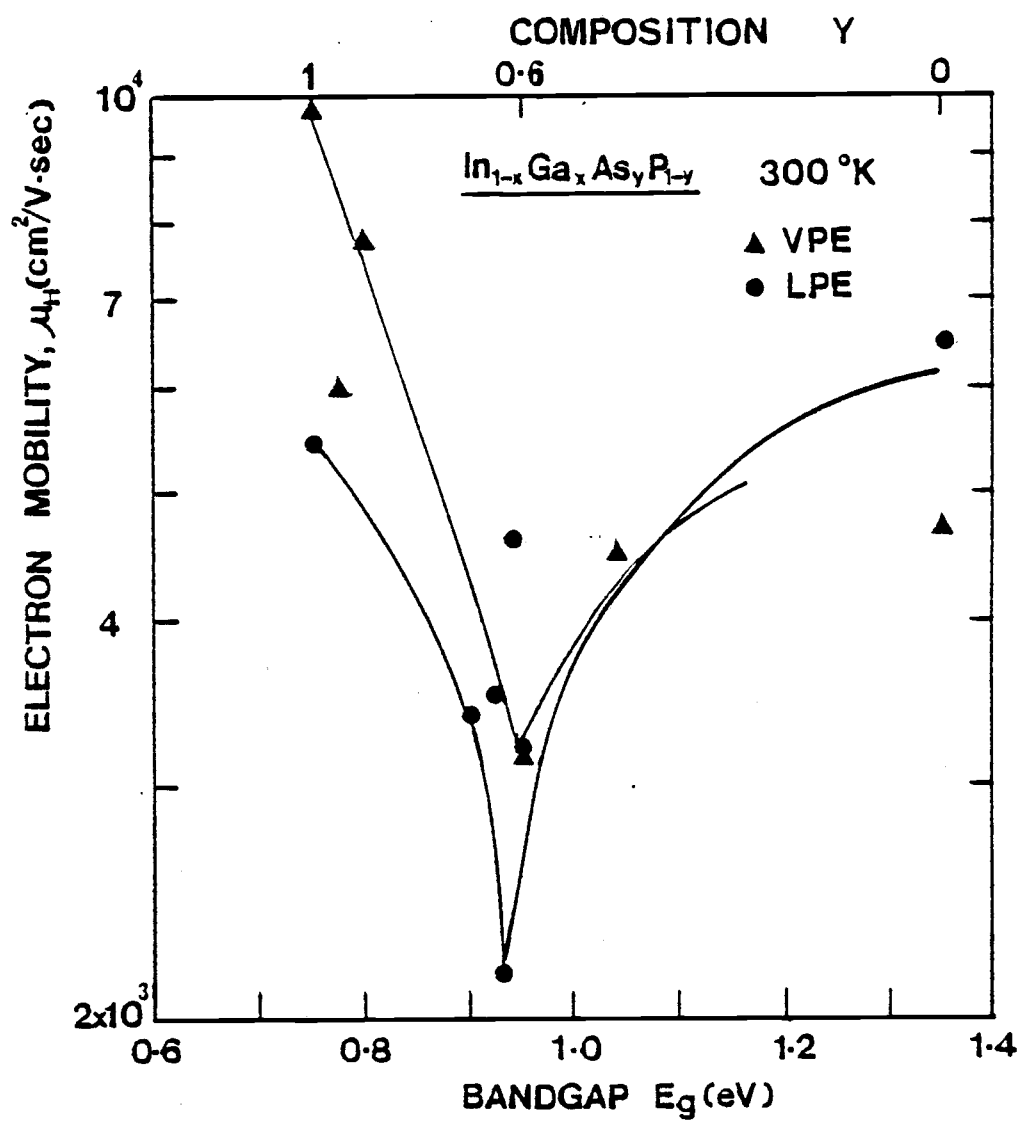


Figure 5.1. Variation of the room-temperature electron mobility with band gap (alloy composition).

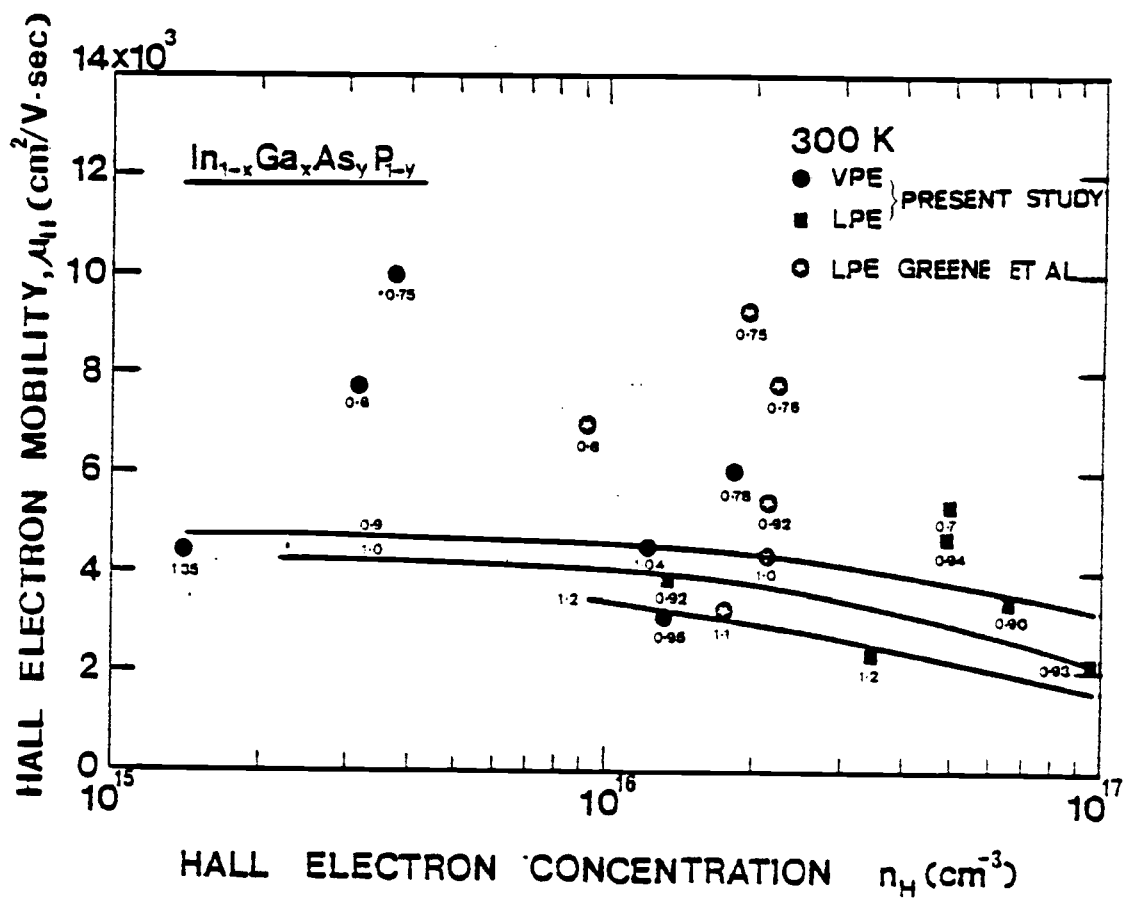


Figure 5.2. Variation of room-temperature electron mobility with carrier concentration.

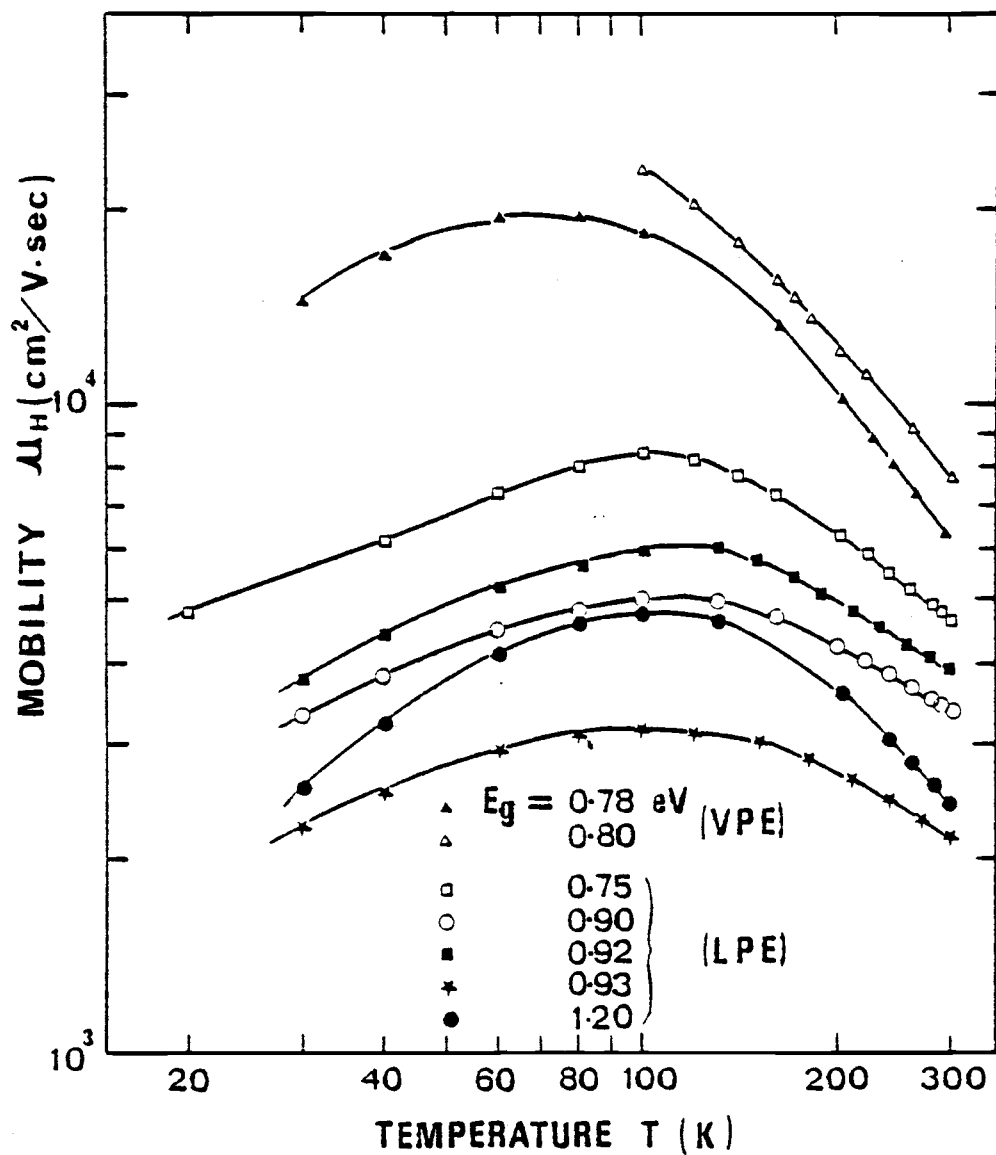


Figure 5.3. Mobility versus temperature data for LPE and VPE samples in the low temperature region.

most of the compositions. Figure 5.4(a) and (b) show the mobility variation for $T \geq 100^\circ\text{K}$. The data throughout the temperature range of $20\text{-}600^\circ\text{K}$ were recorded after an appropriate equilibration time at each temperature. The point of interest to note in the high-temperature region is the significant change in the slope of the $\mu_{\text{H}}\text{-}T$ profile for $T > 400^\circ\text{K}$ in both LPE and VPE samples having band gaps, E_{g} , in the range $0.9 - 1.0$ eV. Hall carrier concentrations, n_{H} , as a function of inverse temperature for both LPE and VPE samples are also shown in Figure 5.5. Because of the wide variation in carrier concentrations in these samples, the results of only two compositions each of LPE and VPE layers are representatively shown in this figure. It is worthwhile to point out that in the n_{H} versus $1/T$ curves, a "dip" consistently appears in a specific temperature range for samples with $E_{\text{g}} = 0.9 - 1.0$ eV. The two anomalous features, namely, the sharp fall mobility at high temperatures and a dip in n_{H} versus $1/T$ curves will be discussed in detail in the next section. The effect of illumination with monochromatic light with wavelengths corresponding to band gap and sub-band gap (0.7 eV) energies is shown in Figure 5.6 for a LPE and a VPE quaternary sample. Photoexcitation produces a pronounced decrease in the mobility of electrons in the VPE layer, indicating that a donor-like center is involved. In the case of the LPE sample, a reverse trend of the mobility upon photoexcitation indicates the presence of an acceptor-like center. The same trend has been observed in several other LPE and VPE layers. The high mobility values observed at temperatures below 100°K and the nearly constant values of n_{H} in that temperature range rule out the possibility of impurity-band conduction being responsible for the photoconductivity effect. The striking feature of

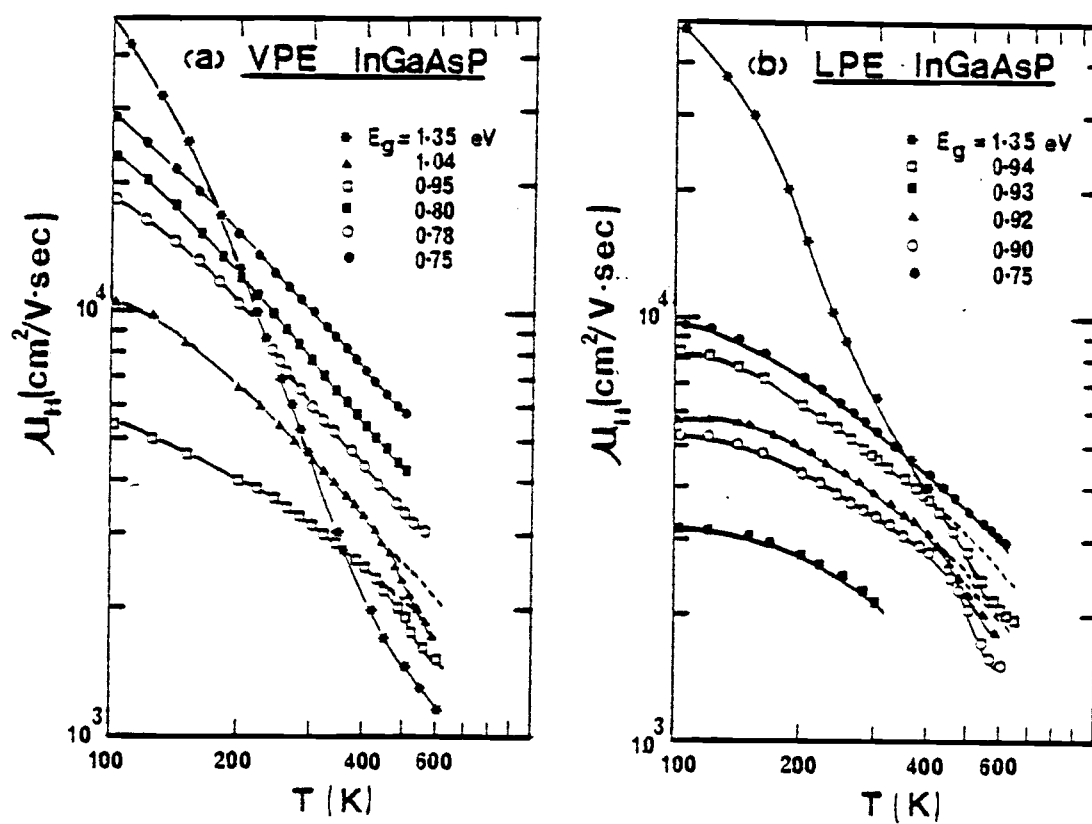


Figure 5.4. Mobility versus temperature data in the high temperature region for (a) VPE samples and (b) LPE samples.

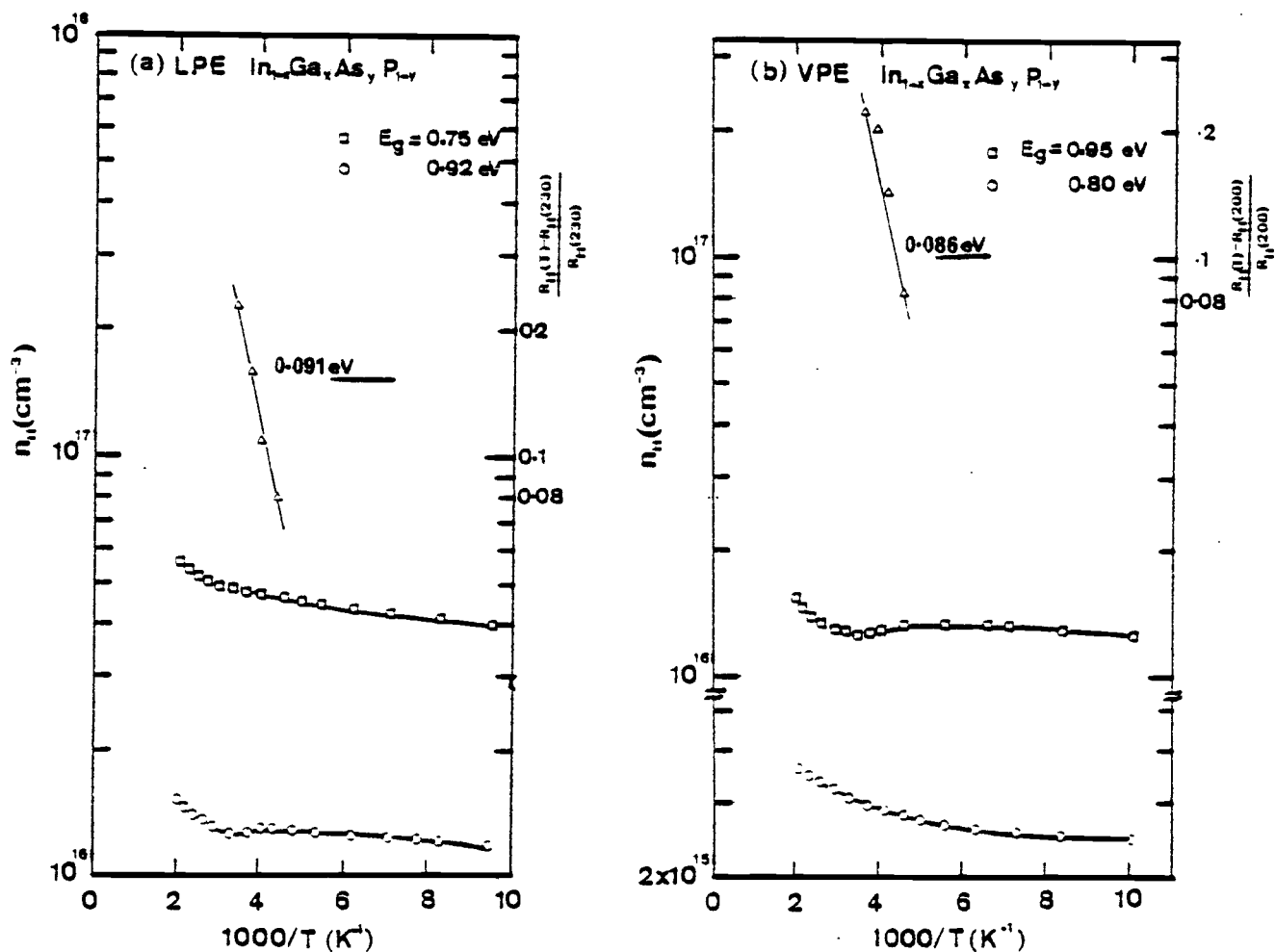


Figure 5.5. Hall carrier concentration as a function of reciprocal temperature for (a) LPE and (b) VPE quaternary samples. The fractional change in the Hall coefficient is also plotted and is fitted to lines with the slopes indicated.

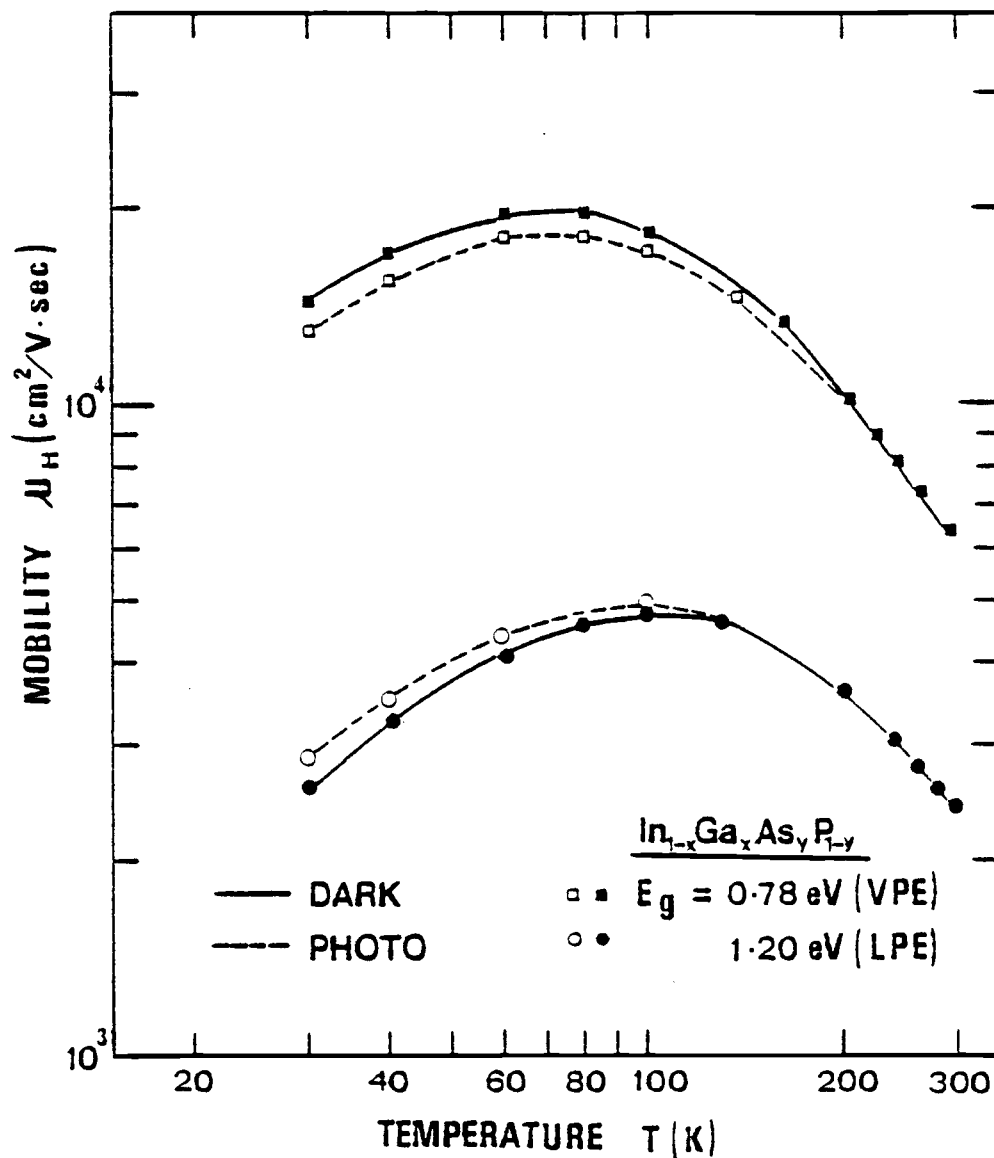


Figure 5.6. Mobility variation with temperature in LPE VPE samples in the dark and upon photoexcitation. The solid curves are for the samples in the dark, while the dashed curves are for the photoexcited case.

the observed photoconductivity is its long-term persistence.

Decay transients for n_H were recorded at different temperatures and their dependence on inverse temperature is shown in Figure 5.7, where an exponential decay rate has been assumed. The results suggest that the centers in LPE and VPE material have an almost identical energy barrier of ~ 0.2 eV to electron capture. The Hall and photo-Hall mobilities coincide at a fairly high temperature; indicating that deep centers may be involved.

5.2 Analysis of Transport Data

The temperature dependence of the electron mobilities were fitted by theoretical estimates taking into account the different scattering mechanisms. The different mechanisms considered were ionized impurity, polar-optical phonon, space charge, piezoelectric, and deformation potential scattering. In addition, alloy scattering⁽⁶⁶⁾, which accounts for the deviations from the perfect periodicity of the virtual crystal model, has also to be considered. The relaxation time and mobility due to these scattering processes are discussed in detail in Appendix A.

The theoretical electron mobility due to the combined effect of all the scattering processes was determined by Matthiesen's rule

$[\mu_d]^{-1} = \sum_j [\mu_j]^{-1}$, where the μ_j 's are the mobilities due to the individual scattering processes. The quaternary material parameters required in these equations were estimated from the binary parameters using an interpolation scheme⁽¹⁵⁾. According to this scheme, a quaternary parameter Q can be expressed as

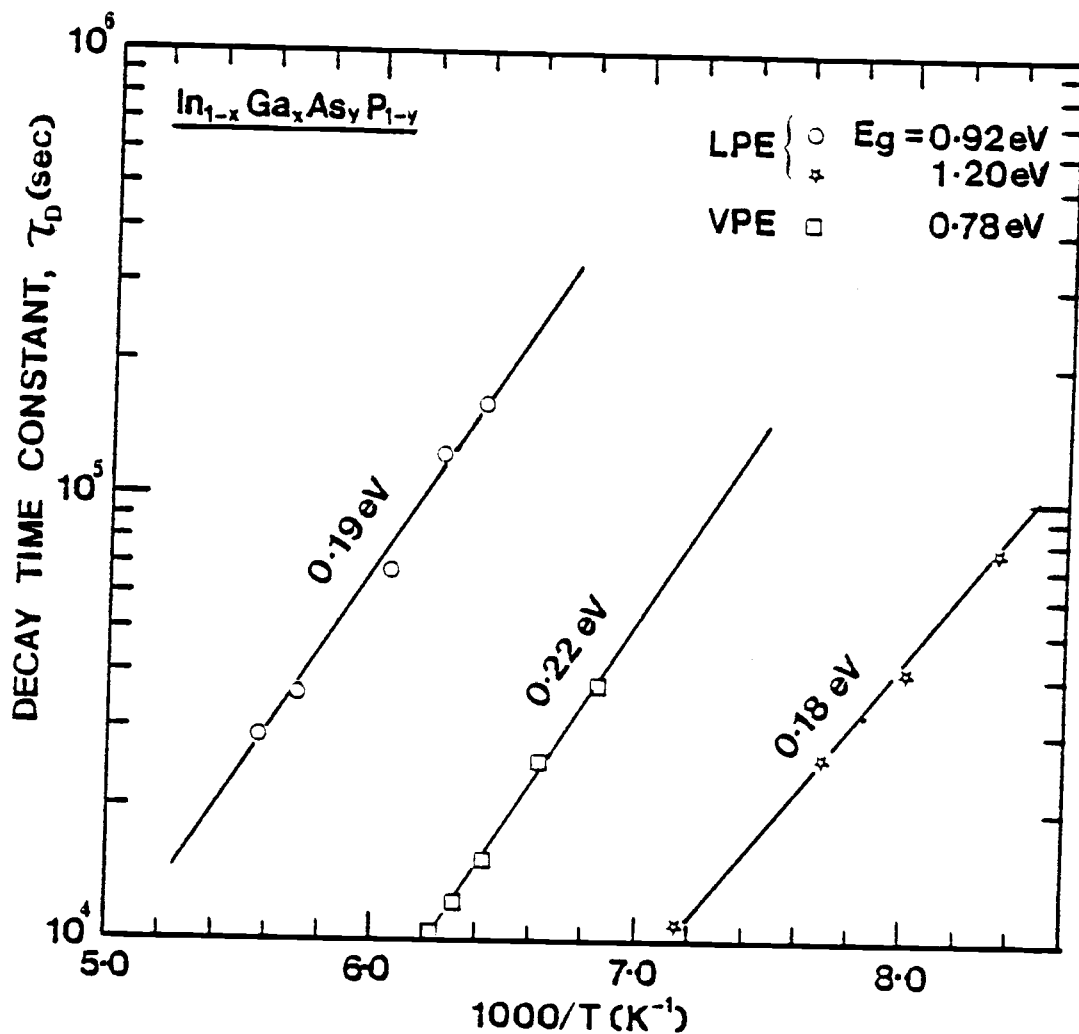


Figure 5.7. Temperature dependence of the decay time constant of the photoexcited carrier concentration assuming an exponential decay law. The slope of the plots is an estimate of the energy barrier associated with carrier capture by the centers.

$$Q(x,y) = \{x(1-x)[(1-y)T_{12}(x)+yT_{43}(x)] + y(1-y)[(1-x)T_{14}(y)+xT_{23}(y)]\} \cdot [x(1-x)+y(1-y)]^{-1} \quad (5.1)$$

where T_{ij} is the material parameter for the ternary alloy formed by binaries i and j . Here, InP, GaP, GaAs, and InAs are the materials 1, 2, 3, and 4, respectively. As an example, $T_{12}(x)$ is a material parameter for $\text{In}_{1-x}\text{Ga}_x\text{P}$. It is assumed that the electrons are scattered in a parabolic band. In order to compare the theoretically estimated mobility with the experimentally determined Hall mobility μ_H throughout the entire temperature range, it is important to know the value of the scattering factor $r(=\mu_H/\mu_d)$, where μ_d is the drift mobility). Hall measurements were performed at both low and high (5T) magnetic fields at 300° and 480°K. The value of r was found to be in the range 1.0 - 1.05 for two quaternary compositions, and such values justify the comparison of the theoretically estimated and experimentally determined mobilities. The variation of r with magnetic field for a sample with $E_g = 1.04$ eV is shown in Figure 5.8. Values of $r = 0.98 - 1.00$ were also obtained by Greene, et al.⁽²⁰⁾ in LPE quaternary layers ($E_g = 0.76 - 0.95$ eV). Alloy scattering does not have to be considered in InP, but from measurements in this study and the data of Hilsum and Rees⁽⁵³⁾, r is known to vary from 1.06 to 1.17 in the temperature range of interest. This variation has been taken into account in the analysis of the mobility data for InP.

Reasonably good fits to the experimental mobility data could be obtained over the temperature range 20-300°K for the LPE and VPE layers. The continuous traces in Figures 5.3 and 5.4 indicate the theoretical fits to the experimental data indicated by the symbols. The experimental

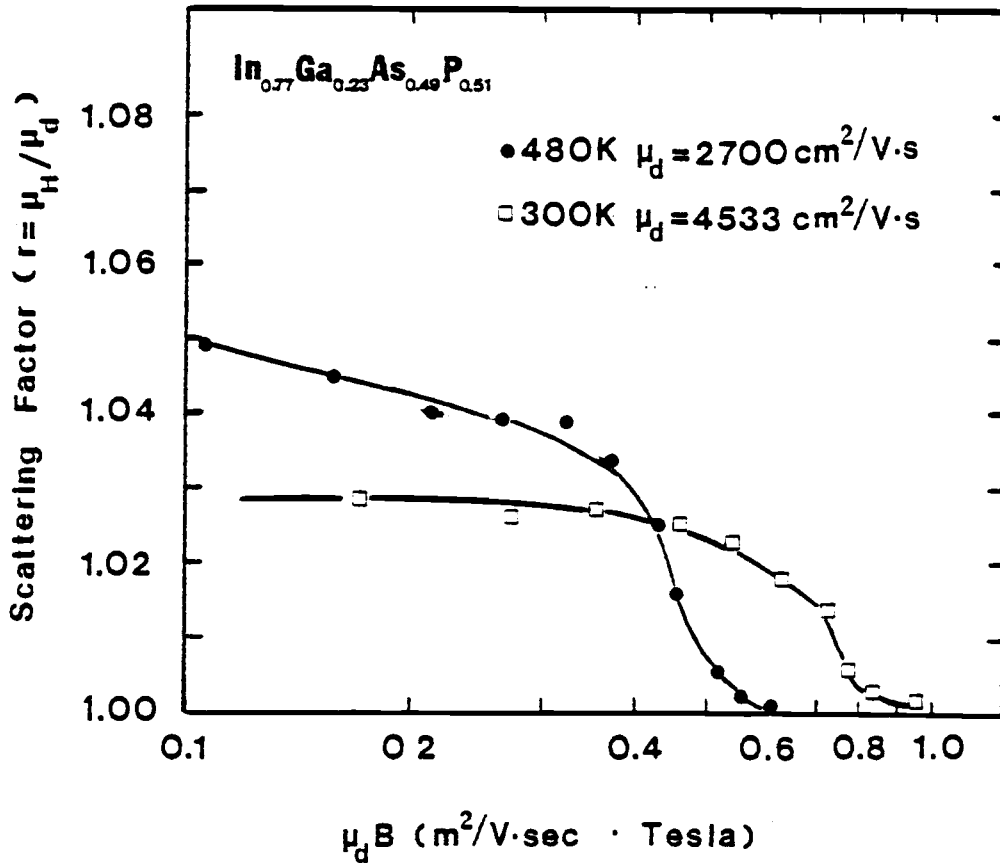


Figure 5.8. Hall scattering factor versus $\mu_d B$ in $\text{In}_{0.77}\text{Ga}_{0.23}\text{As}_{0.49}\text{P}_{0.51}$ ($E_g = 0.95$ eV).

and calculated mobilities for $\text{In}_{0.67}\text{Ga}_{0.33}\text{As}_{0.71}\text{P}_{0.29}$ ($E_g = 0.9$ eV) is shown in Figure 5.9. It is clear that the effects of including piezoelectric and deformation potential scattering are very small and space charge scattering cannot be neglected. Values of the transport parameters which were used to achieve a good fit to the experimental mobilities for the different compositions are listed in Table 5.1. It was not possible to fit (as illustrated by the dashed lines) the mobility variation for $T \geq 400^\circ\text{K}$ for the samples in which a sharp fall in mobility had been recorded. An attempt was made to replace space charge scattering in the analysis by a central-cell correction⁽⁶⁸⁾ of the ionized impurity which also has the same temperature dependence at high temperatures:

$$\mu_{cc} = \frac{3.4 \times 10^{20}}{N_A} \left[\frac{15}{8} (kT)^{1/2} + \frac{E_A}{(kT)^{1/2}} \right] \text{ cm}^2/\text{V}\cdot\text{sec} \quad (5.2)$$

where E_A and N_A are, respectively, the ionization energy and concentration of acceptors. The agreement with experimental data was worse. The values of the alloy scattering potential ΔU as a function of mixed alloy composition are of interest. This parameter has been plotted in Figure 5.11 as a function of E_g and the alloy composition y . The maximum value of ΔU occurs for $E_g \sim 0.95$ eV, or $y \sim 0.6$ which also corresponds to the minimum of the μ_H versus E_g curves (see Figure 5.1). The results show that alloy scattering is most dominant in limiting the electron mobilities in the quaternary crystals with $E_g \sim 0.95$ eV. The rapid fall of the mobility with temperature for $T \geq 400^\circ\text{K}$ observed in some samples with $E_g = 0.9 - 1.0$ eV has not been observed before. The possibility of increased substrate conduction with increasing temperature has been

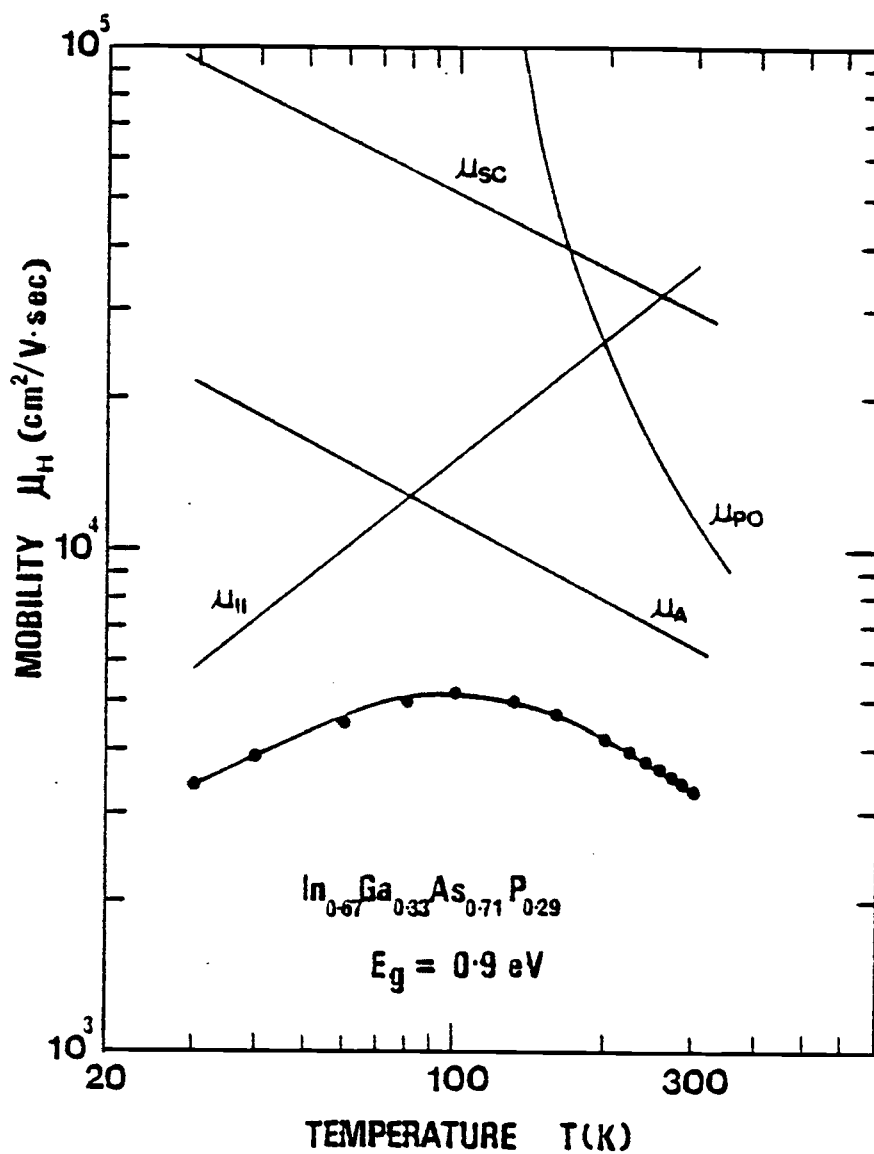


Figure 5.9. Experimental and calculated mobilities as a function of temperature in $\text{In}_{0.67}\text{Ga}_{0.33}\text{As}_{0.71}\text{P}_{0.29}$.

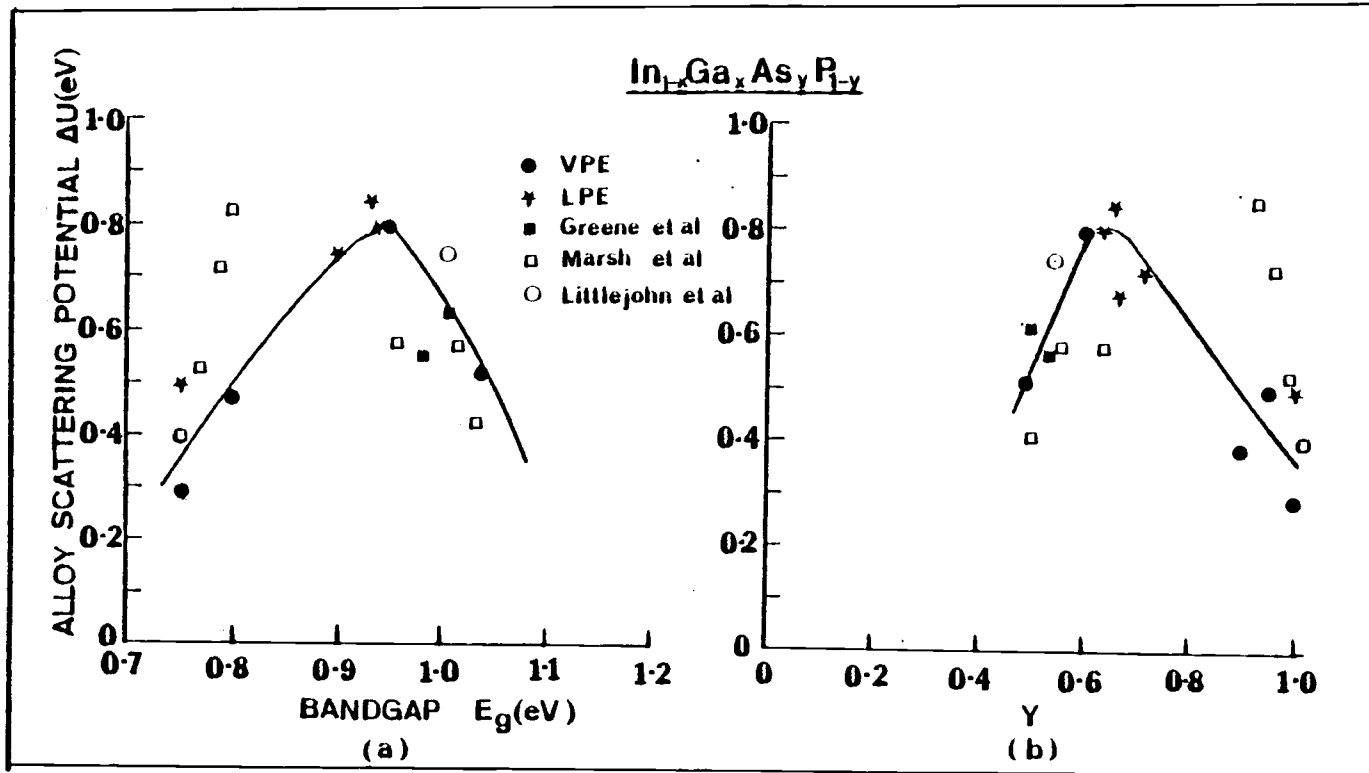


Figure 5.10. Variation of the alloy scattering potential with (a) band gap E_g , and (b) alloy composition y .

considered and the measurements were repeated for two LPE and VPE layers in which the substrates were thinned considerably. The same effect was observed. It is believed that the measurements reflect, at least in part, properties of the epitaxial layer. A similar mobility behavior has been observed in GaAs⁽⁶⁹⁾ for $T > 650^\circ\text{K}$ when electrons transfer from the central conduction valley to the higher satellite valleys. Since the next higher valleys in the $\text{In}_{1-x}\text{Ga}_x\text{As}_y\text{P}_{1-y}$ alloys have been estimated to be around 0.7 eV from Monte Carlo calculations⁽¹⁵⁾, it is inconceivable that substantial intervalley electron transfer would occur at temperatures $400^\circ \leq T \leq 600^\circ\text{K}$. The striking feature in Figure 5.5 is that for alloys with $E_g = 0.9$ to 1.0 eV, n_H shows a marked decrease in a certain temperature range which is similar to the "dip" recorded by Blood in GaAs⁽⁶⁹⁾ due to electron transfer to higher valleys. The same effect was observed for the samples on thinned substrates. The anomalous mobility and concentration data in the quaternary samples may be due to the thermal transfer of electrons from the central valley to a localized defect level, situated in the intervalley region and having a high density of states. Following Aukerman and Willardson⁽⁷⁰⁾, the quantity $(R_H - R_0)/R_0$ has been plotted against inverse temperature, as illustrated in Figure 5.5 where $R_0 = R_H(230^\circ\text{K})$, or $R_H(200^\circ\text{K})$. R_0 is the value of the Hall coefficient when all the carriers are in the central minimum and R_H is the value of the coefficient when carrier transfer is operational. From the figure it is evident that the process follows an exponential law expressed as

$$\frac{R_H - R_0}{R_0} \propto \exp(-\Delta E/kT) \quad (5.3)$$

TABLE 5.1. Parameters for the analysis of the temperature variation of Hall mobility

	Material Band Gap at 300°K (eV)	Ionized Impurity Density ($N_A + N_D$) cm^{-3} at 300°K	Acoustic Deformation Potential, E_1 (eV)	$N_S \cdot A$ (cm^{-1}) ($\times 10^4$)	Alloy Scattering Potential at 300°K, ΔU (eV)
VPE	0.75	4.8×10^{15}	6.62	2.6	0.29
	0.775	9.3×10^{15}	6.66	2.7	0.50
	0.80	2.8×10^{15}	6.62	4.0	0.48
	0.95	3.2×10^{16}	6.79	1.0	0.80
	1.04	2.0×10^{16}	6.86	0.9	0.51
	1.35	1.3×10^{15}	6.50	1.1	-
LPE	0.75	5.0×10^{16}	6.62	2.9	0.50
	0.90	1.1×10^{17}	6.85	3.3	0.72
	0.92	7.0×10^{16}	6.87	1.0	0.68
	0.93	1.7×10^{17}	6.87	1.0	0.85
	0.94	1.1×10^{17}	6.83	1.8	0.80
	1.35	2.5×10^{15}	6.50	0.1	

and a value of ~ 0.09 eV for ΔE is obtained. This indicates that the defect level is probably located 0.09 eV above the central conduction minimum.

5.3 Discussion

The experimental results indicate that a maximum mobility of $\sim 10,000$ cm²/V.sec (room temperature) is obtained in $\text{In}_{0.53}\text{Ga}_{0.47}\text{As}$ ($y=1$). This is in agreement with the results of Leheny, et al.⁽⁷¹⁾, but disagree with the calculations of Littlejohn, et al.⁽¹⁵⁾, who predict a maximum mobility for alloys with $y = 0.8$. Furthermore, none of these authors obtain a sharp minimum in μ_H for $y = 0.6$ as found in this investigation. The variation of ΔU with band gap (composition) obtained by fitting the temperature variation of mobility seems to explain the observed values of μ_H at room temperature. Our values of ΔU agree fairly well with the results of Littlejohn, et al.⁽²²⁾ and Greene, et al.⁽²⁰⁾ but Marsh, et al.⁽⁷²⁾ obtained lower values for this parameter. The results of these authors are also shown in Figure 5.10 for comparison.

The strong persistent photoconductivity exhibited by the donor- and acceptor-like centers indicate that a barrier involving some lattice relaxation is involved during carrier capture. Centers with large barrier energies exhibiting strong persistent photoconductivity have also been identified in undoped and doped $\text{Al}_x\text{Ga}_{1-x}\text{As}$ crystals. The properties of the centers in the ternary alloys will be discussed in detail in Chapter VI. There is considerable likelihood of the presence of large clusters of localized defects in the quaternary lattice. Such defects may cause fluctuations of the band-edge and impurity po-

tentials and give rise to states above the minima which are essentially continuations of the band profile. The anomalous transport data at high temperatures could be indicative of electron transfer to such states. The "dip" in the Hall concentration data, n_H , could also be an indication of carrier transfer to localized states. However, the temperature range in which a lowering of the value of n_H is recorded is slightly lower than the range in which the mobility exhibits a sharp fall. The discrepancy may be due to the prevailing substrate conduction. The lowering in the value of n_H could have been more severe and extended over a larger temperature range if substrate conduction could be completely eliminated.

It has been assumed that all the scattering mechanisms are independent of each other. This is not strictly valid since, for example, an electron-phonon collision can occur while the electron is traversing the field due to an ionized impurity. Also, it has been assumed that the total relaxation time can be defined as $[\sum_j [\tau_j]^{-1}]^{-1}$ which also is not strictly true since a relaxation time cannot be defined for electron scattering by polar optical modes.

CHAPTER VI

DEFECT CENTERS IN LPE Ga_{1-x}Al_xAs

The electrical properties of LPE Ga_{1-x}Al_xAs are dominated by non-shallow defect centers which appear in nonintentionally and intentionally doped crystals and behave as electron trapping centers. Previous work related to these defect centers is reviewed in Sec. 6.1. The results of optical lineshape, thermally stimulated capacitance, and Hall-effect measurements on unintentionally doped LPE Ga_{1-x}Al_xAs layers are presented in Sec. 6.2. The results from the photoionization cross section spectra are analyzed in Sec. 6.3 and discussed in Sec. 6.4, where the thermal and optical emission processes from the defects have been explained. Finally, a model for the microstructure of the defect is presented.

6.1 Review of the Defect Properties6.1.1 Electrical Properties

When Hall measurements were performed on n-type LPE samples of Ga_{1-x}Al_xAs as a function of temperature, the profile of the Hall electron concentration, n_H , as a function of inverse temperature shows a sharp decrease with lowering of temperature. This occurs just below 250°K and indicates a trapping of electrons from the conduction band to non-shallow centers in the forbidden gap. Similar behavior has been observed both in nonintentionally⁽⁷³⁾ and intentionally^(74,75) doped crystals. Detailed analyses of the Hall-effect data using a multiconduction band model⁽⁷³⁾ yield the binding energy of the defect centers with respect to the conduction band edge and their concentration. The

latter parameter has a value nearly equal to the total electron concentration, showing that the defect level plays a dominant role in contributing electrons to the conduction band. The same is true for the doped crystals⁽⁷⁵⁾. The striking feature is that the binding energy changes with composition: it increases monotonically for $x \geq 0.25$, reaches a maximum near the band cross-over composition region, and then decreases monotonically. In the same nonintentionally doped crystals as used by Saxena⁽⁷³⁾, the profiles of the depth of the nonshallow levels determined from capacitance-voltage measurements⁽⁶⁰⁾ and hydrostatic pressure experiments⁽⁷⁶⁾, as shown in Figure 6.1, agree well with the binding energies obtained from Hall measurements. However, the defect binding energies in intentionally doped crystals, as determined by SpringThorpe, et al.⁽⁷⁴⁾ (Te), Kaneko, et al.⁽⁷⁷⁾ (Sn), Nelson⁽⁷⁵⁾ (Te), Balland, et al.⁽⁷⁸⁾ (Sn) and Dingle, et al.⁽⁷⁹⁾ (Te), have marked differences from those in nonintentionally doped ones. These differences are highlighted in Figure 6.2.

The thermal activation energies of the nonshallow defects in intentionally doped LPE crystals have been determined from DLTS measurements by Lang, et al.^(80,81) and Balland, et al.⁽⁷⁸⁾. This energy was measured to be ~ 0.30 eV by Lang and Logan⁽⁸⁰⁾ in Te-doped samples. Samples doped with Sn exhibited two DLTS peaks. The Si-related defect center was deeper than those related to Te or Se. Lang, et al.⁽⁸¹⁾ report, however, that in their nonintentionally doped samples the defect was absent. Their result is in conflict with the results of Bhattacharya, et al.⁽⁶⁰⁾ and of this investigation, which will be discussed in detail in the next section. The reason is not clearly understood. Balland, et al.⁽⁷⁸⁾ have also identified and characterized

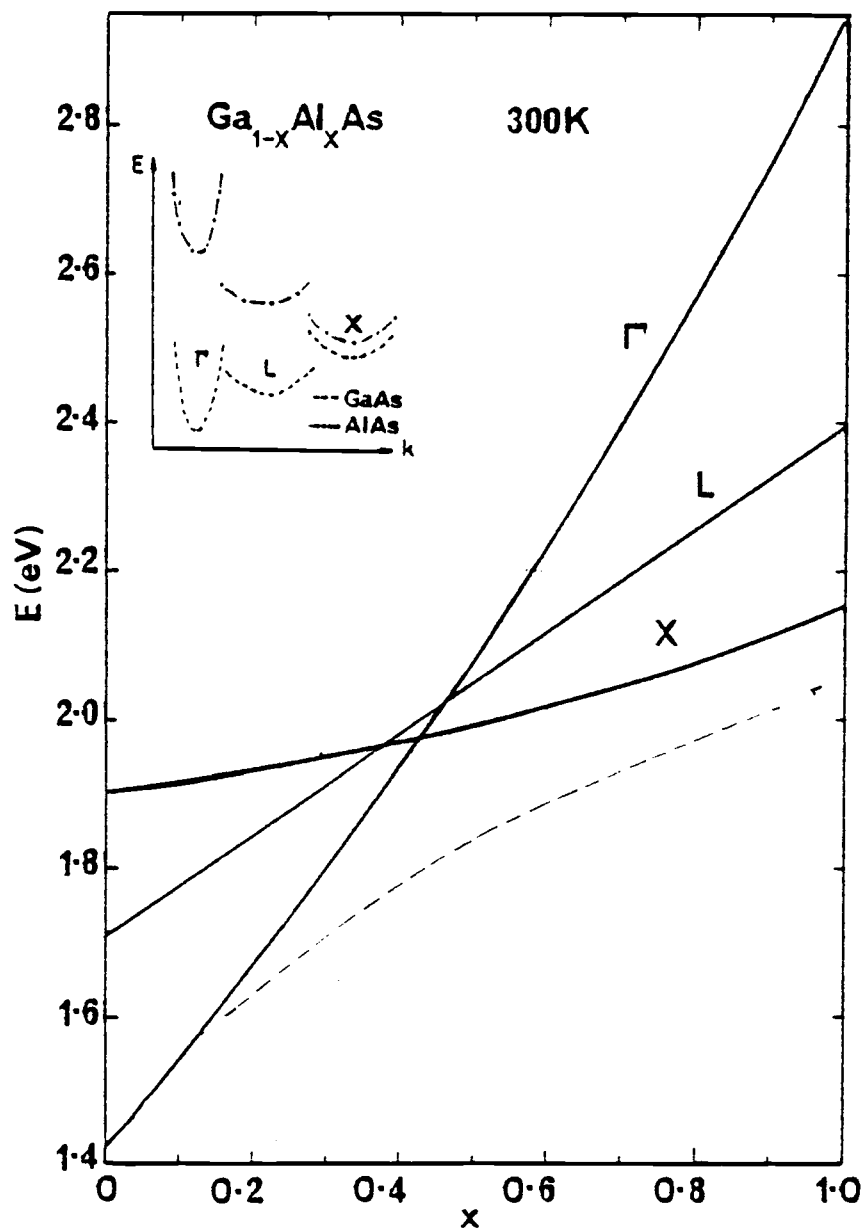


Figure 6.1. The conduction band structure at 300°K and the energy position of defect levels in LPE $\text{Ga}_{1-x}\text{Al}_x\text{As}$ (60,76).

two donor levels in Sn-doped LPE $\text{Ga}_{1-x}\text{Al}_x\text{As}$. Their respective activation energies in a layer with $x = 0.35$ are 0.2 ± 0.02 and 0.13 ± 0.03 eV. The deeper donor exhibited persistent photoconductivity and had an activation energy similar to that measured for defects in nonintentionally doped $\text{Ga}_{1-x}\text{Al}_x\text{As}$ ⁽⁶⁰⁾.

6.1.2 Optical Properties

In both intentionally and nonintentionally doped LPE $\text{Ga}_{1-x}\text{Al}_x\text{As}$ crystals, there is a large increase in the value of n_H upon photoexcitation with 1.1 - 1.2 eV radiation^(75,81). This photoconductivity is extremely persistent (\sim hours for $T < 60^\circ\text{K}$) and can only be quenched by raising the temperature of the sample. By measuring the decay rate of the free-electron concentration, the energy barrier which gives rise to the persistent photoconductivity effect has been estimated to be ~ 0.2 eV by Nelson⁽⁷⁵⁾. The deep donor level with an activation energy of 0.2 eV identified by Balland, et al.⁽⁷⁸⁾ in Sn-doped LPE $\text{Ga}_{1-x}\text{Al}_x\text{As}$ also exhibited a similar persistent photoconductivity effect. Significant changes have also been observed in the value of the electron mobility in doped samples upon photoexcitation at low temperatures⁽⁷⁵⁾. These will be discussed later in the context of photo-Hall measurements performed on nonintentionally doped LPE samples in the present investigation.

The facts which emerge from these experiments are that the non-shallow defects, which behave as electron traps, exhibit apparently similar behavior in intentionally and nonintentionally doped LPE crystals, but their detailed characteristics differ. The measurements on the nonintentionally doped LPE layers in this investigation were

therefore thought to be necessary for a further understanding of the observed differences.

6.2 Experimental Results

6.2.1 Hall and Photo-Hall Measurements

The inverse Hall coefficient and electron mobility in nonintentionally doped LPE $\text{Ga}_{1-x}\text{Al}_x\text{As}$ were determined using the van der Pauw technique with a magnetic flux density of 0.5 Tesla. The details of these measurements have been described in Chapter III. Measurements were restricted only to a few crystal compositions, since the intent was not a detailed study of the transport properties as a function of composition, but a determination of the donor- or acceptor-like nature of the defect levels. The electron mobilities as a function of temperature in crystals with compositions $x = 0.48$ and 0.61 in the dark and upon photoexcitation are shown in Figure 6.3. The dashed and solid curves indicate, respectively, the photoexcited and dark mobility values. The dashed curve was retraced even when the photoexcitation was kept on while raising the temperature and with photoexcitation of different photon energies ($0.7 \leq h\nu \leq 1.1$ eV). The data indicate that the observed photoconductivity is of a persistent nature and can only be quenched thermally. Similar effect has been found in intentionally doped LPE crystals, except that there was a decrease in mobility upon photoexcitation.

6.2.2 Thermally Stimulated Capacitance Measurements

The experimental details of TSC measurements have been described in Chapter III. Only the results will be presented here. The

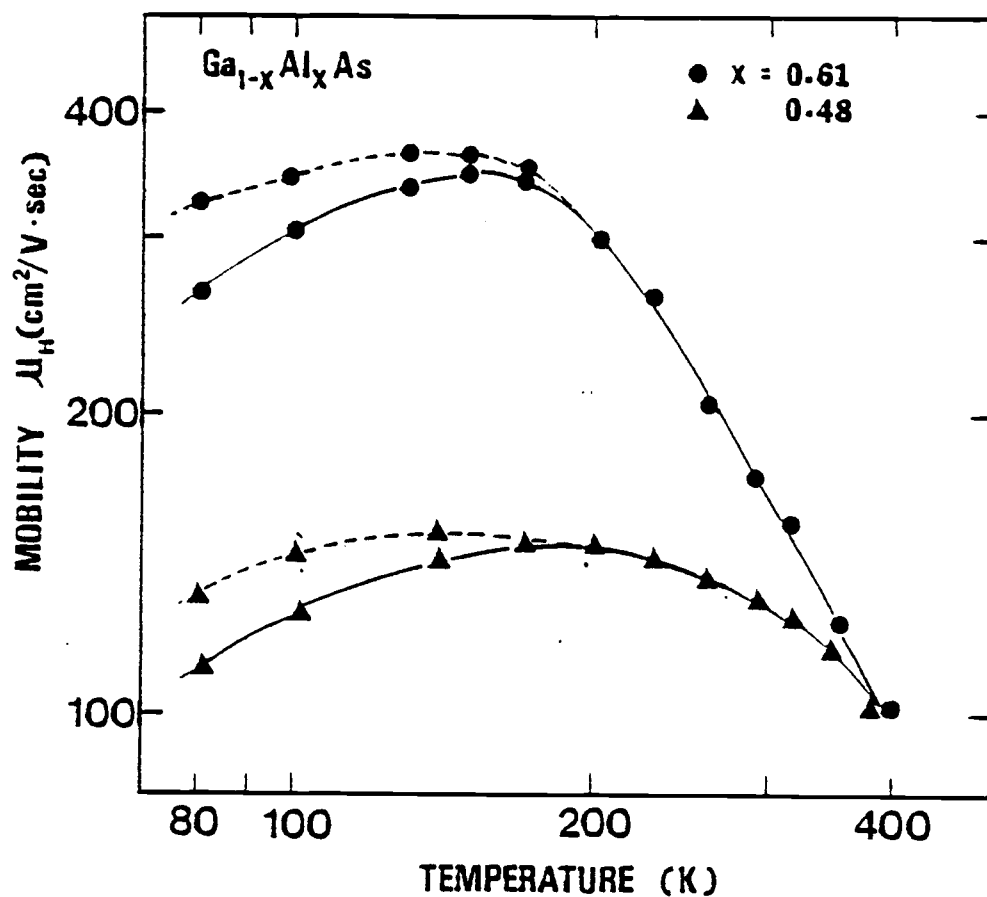


Figure 6.3. Variation of electron mobility with temperature. The solid curves are for the samples in the dark, while the dashed curves were obtained after photoexcitation.

capacitance-temperature profiles which describe the typical behavior in four composition ranges of nonintentionally doped LPE $\text{Ga}_{1-x}\text{Al}_x\text{As}$ crystal are depicted in Figure 6.4. These composition ranges are (i) $x < 0.25$, where the nonshallow level is not detected by DLTS, (ii) $0.25 \leq x \leq 0.36$, where the binding energy of the level monotonically increases, but the thermal activation energy remains constant, (iii) $0.37 \leq x \leq 0.5$, where the conduction valleys come close to each other in energy and eventually cross over and the depth of the level reaches a maximum and (iv) $x > 0.50$, the indirect band gap region where the binding energy and thermal activation energy of the level monotonically decrease. For the sample with $x = 0.19$ the capacitance values for the three steps coincide throughout the temperature range and there is no change with application of a forward bias or irradiation. This confirms that the nonshallow defects are absent and the slight lowering of capacitance with lowering of temperature is due to the change in the position of the Fermi level and partial filling of shallow donors. For the sample with $x = 0.25$, the capacitance profiles for the three steps can be separately seen. For $x = 0.47$ there is a sharp fall in capacitance with lowering of temperature, and no change is observed on application of a forward bias. The same features are observed for the crystal with $x = 0.78$, but the slope of the capacitance change has decreased. There are several important features to be noted in these curves. The largest slope for the capacitance change is observed in the sample with $x = 0.47$. This confirms that amongst the four compositions the deep level has the largest binding energy at $x = 0.47$. A distinct capacitance profile for step 2 is seen only for $x = 0.25$ and not in the samples with higher values of x . Step 2 denotes the condition when all the centers are

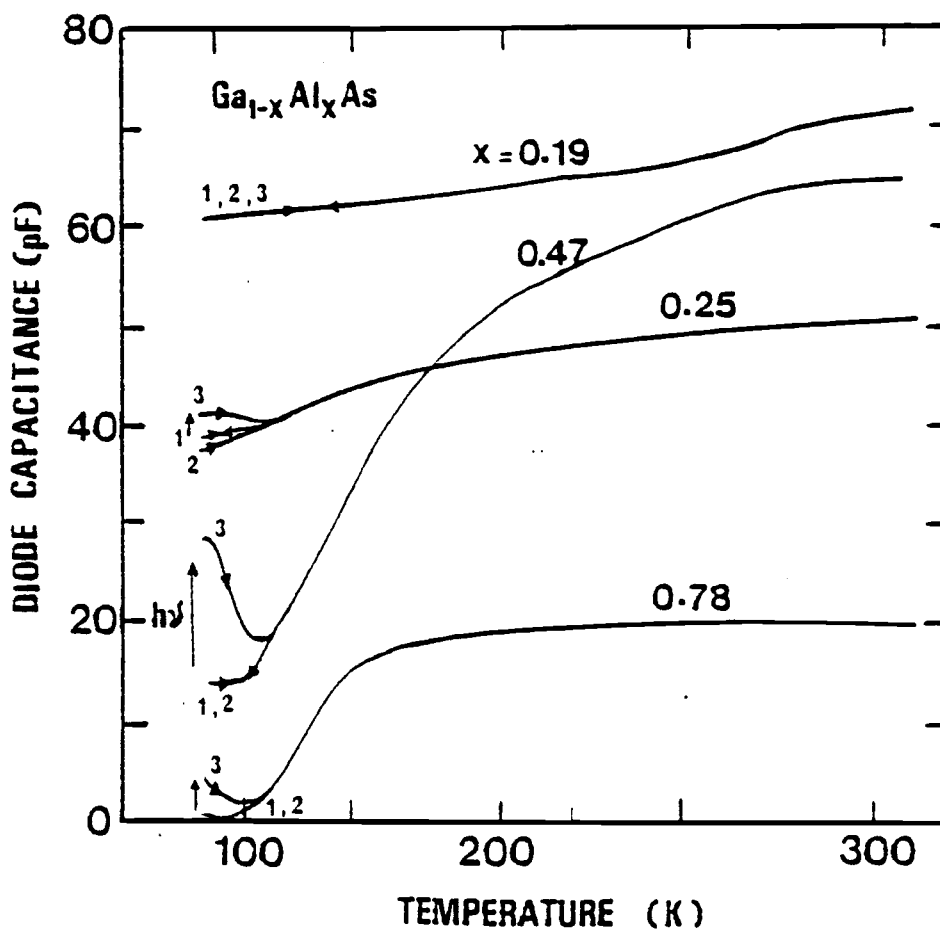


Figure 6.4. Thermally stimulated capacitance data for samples of nonintentionally doped LPE $\text{Ga}_{1-x}\text{Al}_x\text{As}$ with varying compositions. The significance of the different steps has been outlined in the text.

filled with the application of a forward bias. Step 3 is most pronounced for the sample with $x = 0.47$. This step represents the thermal quenching of persistent photoconductivity after the centers are optically emptied by irradiation at 80°K . Finally, the value of the diode capacitance at 80°K for step 1 (or step 2 if it is observed) progressively decreases from $x = 0.19$ to $x = 0.78$, where it attains a very low value. This indicates an increased dominance of the nonshallow level, into which carriers freeze out, in determining the concentration of electrons in the conduction band. The experimental observations outlined above can be consistently explained by the following model. When the nonshallow defect level is present, the Fermi level at room temperature is close to and just below it in the forbidden energy gap. With lowering of temperature, the Fermi level moves closer to the conduction band, thereby partially ($x = 0.25$) or completely ($x = 0.47$ and 0.78) filling the level with electrons. In the latter, no more centers can be filled with the application of a forward bias and a separate profile for step 2 will not be observed. Lang, et al.⁽⁸²⁾ have performed similar experiments with Te-doped LPE $\text{Ga}_{1-x}\text{Al}_x\text{As}$ where a large difference in capacitance was observed between steps 1 and 2 in the low temperature limit. Consequently, in the Te-doped samples there is possibly a lesser dominance of shallow donors, and probably a larger compensation, both of which would fix the equilibrium Fermi level lower in energy in the forbidden gap. Thus a lowering of temperature is not sufficient to fill all the nonshallow defect centers.

6.2.3 Electron Photoionization Cross Section

When the sample was illuminated by the monochromatic light during the thermally stimulated capacitance measurements, the optical emptying of the centers from steps 1 to 3 in Figure 6.4 follows the exponential law expressed by Eqn. (2.18). The resulting capacitance change would be exponential only for a small trap density. However, in the present case $N_T \geq N_D$, the shallow donor density, and the capacitance transients are expected to be highly nonexponential. Capacitance transients due to thermal emission from traps of large density can be approximated by an exponential law at large values of time (closer to saturation). Such "long" time constants derived from the transients due to optical emission have been used to determine the emission rates to which they are related by $\tau_n^0 = 1/e_n^0$. The experimental results of Lang and Logan⁽⁸⁰⁾ also indicated nonexponential transients. The experimental procedure for measuring the photoionization cross sections has been described in detail in Chapter III. The measured cross sections as a function of excitation energy for the nonshallow level in crystals with varying alloy composition are illustrated in Figures 6.5 to 6.8 by the various symbols. The data have been normalized to unity at 1.2 eV to 1.4 eV, depending on composition. The bold lines are theoretical fits to the data using models which are discussed in the next section.

6.3 Analysis of Optical Lineshape Data

Theoretical fitting of the experimental photoionization cross section data was done in order to determine the parameters which define the nonshallow defects. The theoretical optical lineshapes obtained from Lucovsky's model⁽⁴¹⁾ are shown by the solid curves in Figures

6.5 and 6.6 for $x = 0.32$ and 0.50 , respectively. The value of m_T , which is the mass of the bound electron, was chosen to be equal to m_0 for the analysis. Only two representative compositions, both in the direct and indirect energy band gap regions, were chosen because of the absence of any significant change in the experimental values of $\sigma(h\nu)$ with composition. The scatter in the experimental data is attributed to experimental factors. Values of $E_n = 0.80 \pm 0.05$ eV, represented by the shaded regions, are obtained from the theoretical lineshapes. The dashed curves indicate the lineshapes for $m_T = m_d$. The electron density-of-state effective masses in the different conduction minima in $\text{Ga}_{1-x}\text{Al}_x\text{As}$ are discussed in Appendix B. The deterioration of the agreement with the experimental data confirms that all the masses of carriers involved cannot be taken equal to the effective mass in the band to which carriers are excited.

The theoretical fits to the experimental values of $\sigma(h\nu)$ using the model of Huang and Rhys⁽⁴³⁾ are shown in Figures 6.7 and 6.8 for the direct and indirect band gap compositions, respectively. The compositions chosen were $x = 0.32$ and the parameters used were $T = 90^\circ\text{K}$, $\hbar\omega = 30.0$ meV, $E_p = 5.2$ eV, $E_F = 11.5$ eV, $E_0 = 0.12 \pm 0.05$ eV and the Franck-Condon shift, $d_{FC} = 0.75 \pm 0.05$ eV. The shaded regions represent the range of values for d_{FC} . The temperature dependence of the band gap in GaAs^(60,83) was assumed to calculate E_g at 90°K from the values of E_g at 2°K ⁽⁷⁹⁾ for the two compositions. Specifically, the expression used was⁽⁸³⁾:

$$E_g = E_g(2^\circ\text{K}) - (5.4 \times 10^{-4} \text{ eV.K}^{-1})T^2/(T+204) \quad (6.1)$$

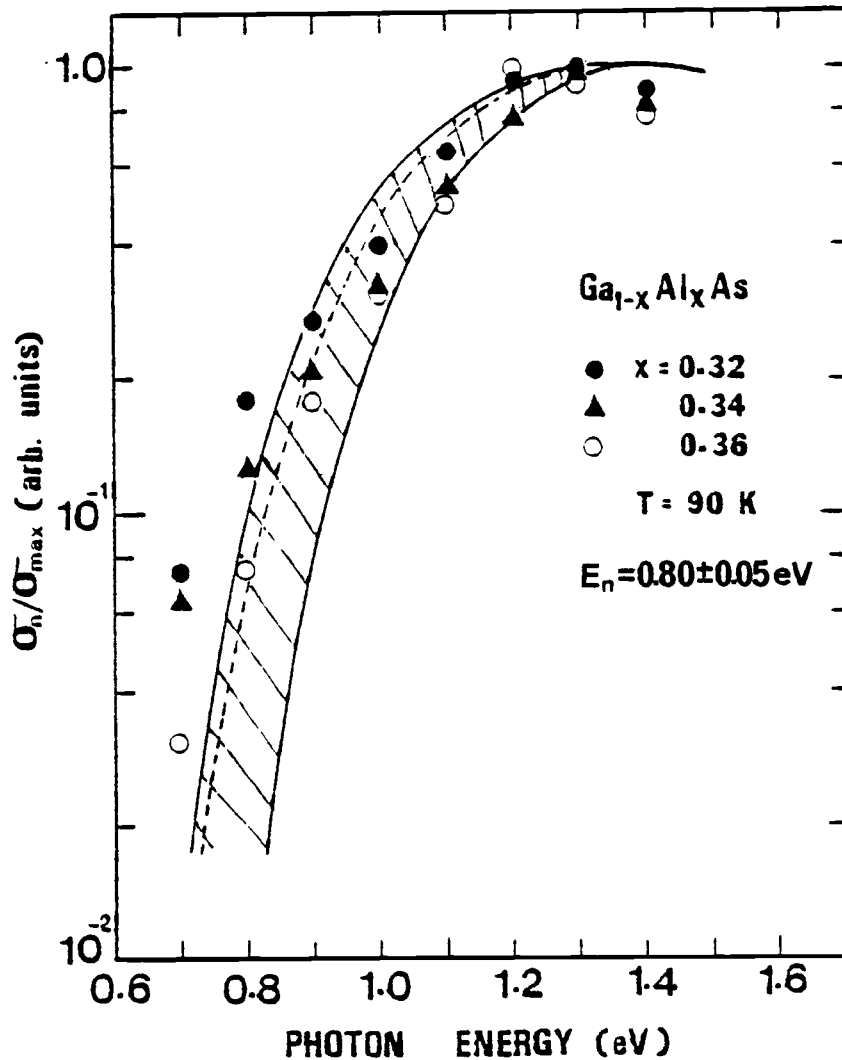


Figure 6.5. Normalized electron photoionization cross section of the defect centers in LPE $\text{Ga}_{1-x}\text{Al}_x\text{As}$. The solid lines and shaded region represent theoretical fits using Lucovsky's model for $x = 0.32$. The dashed line indicates the theoretical lineshape for $x = 0.32$ using $m_T = m^*$ in the model (see text).

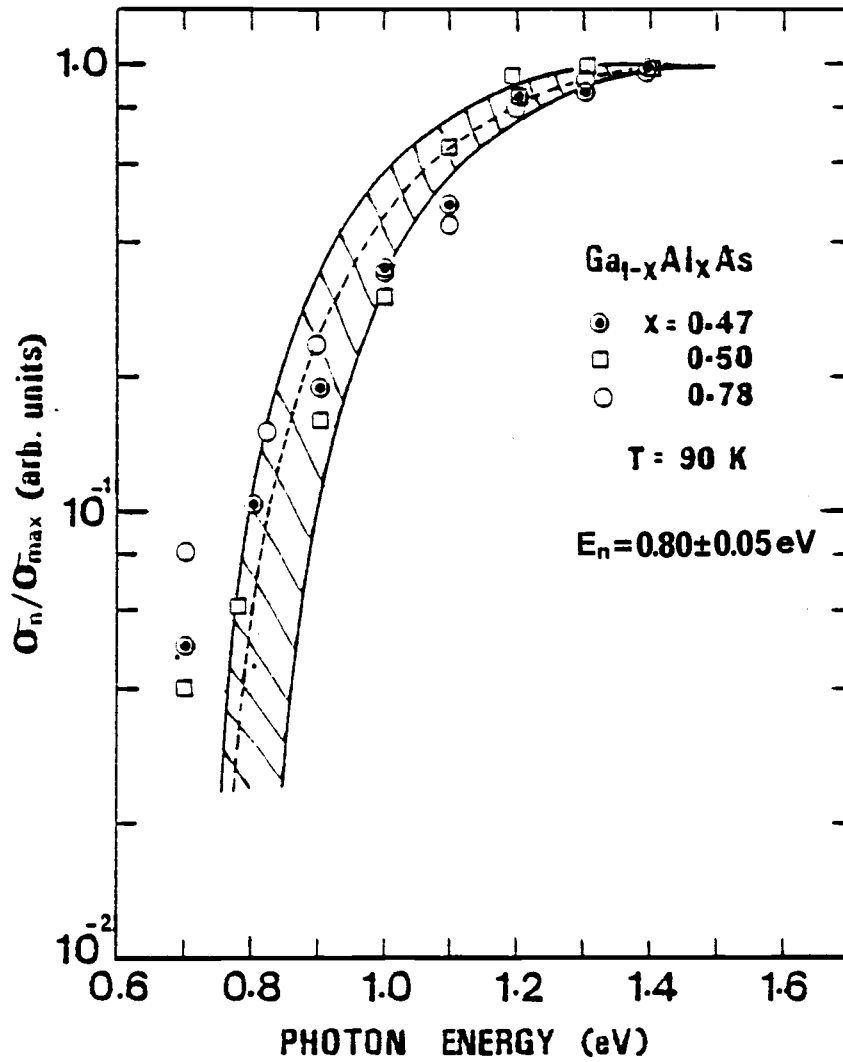


Figure 6.6. Normalized electron photoionization cross section of the defect centers. The solid lines, shaded region, and dashed line for $x = 0.50$ have the same significance as in Figure 6.5.

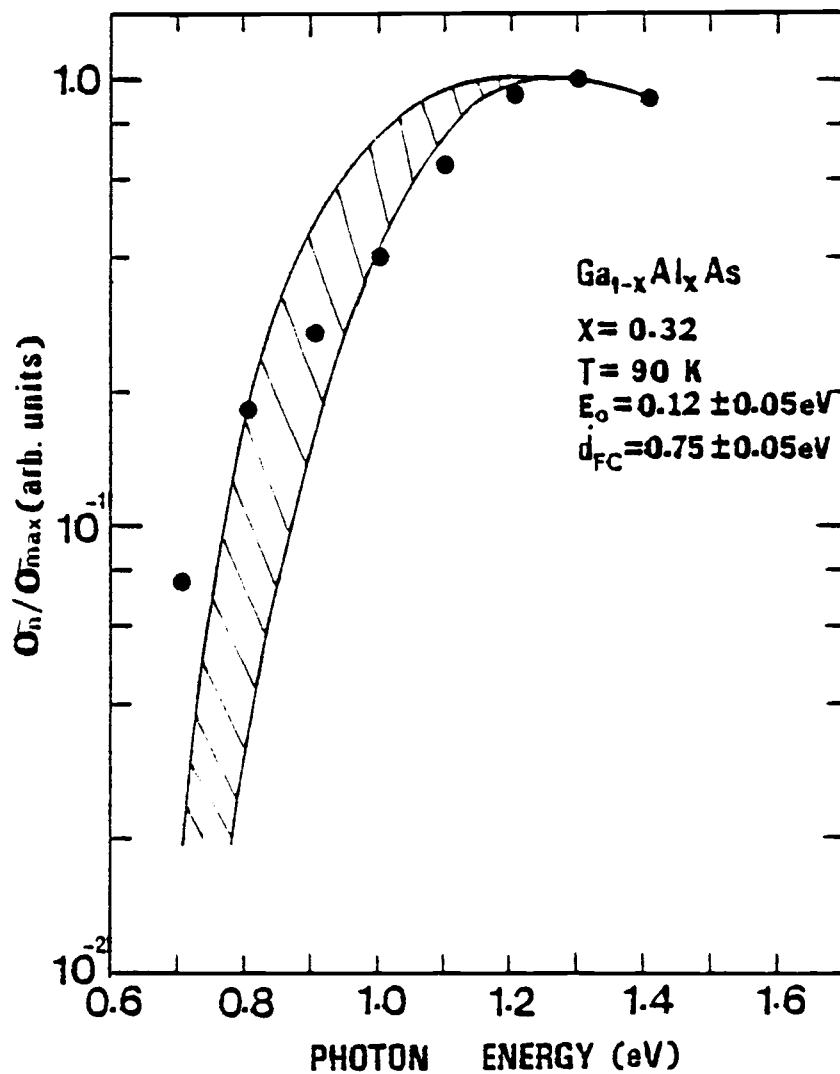


Figure 6.7. Theoretical fit to normalized electron photoionization cross section for $x = 0.32$ using the Huang and Rhys model. The shaded region represents the range of values of the binding energy E_0 and Franck-Condon shift d_{FC} needed to fit the data.

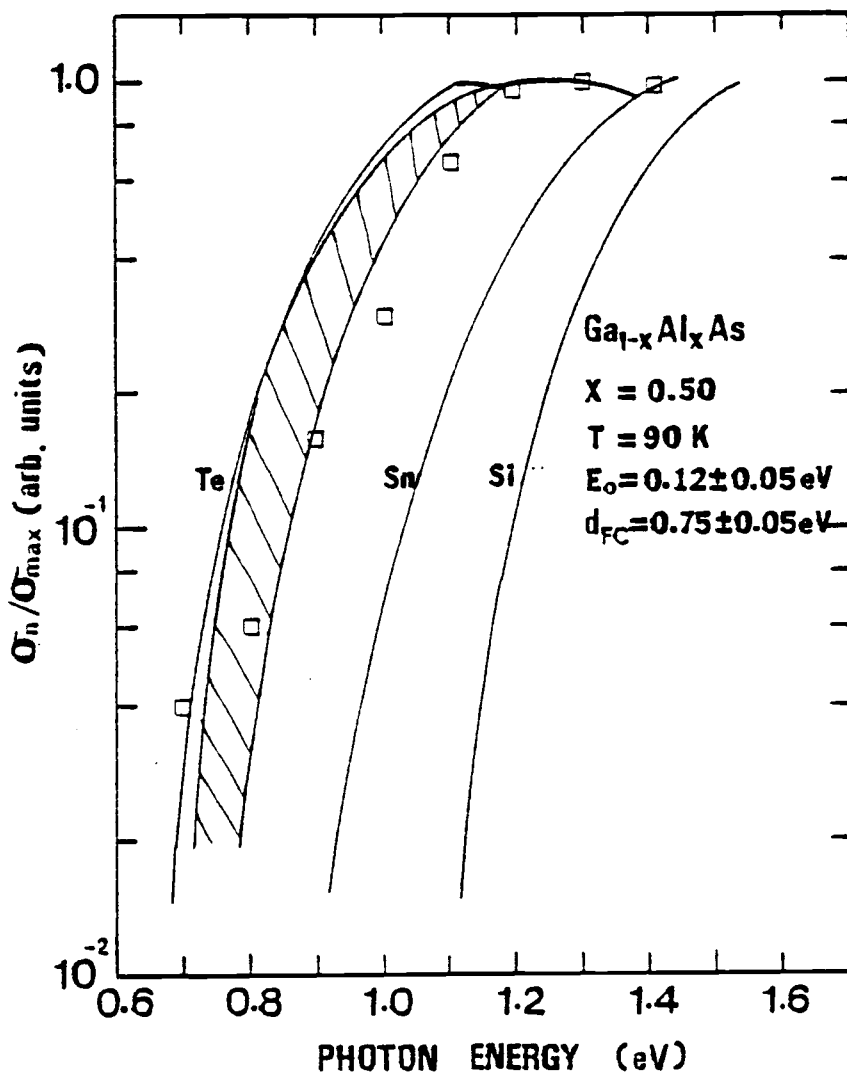


Figure 6.8. Theoretical fit to normalized electron photoionization cross section for $x = 0.50$ using the Huang and Rhys model. The shaded region has the same significance as in Figure 6.7. The optical lineshapes for the defects in intentionally doped samples (Ref. 84) are shown for comparison.

It is assumed that the band gap at 2°K is almost identical to that at 0°K. The defects were assumed to be conduction band-like since it transpires from thermal emission and capture studies⁽⁶⁰⁾ that the level is linked predominantly to the L and X conduction minima. The limitations of using the model of Huang and Rhys for the determination of d_{FC} have been discussed in Chapter II. Also shown for comparison in Figure 6.8 are the optical lineshapes of the defect centers in Se, Te, Si and Sn-doped $Ga_{1-x}Al_xAs$ with $x = 0.40$ ⁽⁸⁴⁾. The values of d_{FC} for intentionally doped crystals obtained by Lang, et al.⁽⁸²⁾ assuming valence band-like states are almost identical to the values obtained in this investigation.

6.4 Discussion

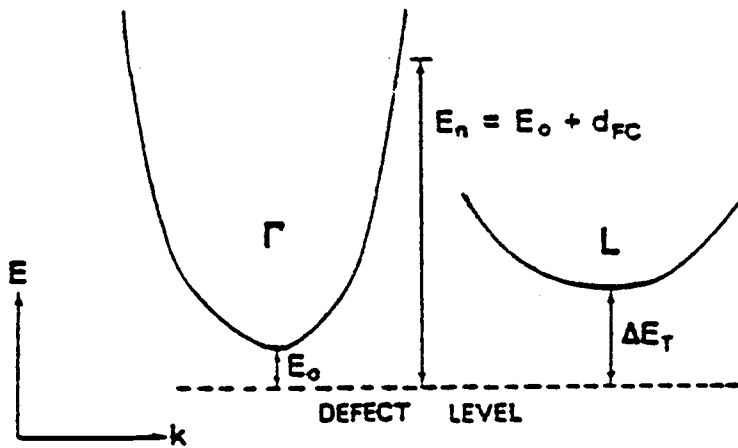
The binding energies of the defect centers in nonintentionally and intentionally doped LPE $Ga_{1-x}Al_xAs$, as shown in Figure 6.2, show an apparent agreement in the direct band gap region. However, since the methods of their determination were quite different, the actual binding energies may disagree to a greater degree. It may only be concluded that the binding energy is related to the dopant specie which is present intentionally or unintentionally.

The agreement between the values of the optical ionization energy $E_n (= E_o + d_{FC})$ derived from the two analytical models is not so good because Lucovsky's model is not suitable for the centers which exhibit an unusually large Stokes shift, i.e., the Franck-Condon energy d_{FC} . From theoretical analysis, the Franck-Condon energy d_{FC} is much larger than the binding energy E_o derived from Hall data and analysis of optical lineshape data. Contrary to the systematic change in the value

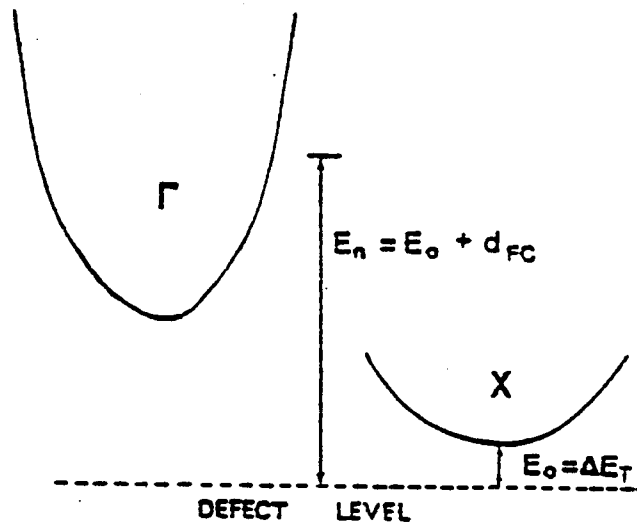
of E_0 and the thermal activation energy ΔE_T (for $x > 0.36$) with change in crystal composition, there is no noticeable change in the value of the optical ionization energy. This can be understood by considering the wavefunction in the defect level to result from several bands and is delocalized in that respect. The value of d_{FC} thus represents a relaxation which is independent of the changing band structure, whereas E_0 signifies the binding energy of the defect with respect to a band minimum. It is imperative at this point to discuss the electron emission and capture mechanisms associated with the defect centers. The profile of the energy ΔE_T as a function of composition in the nonintentionally doped samples is shown in Figure 6.2. For $x > 0.44$ the values of ΔE_T and E_0 are almost identical in the same crystals. Also, since the X minima are the lowest in this composition range, E_0 is the binding energy with respect to these minima. In the direct band gap and band cross-over regions, the two energies are unequal. For $0.25 \leq x \leq 0.36$, it has been shown by Bhattacharya, et al.⁽⁶⁰⁾ that electrons are emitted predominantly to the L minima and capture also occurs via these minima. It was also determined that there is no barrier associated with thermal capture and the thermal activation energy, ΔE_T , is equal to the sum of the trap "depth" and the intervalley separation, ΔE_{TL} . In the indirect band gap region the X minima are mainly involved and it is believed that in the band cross-over region, both are involved in varying degrees.

In the Hall and photo-Hall measurements, an increase of mobility upon photoexcitation signifies decreased ionized impurity scattering and hence the involvement of an acceptor-like center. The identical persistent photoconductivity effect observed during thermally stimulated capacitance and Hall measurements establishes beyond doubt that

the same defect is involved. Acceptor-like defects exhibiting similar persistent photoconductivity have been detected in other III-V^(85,86) and II-VI⁽⁸⁷⁾ semiconducting compounds too. Thus the significant result which emerges from the present study is that the defect centers in the nonintentionally doped crystals are acceptor-like in contrast to the donor-like nature of the defects in the intentionally doped crystals. Since no thermal barrier has been associated with electron capture by the centers in these crystals, it is conceivable that the low thermal capture cross sections are due to their acceptor-like nature. On the other hand, the large relaxation energy is related to the observed persistent photoconductivity. Consequently, the defect centers in the nonintentionally doped crystals may be described thus: they are primarily responsible for the electrons in the conduction band, interacting mainly with the indirect minima during thermal emission and capture processes, and are acceptor-like. They are also characterized by a large Stokes shift. Models which will perhaps account for the observed trends are presented in Figures 6.9 and 6.10. The emission-capture in the direct and indirect band gap regions are separately shown in Figure 6.9. The total system energy of the defect in its ground and excited states are depicted in Figure 6.10, which is the configuration coordinate diagram in the large lattice relaxation limit. The thermal barrier to electron capture, as found experimentally, is taken to be zero. Also, for the direct band gap region, the system energy in the L conduction minima is introduced to account for the interaction of the defects with these minima.



(a) DIRECT BANDGAP



(b) INDIRECT BANDGAP

Figure 6.9. Models to explain the measured binding energy, E_0 , the thermal activation energy, ΔE_T , and the optical ionization energy, E_n , of the defects in (a) direct band gap, and (b) band gap nonintentionally doped LPE $\text{Ga}_{1-x}\text{Al}_x$.

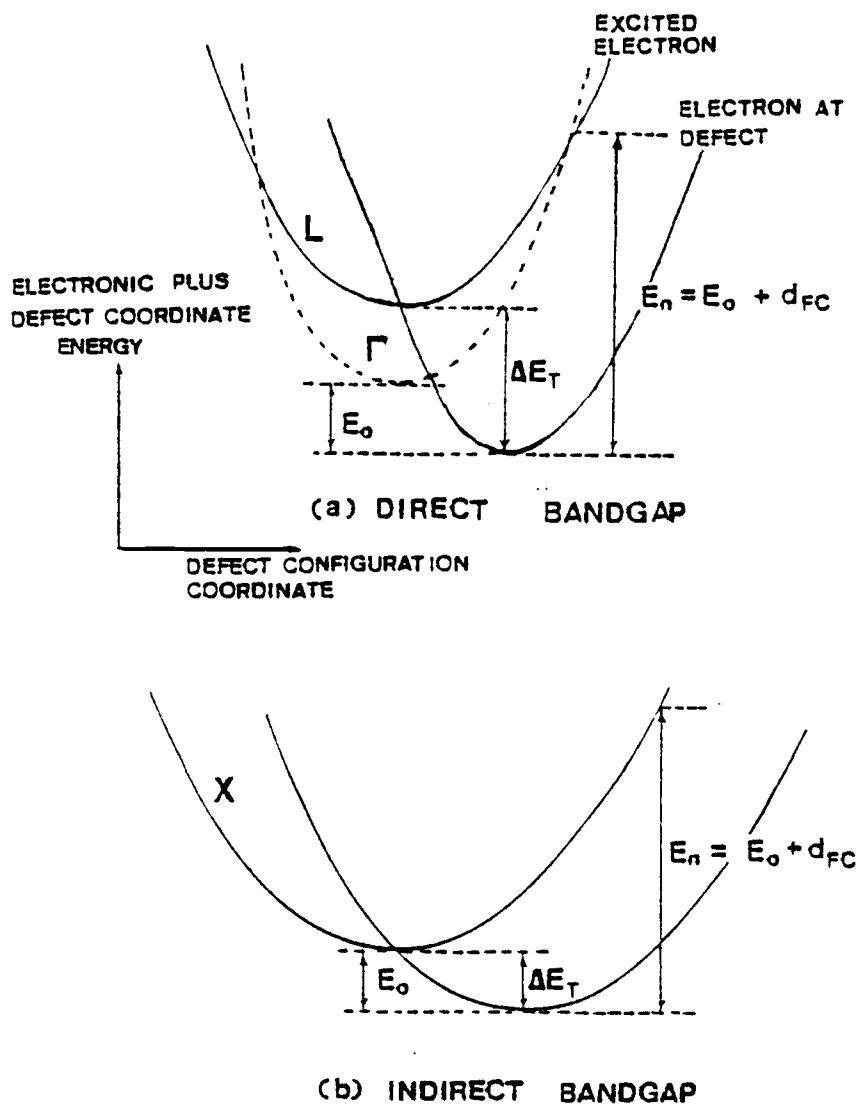


Figure 6.10. Configuration coordinate diagrams for the defects in (a) direct band gap, and (b) indirect band gap nonintentionally doped LPE $\text{Ga}_{1-x}\text{Al}_x\text{As}$.

6.5 Physico-Chemical Origin of the Defects

For the defects in Te-doped LPE $\text{Ga}_{1-x}\text{Al}_x\text{As}$, Lang, et al.⁽⁸²⁾ proposed a model in which the microstructure of the defect is a complex involving Te as a donor and an arsenic vacancy, V_{As} . The same model was extended for the defects identified in LPE crystals doped with other donor impurities, e.g., Se, Si and Sn. These authors have also given reasons as to why possibilities such as substitutional impurities, cation-vacancy complexes and interstitials can be ruled out. Therefore, it is conceivable that an impurity-vacancy complex would explain the results obtained in this study from the nonintentionally doped crystals. It is obvious that the electrical and optical properties of the defects in these nonintentionally doped crystals are very similar to those of the centers in the doped crystals. This fact and their consistent presence in crystals of all compositions greater than $x = 0.25$ point toward a vacancy-related defect. If the center is related to a gallium vacancy, its concentration would strongly depend on composition. This is, however, not the case. Moreover, the gallium vacancy and its complexes in GaAs⁽⁸⁸⁾ are known to produce luminescence bands. But it has been established by Bhattacharya, et al.⁽³²⁾ that the defects under study are nonradiative. Thus the involvement of an arsenic vacancy in the formation of the center is more possible. The vacancy determines the major properties of the center and it is believed that more detailed differences, such as binding energy, charge state, etc., are caused by the chemical impurity. All the impurities which have been considered give rise to donor-like characteristics. Elements which have not been used as dopants are C and S. C is an impurity which can be consistently present in the crystals, since the LPE boats

are made of graphite. C in GaAs also acts as an acceptor⁽⁸⁹⁾ and the properties of C-doped $\text{Ga}_{1-x}\text{Al}_x\text{As}$ have not been reported. Thus, a C-V_{As} model is proposed to explain the characteristics of the defect centers in these nonintentionally doped crystals. They may not necessarily be the same centers identified in Si, Se, Sn and Te-doped $\text{Ga}_{1-x}\text{Al}_x\text{As}$. Some of the characteristics of this class of nonradiative defects in $\text{Ga}_{1-x}\text{Al}_x\text{As}$, i.e., large relaxation and their localized resonant nature, give rise to their unique thermal and optical properties. Such defects may play a pronounced role in the performance of optoelectronic devices.

CHAPTER VII

CONCLUSIONS

The purpose of this work was to investigate the electrical and optical properties of two technologically important semiconducting compounds. Both $\text{In}_{1-x}\text{Ga}_x\text{As}_y\text{P}_{1-y}$ and $\text{Ga}_{1-x}\text{Al}_x\text{As}$ are now being widely used to fabricate heterostructure optoelectronic and microwave devices. Electrical and optical measurement techniques were used to determine parameters which define the bulk properties of the compounds and defect states therein.

Electron and hole traps were detected in the $\text{In}_{1-x}\text{Ga}_x\text{As}_y\text{P}_{1-y}$ quaternary compounds by capacitance spectroscopic techniques. This is one of the first identifications of traps in these compounds since such measurements are made difficult due to the low barrier heights of the Schottky diodes. The thermal activation energy, density and thermal capture cross section of the trapping centers have been calculated. The significant result obtained is that electron traps with an activation energy of 0.82 eV, which have identical properties to a dominant center in bulk and VPE GaAs, are present in some quaternary layers. Measurements have been performed on organometallic VPE GaAs crystals with progressively differing As/Ga ratios to study the physico-chemical origin of these common deep centers. A linear dependence of the trap concentration on As/Ga ratio in the material indicates the involvement of a Ga vacancy in the formation of the center.

Low field transport measurements over the temperature range 20-600°K have been made on the same quaternary samples using the van der Pauw technique. Detailed analysis of the mobility data has yielded the

concentration of ionized impurities, the alloy scattering potentials, ΔU , and other important transport parameters. It is found that alloy scattering plays a dominant role in limiting carrier mobilities in these alloys and the maximum value of $\Delta U \approx 0.8$ eV occurs in crystals with band gap $E_g \approx 0.95$ eV. The variation of ΔU with composition consistently explains the mobility variation in the alloys as a function of composition. Photo-Hall measurements at low temperatures reveal the presence of donor- and acceptor-like defects in the LPE and VPE quaternary alloys, respectively. These centers exhibit persistent photoconductivity at low temperatures and have a high barrier energy (~ 0.2 eV) associated with electron capture. The anomalous variation of mobility and carrier concentration at $T > 350^\circ\text{K}$ in alloys with $E_g \sim 0.95$ eV have been explained by assuming large clusters of localized defects.

In the LPE $\text{Ga}_{1-x}\text{Al}_x\text{As}$ crystals, attention was focused on dominant defect centers which are suspected to be responsible for degradations in heterostructure lasers. Hall-effect, thermally stimulated capacitance and optical lineshape measurements were performed to understand the properties and origin of these defects. Photo-Hall measurements indicate that the defects are acceptor-like. This is in contrast to the donor-like properties of similar defects exhibited in intentionally doped crystals. Photoionization cross section and optical lineshape data have been analyzed by both Lucovsky's model and the Huang and Rhys phonon-broadened theory. The best fits to the experimental data are obtained for an optical ionization energy $E_n = 0.87 \pm 0.10$ eV and a Franck-Condon shift $d_{\text{FC}} = 0.75 \pm 0.05$ eV. There is no apparent dependence of the value of this parameter on the alloy compositions. The strong persistent photoconductivity of this defect center is attributed to

large lattice relaxation. A model for the defects in the nonintentionally doped crystals has been proposed in which the defect is a complex involving an impurity--possibly C-- and V_{As} . Comparison with the models used to explain the properties of similar defects in intentionally doped crystals leads to a more general microstructure in which this class of complex defects in the ternary alloys can be viewed as being formed of V_{As} , which defines the general properties, and a substitutional impurity in the Ga or As sublattice, which determines the small differences in binding energy, thermal activation energy and charge state.

A few concluding remarks can be made regarding suggestions for future work whereby a fuller understanding of the material properties of the ternary and quaternary alloys can be gained. In particular, it is felt that some fundamental parameters related to the quaternaries need to be determined experimentally. The band structure of the quaternary alloys as a function of composition has not been measured. Only theoretical estimates of the intervalley separation from Monte Carlo calculations are available. Such calculations shown that indirect conduction minima, L or X, are located 0.7 - 0.8 eV above the direct Γ minimum. It is known that the application of hydrostatic pressure moves the energy position of the band minima and alter the intervalley separation. Low and high field transport measurements performed on the crystals would give information regarding the intervalley separations, intervalley scattering parameters, coupling constants between the valleys and the effective masses in the indirect minima. More work is also necessary to understand the origin of various defects detected in this study. Crystals with very high purity and also doped intentionally have

to be grown and a systematic study undertaken.

A plausible model for the microstructure of the dominant defect in LPE $\text{Ga}_{1-x}\text{Al}_x\text{As}$ has been suggested. Since C has been included in the formation of the complex defect, it would be of interest to study the properties of crystals intentionally doped with C and compare them with the properties of crystals grown in a boron nitride boat. The latter category of crystals would not be intentionally doped with C since this element is suspected to migrate into the crystal from the graphite boat during liquid phase epitaxial growth.

REFERENCES

1. H.M. Macksey, T.G. Blocker, F.H. Doerbeck, *Electron. Lett.*, 13, 312 (1977).
2. J.B. Gunn, *IEEE Trans. Electron Devices*, ED-23, 705 (1976).
3. R.N. Hall, G.E. Fenner, J.D. Kingsley, T.J. Soltys, and R.O. Carlson, *Phys. Rev. Lett.*, 9, 366 (1962).
4. N. Holonyak, Jr. and S.F. Bevacqua, *Appl. Phys. Lett.*, 1, 82 (1962).
5. L.W. James and R.L. Moon, *Appl. Phys. Lett.*, 26, 467 (1975).
6. R.D. Dupuis and P.D. Dapkus, *Appl. Phys. Lett.*, 31, 466 (1977).
7. A.Y. Cho and J.R. Arthur, Jr. in Progress in Solid State Chemistry, 10, 157, Pergamon Press, NY (1975).
8. J.B. Mullin, R.J. Heritage, C.H. Holliday, and B.W. Straughan, *J. Crystal Growth*, 3, 281 (1968).
9. H.C. Casey, Jr. and M.B. Panish, Heterostructure Lasers, Academic Press, New York (1978).
10. H. Kressel and J.K. Butler, Semiconductor Lasers and Heterojunction LED's, Academic Press, New York (1978).
11. C.M. Wolfe and G.E. Stillman, "Proc. 3rd Int. Symp. GaAs," pp. 3-17, Inst. Physics, London (1971).
12. Osanai, T. Shioda, T. Moriyama, and S. Araki, *Electron Lett.*, 12, 549 (1976).
M. Horiguchi and H. Osanai, *Electron Lett.*, 12, 310 (1976).
13. D.N. Payne and W.A. Gambling, *Electron Lett.*, 11, (1975).
14. R.D. Burnham, N. Holonyak, Jr. and D.R. Scitres, *Appl. Phys. Lett.*, 17, 455 (1970).
15. M.A. Littlejohn, J.R. Hauser, and T.H. Glisson, *Appl. Phys. Lett.*, 30, 242 (1977).

16. R.E. Nahory, M.A. Pollack, W.D. Johnston, and R.L. Barns, Appl. Phys. Lett., 33, 659 (1978).
17. R.J. Nicholas, J.C. Portal, C. Houlbert, P. Perrier, and T.P. Pearsall, Appl. Phys. Lett., 34, 492 (1979).
18. H. Brendecke, H.L. Störmer, and R.J. Nelson, Appl. Phys. Lett., 35, 772 (1979).
19. R.H. Leheny, A.A. Ballman, J.C. DeWinter, R.E. Nahory, and M.A. Pollack, presented at the 21st Electron. Mater. Conf., Boulder, CO, 1979.
20. P.D. Greene, S.A. Wheeler, A.R. Adams, A.N. El-Sabbahy, and C.N. Ahmed, Appl. Phys. Lett., 35, 78 (1979).
21. M.A. Littlejohn, J.R. Hauser, T.H. Glisson, D.K. Ferry, and J.W. Harrison, Solid State Electron., 21, 107 (1978).
22. M.A. Littlejohn, R.A. Sadler, T.H. Glisson, and J.R. Hauser, Proc. 7th Int. Symp. on GaAs and Related Compounds, St. Louis, MO, 239 (1979).
23. R. Yeats and S.H. Chiao, presented at the 37th Ann. Device Res. Conf., Boulder, CO (1979).
24. G.H.B. Thomson and G.D. Henshall, Electron. Lett., 16, 42 (1980).
25. J. van der Pauw, Philips Res. Rep., 13, 1 (1958).
26. P.K. Bhattacharya and M.D. Yeaman, Solid State Electron. 24, 297 (1981).
27. A. Majerfeld and P.K. Bhattacharya, Appl. Phys. Lett., 33, 259 (1978).
28. P.K. Bhattacharya, J.W. Ku, S.J.T. Owen, V. Aebi, C.B. Cooper, and R.L. Moon, Appl. Phys. Lett., 36, 304 (1980).

29. E.E. Wagner, D.E. Mars, G. Ham, and G.B. Stringfellow, *J. Appl. Phys.*, 51, 5434 (1980).
30. H. Morkoc, A.Y. Cho, and C. Radice, *J. Appl. Phys.*, 51, 4882 (1980).
31. P.M. Petroff, D.V. Lang, R.A. Logan and W.D. Johnston, in Proc. of the International Conference on Defects and Radiation Effects in Semiconductors, Nice, Inst. of Phys., London, 427 (1979).
32. P.K. Bhattacharya, S.J.T. Owen, and J. Marrs, *Appl. Phys. Lett.*, 36, 664 (1980).
33. M. Lax, *Phys. Chem. Solids*, 8 (1959).
34. P.T. Landsberg and A.R. Beattie, *Phys. Chem. Solids*, 8 (1959).
35. R.N. Hall, *Phys. Rev.*, 87, 387 (1952).
36. W. Shockley and W.T. Read, *Phys. Rev.*, 87, 835 (1952).
37. D.V. Lang and C.H. Henry, *Phys. Rev. Lett.*, 35, 1525 (1975).
38. M. Bleicher and E. Lange, *Solid-State Electronics*, 16, 373 (1973).
39. P.K. Bhattacharya, Ph.D. Thesis, Sheffield University (1978).
40. A. Mitonneau, G.M. Martin and A. Mircea, *Inst. Phys. Conf. Ser.* 33a, Ch. 2 (1977).
41. G. Lucovsky, *Solid State Communciations*, 3, 229 (1965).
42. H.G. Grimmeiss and L-Å Ledebø, *J. Phys. C: Solid State Phys.*, 8 (1975).
43. K. Huang and R. Rhys, *Proc. R. Soc.*, 204, 406 (1950).
44. M. Jaros, *Phys. Rev.*, B16, 3694 (1977).
45. R.A. Smith, Semiconductors, Cambridge at the University Press (1959).
46. A.C. Beer, Solid State Physics, edited by F. Seitz and D. Turnbull, (New York:Academic), 4 (1963).
47. M.B. Panish, *J. Appl. Phys.*, 44, 2667 (1973).
48. D.V. Lang, *J. Appl. Phys.*, 45, 3023 (1974).

49. A.M. White, B. Day and A.J. Grant, *J. Phys.*, C12, 4833 (1979).
50. C.T. Sah and J.W. Walker, *Appl. Phys. Lett.*, 22, 384 (1973).
51. F.E. Roberts, *Phys. Lett.*, 17, 21 (1965).
52. M.C. Hales and J.R. Knight, *J. Phys. E:Sci. Instrum.*, 6, 520 (1973).
53. J.A. Van Vechten and C.D. Thurmond, *Phys. Rev.*, B14, 3539 (1976).
54. A. Mircea, A. Mitonneau, J. Hallais, and M. Jaros, *Phys. Rev.*, B16, 3665 (1977).
55. O. Wada, A. Majerfeld, and A.N.M.M. Choudhury, *J. Appl. Phys.*, 51, 423 (1980).
56. J. Leotin, R. Barbaste, S. Askenazy, M.S. Skolnick, R.A. Stradling, and J. Tuchendler, *Solid-State Commun.*, 15, 693 (1974).
57. C.H. Henry and D.V. Lang, *Phys. Rev.*, B15, 989 (1977) ✕
58. A. Mircea, A. Mitonneau, and J. Vannimenus, *J. Phys. (Paris)*, 38, L41 (1977).
59. D. Bois, A. Chantre, G. Vincent, and A. Nouailhat, Proc. Int. Conf. on Physics of Semiconductors, Edinburgh (UK), 295 (1979).
60. P.K. Bhattacharya, A. Majerfeld and A.K. Saxena, in Proc. of the 7th Int. Symp. on GaAs and Related Compounds, St. Louis, edited by C.M. Wolfe, *Inst. of Phys.*, London, 199 (1979).
61. J. Chavallier, *Status Solidi (b)*, 14, 531 (1972).
62. A.M. White, A.J. Grant, and B. Day, *Electron. Lett.*, 14, 409 (1978).
63. P.K. Bhattacharya, J.W. Ku, S.J.T. Owen, S.H. Chiao, and R. Yeats, *Electron. Lett.*, 15, 753 (1979).
64. Y. Sasai, Y. Yamazoe, M. Okuyama, T. Nishino, and Y. Hamakawa, *Japan J. Appl. Phys.*, 18, 1415 (1979).
65. S.H. Chiao and R.L. Moon, in Progress in Crystal Growth, London: Pergamon, (1980).

66. L. Nordheim, *Annalen der Physik*, 607 (1931).
67. C. Hilsum, H.D. Rees, and W. Wilgoss, *Phys. Status Solidi (b)*, 56, K93 (1973).
68. G.B. Stringfellow and H. Künzel, *J. Appl. Phys.* 57, 3254 (1980).
69. P. Blood, *Phys. Rev.*, B6, 2257 (1972).
70. L.W. Aukerman and R.K. Willardson, *Appl. Phys. Lett.*, 31, 939 (1962).
71. R.F. Leheny, R.E. Nahory, M.A. Pollack, A.A. Bullman, E.D. Beebe, J.C. DeWinter, and R.J. Martin, *IEEE Electron. Dev. Lett.*, EDL-1, 110 (1980).
72. J.H. Marsh, P.A. Houston, P.N. Robson, in Proc. 8th Int. Symp. on GaAs and Related Compounds, Vienna, Austria (1981).
73. A.K. Saxena, *Phys. Stat. Sol. (b)*, 96, K77 (1979).
74. A.J. SpringThorpe, F.D. King and A. Becke, *J. Electron. Mater.*, 4, 101 (1975).
75. R.J. Nelson, *Appl. Phys. Lett.*, 31, 351 (1977).
76. A.K. Saxena, *Appl. Phys. Lett.*, 36, 79 (1980).
77. K. Kaneko, M. Ayabe, and N. Watanabe, Proc. of the 6th Int. Symp. on GaAs and Related Compounds, Edinburgh Conference, (Inst. of Phys., London), 216 (1977).
78. B. Balland, G. Vincent, D. Bois, and P. Hirtz, *Appl. Phys. Lett.*, 34, 108 (1979).
79. R. Dingle, R.A. Logan, and J.R. Arthur, Proc. of the 6th Int. Symp. on GaAs and Related Compounds, Edinburgh Conference, edited by C. Hilsum, *Inst. of Phys.*, London, 66 (1977).
80. D.V. Lang and R.A. Logan, *Phys. Rev. Lett.*, 39, 635 (1977).
81. A.K. Saxena, Ph.D. Thesis, University of Sheffield, (1978) (unpublished).

82. D.V. Lang, R.A. Logan and M. Jaros, Phys. Rev., B19, 1015 (1979).
83. D.E. Aspnes, Phys. Rev., B15, (1976).
84. D.V. Lang and R.A. Logan, in Proc. of the 14th Int. Conf. on the Physics of Semiconductors, Edinburgh, edited by Wilson, Institute of Physics, London, 433 (1979).
85. M.G. Craford, G.E. Stillman, J.A. Rossi, and N. Holonyak, Jr., Phys. Rev., 168, 867 (1968).
86. P.K. Bhattacharya, J.W. Ku, S.J.T. Owen, G.H. Olsen, and S.-H. Chiao, IEEE J. Quantum Electronics, QE-17, 150 (1981).
87. M.R. Lorenz, B. Segall, and H.H. Woodbury, Phys. Rev., 134, A751 (1964).
88. E.W. Williams and H.B. Bebb, in Semiconductors and Semimetals, edited by R.K. Willardson and A.C. Beer, Academic Press, 8, 321 (1972).
89. D.J. Ashen, P.J. Dean, D.T.J. Hurle, J.A.B. Mullin, A.M. White and P.D. Greene, J. Phys. Chem. Solids, 36, 1041 (1975).
90. B.R. Nag, Theory of Electrical Transport in Semiconductors, Pergamon Press (1972).
91. H. Brooks, Advan. Electron. Electron Phys., 7, 158 (1955).
92. A. Fortini, J. Appl. Phys., 41, 3121 (1970).
93. J.R. Hauser, M.A. Littlejohn and T.H. Glisson, Appl. Phys. Lett., 28, 458 (1976).
94. R.L. Moon, G.A. Antypass, and L.W. James, J. Electron. Mater., 3, 635 (1974).
95. C.M. Wolfe, G.E. Sillman, and W.T. Lindley, J. Appl. Phys., 41, 3088 (1970).

96. J.D. Zook, Phys. Rev., 136, A869 (1964).
97. L.R. Weisberg, J. Appl. Phys., 33, 1817 (1962).
98. D.E. Aspnes, Phys. Rev., B14, 5331 (1976).

APPENDICES

APPENDIX A

MOBILITIES OF DIFFERENT SCATTERING MECHANISMS

Carrier transport in a solid is governed by the Boltzmann transport equation

$$\frac{df}{dt} = \left(\frac{\partial f}{\partial t}\right)_{\text{local}} + \nabla_r f + \nabla_p f + \left(\frac{\partial f}{\partial t}\right)_{\text{coll.}} \quad (\text{A1})$$

Consider a homogeneous material in a steady state condition,

$$\nabla_p f = -\left(\frac{\partial f}{\partial t}\right)_{\text{coll.}} \approx -\frac{f-f_0}{\tau} \quad (\text{A2})$$

where f_0 is the carrier distribution in the equilibrium condition and τ is the relaxation time.

Left side of Eqn. (A2) may be written in terms of wave vector form as

$$\frac{\partial f}{\partial t} \Big|_{\text{coll.}} = -\frac{V}{(2\pi)^3} \int [P(K,K')f(K) - P(K',K)f(K')] dK' \quad (\text{A3})$$

$P(K,K')$ and $P(K',K)$ denote respectively the probability of transition from K to K' and from K' to K states, and V is the volume of crystal. Expanding f in spherical harmonics with the direction of the field as the polar axis, it becomes

$$f(K) \approx f_0 + K f_1 \cos\theta \quad (\text{A4})$$

where θ is the angle between the electron wave vector and the field direction. Using condition that for the equilibrium distribution f_0 ,

$$P(K',K)f_0(K') = P(K,K')f_0(K) \quad (A5)$$

Eqn. (A3) becomes

$$\frac{\partial f}{\partial t} \Big|_{\text{coll.}} = \frac{V}{(2\pi)^3} \int \left[\frac{f_0(K)}{f_0(K')} f_1(K') K' \cos \theta' - f_1(K) K \cos \theta \right] P(K,K') dK' \quad (A6)$$

Consider the elastic collisions, the energy of the electron remains unchanged,

$$f_0(K) = f_0(K') \quad (A7)$$

and

$$\frac{\partial f}{\partial t} \Big|_{\text{coll.}} = \frac{-f - f_0}{\tau} = - \frac{VKf_1 \cos \theta}{(2\pi)^3} \int \left(1 - \frac{K' \cos \theta'}{K \cos \theta} \right) P(K,K') dK' \quad (A8)$$

Thus,

$$\frac{1}{\tau} = \frac{V}{(2\pi)^3} \int \left(1 - \frac{K' \cos \theta'}{K \cos \theta} \right) P(K,K') dK' \quad (A9)$$

In order to calculate the carrier relaxation time, the carrier transition probability should be figured out first. Consider an electron of energy E_i and a small perturbation potential ΔV in the vicinity of the scattering center, the eigen function which describes the electron is

$$\psi(t) = \sum_n C_n(t) \psi_n \exp\left[-\left(\frac{i}{\hbar}\right)E_n t\right] \quad (A10a)$$

where

$$C_n(t) = 1 + \frac{1}{i\hbar} \int_0^t (\psi_n^*, \Delta V \psi_i) dt \quad n = i \quad (A10b)$$

$$C_n(t) = \frac{1}{i\hbar} \int_0^t (\psi_n^*, \Delta V \psi_i) \exp\left[\frac{i}{\hbar}(E_n - E_i)t\right] \quad n \neq i \quad (\text{A10c})$$

The probability of an electron scattered from an initial state $E_1(K)$ to a final state $E_2(K')$ at any time t after the perturbing potential $(\Delta V/e)$ is applied is

$$P(K, K') \equiv \frac{\partial}{\partial t} \left| C_{K'}(t) \right|^2 = \frac{2\pi}{\hbar} (\psi_2^*, \Delta V \psi_1)^2 \Omega(E_1 - E_2) \quad (\text{A11})$$

where $(\psi_2^*, \Delta V \psi_1)^2 \equiv M(K, K')$ is the transition matrix, and $\Omega(E_1 - E_2) = (\sin(E_1 - E_2)t/\hbar)/\pi(E_1 - E_2)$.

In what follows, the mathematical forms of mobilities limited by ionized impurity, polar optical phonon and alloy scattering have been derived. The expression for the mobilities limited by space charge scattering, deformation potential and piezoelectric scattering have also been outlined.

(I) Ionized Impurity Scattering

Assuming $\sigma(\theta, \phi)$ is the scattering cross section of an ionized impurity center, the velocity of the incident electron is given by $(1/\hbar)\partial E/\partial K$ and N_I is the ionized impurity concentration, then the total intensity of the scattered wave in a solid angle $\sin\theta d\theta d\phi$ will be given by

$$S_{K-K'} = \frac{N_I}{\hbar} \frac{\partial E}{\partial K} \sigma(\theta, \phi) \sin\theta d\theta d\phi \quad (\text{A12})$$

Equating this with the number of transitions obtained by using the transition probability,

$$\begin{aligned}
T_{K \rightarrow K'} &\equiv \frac{V}{(2\pi)^3} N_I V \int_{\phi=0}^{2\pi} \int_{\theta=0}^{\pi} \int_{K'=0}^{\infty} P(K, K') dK' \\
&= \frac{N_I}{\hbar} \int_{\phi=0}^{2\pi} \int_{\theta=0}^{\pi} \frac{\partial E}{\partial K} \sigma(\theta, \phi) \sin\theta d\theta d\phi
\end{aligned} \tag{A13}$$

Substitute Eqn. (A11) into (A13) and change the variable K' to E_2 and integrate over E_2 , Eqn. (A13) becomes

$$T_{K \rightarrow K'} = \frac{N_I V^2}{(2\pi)^3} \frac{2\pi}{\hbar^3} m_c K \int_{\phi=0}^{2\pi} \int_{\theta=0}^{\pi} |M(K, K')|^2 \sin\theta d\theta d\phi \tag{A14}$$

Comparing Eqn. (A13) with Eqn. (A14) we obtain

$$\sigma(\theta, \phi) = \frac{V^2 m_c^2}{4\pi^2 \hbar^2} |M(K, K')|^2 \tag{A15}$$

By using Eqn. (A9), the carrier relaxation time due to ionized impurity scattering is given by

$$\frac{1}{\tau_I} = \frac{N_I}{\hbar} \frac{\partial E}{\partial K} \int_{\phi=0}^{2\pi} \int_{\theta=0}^{\pi} \sigma(\theta, \phi) \left(1 - \frac{K' \cos\theta'}{K \cos\theta}\right) d\theta d\phi \tag{A16}$$

It should be mentioned that θ' and θ represent the angle between K' , K and the direction of the field, respectively, and θ_K is the angle between K and K' , then

$$\cos\theta' = \cos\theta \cos\theta_K + \sin\theta \sin\theta_K \cos\phi \tag{A17}$$

where ϕ is measured with reference to the plane containing the field and K . Since $\sigma(\theta, \phi)$ is independent of ϕ , Eqn. (A16) can be integrated over ϕ and becomes

$$\frac{1}{\tau_I} = \frac{2\pi N_I}{h} \frac{\partial E}{\partial K} \int_0^\pi \sigma(\theta_K) (1 - \cos\theta_K) \sin\theta_K d\theta_K \quad (\text{A18})$$

In the derivation of $\sigma(\theta)$, it is more accurate to use screened Coulomb potential approximation method. The potential energy of an electron in this vicinity of an impurity center can be approximated as

$$V(r) = - \frac{Ze^2}{4\pi\epsilon_r} \exp(-r/L_D) \quad (\text{A19})$$

where Z is the charge number of the ionized impurity, r is the distance from scattering center. L_D is the Debye length as defined in Eqn. (2.16b). Eqn. (A19) can be solved from Poisson's equation by assuming Boltzmann statistics. The transition matrix will be given by

$$\begin{aligned} M(K, K') &= \int \psi_K V(r) \psi_{K'}^* dr \\ &= - \int U_K \exp(iK \cdot r) \frac{Ze^2 \exp(-r/L_D)}{4\pi\epsilon_s r} U_{K'} \exp(-iK' \cdot r) dr \end{aligned} \quad (\text{A20})$$

Approximately the electron waves by plane waves and expanding the potential function in a Fourier series we obtain⁽⁹⁰⁾

$$|M(K, K')| = \frac{Ze^2}{V\epsilon_s (|K-K'|^2 + L_D^{-2})} \quad (\text{A21})$$

since $K=K'$ (vector form)

$$\text{then } |K-K'| = 2K \sin \frac{\theta_K}{2}$$

Substituting this relation into Eqn. (A15), the scattering cross section is

$$\sigma(\theta, \phi) = \left[\frac{2m_c z e^2}{4\pi\epsilon_s \hbar^2 (4K^2 \sin^2 \theta_K / 2 + L_D^{-2})} \right]^2 \quad (\text{A22})$$

By using the relations $E = \hbar^2 k^2 / 2m_c$ and $b = 4K^2 L_D^2$, and substitute Eqn. (A22) for (A18), then the relaxation time is given by

$$\frac{1}{\tau_I} = \frac{2\pi N_I \hbar K}{m_c} \int_0^\pi \frac{2Ze^2 m_c}{4\pi\epsilon_s \hbar^2} \frac{(1 - \cos \theta_K) \sin \theta_K}{(4K^2 \sin^2 \theta_K / 2 + L_D^{-2})^2} d\theta_K \quad (\text{A23})$$

After further simplification, (A23) becomes

$$\frac{1}{\tau_I} = \frac{N_I Z^2 e^4 m_c}{8\pi \hbar^3 \epsilon_s^2 K^3} \int_0^\pi \frac{\sin^3 \theta / 2 d(\sin \theta / 2)}{[\sin^2(\theta/2) + 1/b]^2} \quad (\text{A24})$$

Assuming $\sin(\theta/2) = x$, Eqn. (A24) becomes

$$\begin{aligned} \frac{1}{\tau_I} &= \frac{N_I Z^2 e^4 m_c}{8\pi \hbar^3 \epsilon_s^2 K^3} \int_0^1 \frac{x^3 dx}{(x^2 + b^{-1})^2} \\ &= \frac{N_I Z^2 e^4}{16\pi (2m_c)^{1/2} \epsilon_s^2 E^{3/2}} \left[\ln(1+b) - \frac{b}{1+b} \right] \end{aligned} \quad (\text{A25})$$

where $b = \frac{8m_c \epsilon_s kT}{\hbar^2 e^2 n^*}$ and n^* is the effective screen density which is approximately equal to free carrier concentration. The average relaxation time can be calculated by using the formula,

$$\langle \tau \rangle = \frac{\int_0^\infty \tau E^{3/2} e^{-E/kT} dE}{\int_0^\infty E^{3/2} e^{-E/kT} dE} \quad (\text{A26})$$

Then

$$\langle \tau_I \rangle = \frac{16\pi (2m_c^*)^{1/2} \epsilon_s^2 \int_0^\infty E^3 [\ln(1+b) - b/b+1]^{-1} e^{-E/kT} dE}{Z^2 e^4 N_I \int_0^\infty E^{3/2} e^{-E/kT} dE} \quad (\text{A27})$$

The logarithmic term varies slowly and it can be taken outside the integral by replacing E with $3kT$ as an approximation. In this way we obtain

$$\langle \tau_I \rangle = \frac{64\epsilon_s^2 (2\pi kT)^{3/2} m_c^{1/2}}{N_I Z^2 e^4} \left[\ln(1+b) - \frac{b}{1+b} \right]^{-1} \quad (\text{A28})$$

The mobility due to ionized impurity scattering is given by

$$\mu_I = \frac{e}{m_c} \langle \tau_I \rangle = \frac{64\epsilon_s^2 (2\pi kT)^{3/2}}{N_I Z^2 e^3 m_c^{1/2}} \left[\ln(1+b) - \frac{b}{1+b} \right]^{-1} \quad (\text{A29})$$

Taking $Z = 1$, $m_o = 9.11 \times 10^{-31}$ kg, $e = 1.6 \times 10^{-19}$ coul., $k = 1.38 \times 10^{-23}$ joule/K, Eqn. (A29) which is also called the Brooks-Herring equation⁽⁹¹⁾ can be expressed as

$$\mu_I = \frac{3.28 \times 10^{15} (m_o/m_c)^{1/2} \epsilon_r^2 T^{3/2}}{(N_A + N_D) \{ \ln(b+1) - [b/(b+1)] \}} \text{ cm}^2/\text{V}\cdot\text{sec} \quad (\text{A30})$$

$$b = \frac{1.29 \times 10^{14} (m_c/m_o) \epsilon_s T^2}{n^*} \quad (\text{A31})$$

In the Brooks-Herring theory, the Coulomb potential of the impurity centers is screened by free carriers and the dielectric response of the valence electrons is simply accounted for by the static dielectric constant of the medium ϵ_s . Attempts have been made⁽⁷⁸⁾ to improve the Brooks-Herring theory by including valence screening effects in addition to those represented by ϵ_s and values of mobility in anomaly with those predicted by the Brooks-Herring equation were obtained. However, a more recent analysis⁽⁷⁹⁾ shows that the difference is very small.

(II) Polar Optical Phonon Scattering

The transition probability for polar optical phonon scattering can be derived by evaluating the potential energy of the electron due to polarization and substituting into Eqn. (A11). Since this scattering mechanism consists of the absorption and emission of phonons, the initial and final energy states can be expressed as $E_1 = E_K + n_\xi h\omega_\xi$ and $E_2 = E_{K'} + (n_\xi \pm 1)h\omega_\xi$ where $n_\xi = (\exp(h\omega_\xi/kT) - 1)^{-1}$ is the number of phonons followed the Boltzmann distribution and $h\omega_\xi$ is the phonon energy with wave vector $q\xi$. Now the transition probability $P(K, K')$ is given by

$$P(K, K') = \frac{2\pi}{h} \cdot e^{\left(\frac{h\omega_\xi}{2V\epsilon_0} \frac{1}{1/K_\infty - 1/K_S}\right)} \frac{1}{\xi^2} (n_\xi \text{ or } n_\xi + 1) \cdot \Omega(E_1 - E_2) \quad (\text{A32})$$

where ω_ξ is the longitudinal optical phonon vibration frequency, V is the total volume of the crystal, ϵ_∞ is the material permittivity at very high frequency, ϵ_S is the static permittivity, $\xi = |K' - K|$ is the wave vector difference after scattering from K to K' . Substituting Eqn. (A32) into (A9), the relaxation time due to polar optical scattering is given by⁽⁹⁰⁾

$$\begin{aligned} \frac{1}{\tau_{po}} &= \frac{V}{(2\pi)^3} \cdot \frac{2\pi}{h} \cdot e^{\left(\frac{h\omega_\xi}{2V\epsilon_0} \frac{1}{1/K_\infty - 1/K_S}\right)} \cdot \\ &\cdot \int \frac{1}{\xi^2} [n_\xi \Omega(E_{K'}, -E_K - h\omega_\xi) + (n_\xi + 1) \Omega(E_{K'}, -E_K + h\omega_\xi)] \cdot \\ &\cdot \left(1 - \frac{K' \cos \theta'}{K \cos \theta}\right) d\xi \quad (\text{A32}) \end{aligned}$$

where the Ω function has been defined previously as

$$\Omega(x) = \sin \frac{xt}{\hbar} / \pi x$$

By assuming spherical constant energy surface, elastic scattering,

$$E = \hbar^2 k^2 / 2m_c \gg \hbar \omega_1, \text{ and using the integral } I = \int_{-\infty}^{\infty} (\sin y / y) dy = \pi,$$

Eqn. (A32) can be simplified to

$$\begin{aligned} \frac{1}{\tau_{po}} &= \frac{e^2 \omega_1}{4\pi \epsilon_0} \left(\frac{1}{K_\infty} - \frac{1}{K_s} \right) \frac{m_c}{\hbar^2 K'} \left[\frac{n_\xi + 1}{2K} \int_0^{2K} d\xi + \frac{n_\xi}{2K} \int_0^{2K} d\xi \right] \\ &= \frac{e^2 \omega_1}{4\sqrt{2} \cdot \pi \epsilon_0} \left(\frac{1}{K_\infty} - \frac{1}{K_s} \right) \frac{m_c^{1/2}}{\hbar E^{1/2}} (2n_\xi + 1) \end{aligned} \quad (\text{A33})$$

or

$$\frac{1}{\tau_{po}} = \frac{e^2 \omega_1}{4\sqrt{2} \pi \epsilon_0} \left(\frac{1}{K_\infty} - \frac{1}{K_s} \right) \frac{m_c^{1/2}}{\hbar E^{1/2}} \left(\frac{e^{\hbar \omega_1 / kT} + 1}{e^{\hbar \omega_1 / kT} + 1} \right) \quad (\text{A34})$$

Unless the temperature is very small, we may assume that $\hbar \omega_1 \ll kT$, then $e^{\hbar \omega_1 / kT} + 1 \approx 2$, then Eqn. (A34) becomes

$$\frac{1}{\tau_{po}} \approx \frac{e^2 \omega_1}{2\sqrt{2} \pi \epsilon_0} \left(\frac{1}{K_\infty} - \frac{1}{K_s} \right) \frac{m_c^{1/2}}{\hbar E^{1/2}} \frac{1}{e^{\hbar \omega_1 / kT} - 1} \quad (\text{A35})$$

By using Eqn. (A26), the average relaxation time is given by

$$\begin{aligned} \langle \tau_{po} \rangle &= \frac{2\sqrt{2} \pi \epsilon_0 \hbar}{e^2 \omega_1 m_c^{1/2} (1/K_\infty - 1/K_s)} \frac{\int_0^\infty E^2 e^{-E/kT} dE}{\int_0^\infty E^{3/2} e^{-E/kT} dE} \\ &= \frac{2\sqrt{2} \pi \epsilon_0 \hbar}{e^2 \omega_1 m_c^{1/2} (1/K_\infty - 1/K_s)} \frac{8(kT)^{1/2}}{3(\pi)} \\ &= \frac{16 \epsilon_0 \hbar (2kT\pi)^{1/2}}{3 e^2 m_c^{1/2} \omega_1 (1/K_\infty - 1/K_s)} \end{aligned} \quad (\text{A36})$$

The mobility due to polar optical scattering is given by

$$\mu_{po} = \frac{e\langle\tau_{po}\rangle}{m_c} = \frac{16\epsilon_0 \hbar (2kT\pi)^{1/2}}{3e\omega_1 m_c^{3/2} (1/K_\infty - 1/K_s)} \quad (A37)$$

Since the polar optical phonon scattering is neither randomizing nor elastic, strictly a relaxation time approximation cannot be made for this type of scattering. Fortini, et al.⁽⁹²⁾ derived μ_{po} differently by solving the Boltzmann transport equation and calculating current density. The formula of μ_{po} is essentially the same as Eqn. (A37) except a correction factor $G(\theta/T)$ ⁽⁹²⁾ which is nearly equal to unity at high temperature $kT \gg \hbar\omega_1$. Substituting the known values into Eqn. (A37), μ_{po} becomes

$$\mu_{po} = 25.44 \frac{K_s K_\infty}{K_s - K_\infty} \frac{\exp(\theta/T) - 1}{(m_c/m_o)^{3/2}} \frac{1}{\theta} G\left(\frac{\theta}{T}\right) T^{1/2} \quad (A38)$$

where $\theta = \hbar\omega_1/k$ is the optical phonon temperature.

(III) Alloy Scattering

The relaxation time due to alloy scattering has been determined by Hauser, et al.⁽⁹³⁾, which is

$$\frac{1}{\tau_a} = \frac{3\pi}{32\sqrt{2}} \frac{(m_c)^{3/2} a^3}{\hbar^4} (\Delta U)^2 E^{1/2} \quad (A39)$$

where a is the lattice constant, ΔU is the alloy scattering potential.

The average relaxation calculated by using Eqn. (A26) is given by

$$\begin{aligned}
\langle \tau_a \rangle &= \frac{32\sqrt{2} \hbar^4}{3\pi m_c^{3/2}} \cdot \frac{1}{a^3} \frac{\int_0^\infty E e^{-E/kT} dE}{(\Delta U)^2 \int_0^\infty E^{3/2} e^{-E/kT} dE} \\
&= \frac{128\sqrt{2} \hbar^4}{9\pi m_c^{3/2}} \frac{1}{a^3 (kT)^{1/2} (\Delta U)^2} \quad (A40)
\end{aligned}$$

Thus the mobility due to alloy scattering is given by

$$\mu_a = \frac{128\sqrt{2} e \hbar^4}{9\pi k^{1/2}} \frac{1}{a^3 (m_c)^{5/2} (\Delta U)^2 T^{1/2}} \quad (A41)$$

or

$$\mu_a = \frac{9.43 \times 10^3 T^{-1/2}}{(m_c/m_o)^{5/2} (\Delta U)^2 a^3} \quad (A42)$$

The lattice constant, a , is estimated for the quaternaries in the present investigation by the equation⁽⁹⁴⁾

$$a_{x,y}^o (\text{Å}) = 5.87 + 0.18x - 0.42y + 0.02xy \quad (A43)$$

(IV) Acoustic Phonon Scattering

The relaxation time due to longitudinal acoustic phonon scattering can be derived similarly as that of polar optical phonon scattering process. The mobility limited by this mechanism can be expressed as⁽⁹⁵⁾

$$DP = \frac{3.17 \times 10^{-5} \rho_d U_1^2 T^{-3/2}}{E_{DP}^2 (m_c/m_o)^{5/2}} \quad (A44)$$

where E_{DP} (eV) is the acoustic deformation potential, U_1 is the longitudinal sound velocity, and ρ_d is the density of the material.

(V) Piezoelectric Scattering

In crystals having no inversion symmetry the displacements of the atoms associated with the acoustic waves produce an electric field. Electrons can interact with the lattice through this field. The phonons involved in piezoelectric scattering are the same as those involved in the acoustic phonon scattering. The relaxation time can be derived similarly and the mobility due to piezoelectric scattering can be expressed as⁽⁹⁶⁾

$$\mu_{pE} = \frac{2.52 \times 10^{12} T^{-1/2}}{(m_c/m_o)^{3/2} h_{14}^2 [(4/c_t + (3/c_l))]} \quad (A45)$$

with

$$h_{14} = e_{14}/\epsilon_s \epsilon_o$$

where e_{14} is defined as the piezoelectric constant and c_t and c_l are, respectively, the transverse and longitudinal elastic constants.

(VI) Space Charge Scattering

The space charge scattering mechanism particularly limits the carrier mobilities at high temperatures. From the formulation by Weisberg⁽⁹⁷⁾, the temperature dependence of the mobility can be expressed as

$$\mu_{SC} = \frac{3.2 \times 10^4 T^{-1/2}}{(m_c/m_o)^{1/2} (N_s \cdot A_s)} \quad (A46)$$

where N_s and A_s are, respectively, the concentration and area of the scattering centers.

The material parameters of binary compounds which were used in the interpolation scheme⁽¹⁵⁾ are listed in Table A.1.

Table A.1. The Parameters of Binary Compounds

	InP	GaP	GaAs	InAs
Static permittivity, ϵ_s	12.35	11.10	12.9	14.55
Dynamic permittivity, ϵ_d	9.52	8.90	10.90	11.80
Optical phonon temperature, θ	501	580	420	350
Density, ρ_d (gm/cm ²)	4.83	4.13	5.37	5.71
Sound velocity, U_1 (km/sec)	5.16	6.28	5.24	4.28
Deformation potential, E_{DP} (eV)	6.5	13	8.6	4.9
Piezoelectric constant, e_{14} (coul/m ²)	0.035	-0.1	0.16	0.045
Elastic constant, C_{11} (dynes/cm ²)	1.022E+12	1.412E+12	1.188E+12	0.865E+12
C_{12}	0.576E+12	0.025E+12	0.538E+12	0.485E+12
C_{14}	0.460E+12	0.705E+12	0.594E+12	0.396E+12

APPENDIX B

ELECTRON EFFECTIVE MASSES IN $\text{Ga}_{1-x}\text{Al}_x\text{As}$

The variation of the effective masses in $\text{Ga}_{1-x}\text{Al}_x\text{As}$ with Al compositions can be calculated from $\vec{K} \cdot \vec{P}$ theory according to Aspnes⁽⁹⁸⁾.

In the Γ conduction-band minimum,

$$\frac{m_0}{m_{\Gamma}^*} = 1 + 7.51 \left[\frac{2}{E_{\Gamma}} + \frac{1}{E_{\Gamma} + 0.341} \right] \quad (\text{B1})$$

where E_{Γ} is the energy of Γ minimum with respect to the valence-band maximum.

In the L conduction-band minima,

$$\frac{m_0}{m_{tL}^*} = 1 + 19.3 \left[\frac{1}{E_L} + \frac{1}{E_L + 0.22} \right] \quad (\text{B2})$$

where m_{tL}^* is the transverse effective mass of electron in the L minima, E_L is the energy of L minima with respect to the valence-band maximum. The longitudinal effective mass of electron, $m_{\ell L}^*$, in the L minima is equal to $1.9 m_0$, then the electron density-of-state effective mass in the L minima is given by

$$m_L^* = M_c^{2/3} \cdot m_{\ell L}^{2/3} m_{tL}^{1/3} \quad (\text{B3})$$

where M_c is the number of equivalent minima in the L valley. In X conduction-band minima, the electron density-of-state effective mass keeps constant and is given by

$$m_X^* = 0.85 m_0 \quad (B4)$$

The variation of the different electron effective masses with Al composition is shown in Figure B.1.

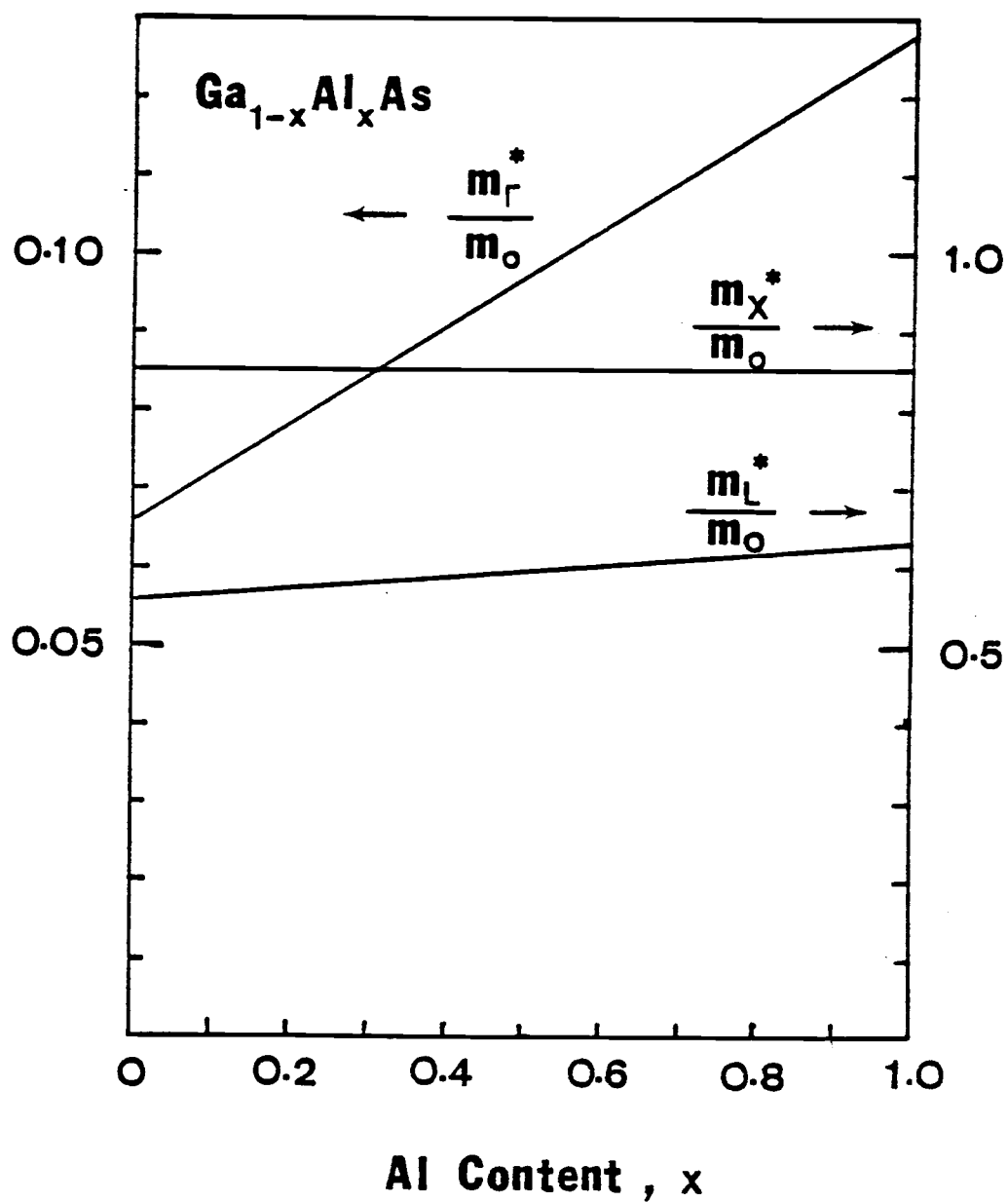


Figure B.1. Variation of electron effective mass with Al content in the conduction minima of Ga_{1-x}Al_xAs.

APPENDIX C

COMPUTER PROGRAM

- (I) Program for Mobility Data Analysis
- (II) Program for Lucovsky's Model
- (III) Program for Huang and Rhys Model

Computer Program for Mobility Analysis

```

PROGRAM MOB(INPUT,OUTPUT,TAPE5=INPUT,TAPE6=OUTPUT)
C  IN THIS PROGRAM WE DEFINE INP=1,GAP=2,GAAS=3,INAS=4
    DIMENSION A(10,4),M(8),B(4),C(12),U(12,8),D(19),G(19),Z(10),W(10)
    DATA ((A(I,J),J=1,4),I=1,10)/12.35, 11.10, 12.9, 14.55,
1     9.52,      8.90,      10.90,      11.80,
2     501.,      580.,      420.,      350.,
3     4.83,      4.13,      5.37,      5.71,
4     5.16,      6.28,      5.24,      4.28,
5     6.5,       13.0,      8.6,      4.9,
6     0.035,     -0.10,     0.16,     0.045,
7     1.022E+12, 1.412E+12, 1.188E+12, 0.865E+12,
8     0.576E+12, 0.625E+12, 0.538E+12, 0.485E+12,
9     0.460E+12, 0.705E+12, 0.594E+12, 0.396E+12/
    DATA M/1,2,4,3,2,3,1,4/
    DATA D/0.2, 0.3, 0.4, 0.5, 0.6, 0.7, 0.8, 0.9, 1.0, 1.1, 1.2,
1     1.4, 1.5, 2.0, 2.5, 3.0, 3.5, 4.0, 4.5/
    DATA G/ 0.8387, 0.7902, 0.7520, 0.7226,
1     0.7008, 0.6861, 0.6776, 0.6748,
2     0.6770, 0.6837, 0.6943, 0.7258,
3     0.7458, 0.8752, 1.0321, 1.1908,
4     1.3484, 1.4926, 1.6173/
    DATA Z/ 0.13779,0.72945,1.80834,3.40143,5.55249,
1     8.33015,11.84378,16.27925,21.99658,29.92069/
    DATA W/ 3.0844E-01,4.0111E-01,2.1806E-01,6.2087E-02,
1     9.5015E-03,7.5300E-04,2.8259E-05,4.2493E-07,
1     1.8395E-09,9.9118E-13/
1 READ(5,2)X,Y,X1,X2,X3,X5
2 FORMAT(2F6.4,2X,EB.2,2X,F4.2,2X,EB.2,2X,F6.4)
   DO 20 I=1,2
   DO 10 J=1,4
   L=2*(J-1)+1
   K=L+1
   XA=X
   IF(J.GT.2)XA=Y
   B(J)=(1.0-XA)*(A(I,M(L))-1.0)/(A(I,M(L))+2.0)+XA*(A(I,M(K))-1.0)/(A(I
1(I,M(K))+2.0)
10 B(J)=(1.0+2.0*B(J))/(1.0-B(J))
20 C(I)=(X*(1.0-X)*((1.0-Y)*B(1)+Y*B(2))+Y*(1.0-Y)*((1.0-X)*B(4)+X*B(
13)))/(X*(1.0-X)+Y*(1.0-Y))
   DO 40 I=3,10
   DO 30 J=1,4
   L=2*(J-1)+1
   K=L+1
   XA=X
   IF(J.GT.2)XA=Y
30 B(J)=(1.0-XA)*A(I,M(L))+XA*A(I,M(K))

```

```

40 C(I)=(X*(1.0-X)*((1.0-Y)*B(1)+Y*B(2))+Y*(1.0-Y)*((1.0-X)*B(4)+X*B(
13)))/(X*(1.0-X)+Y*(1.0-Y))
C(11)=0.08-0.039*Y
C(12)=0.1894*Y-0.4184*X+0.0130*X*Y+5.8696
WRITE(6,41)X,Y
41 FORMAT(1X,"THE COMPOSITION IS X = ",F5.3,5X,"Y = ",F5.3)
WRITE(6,43)(C(I),I=1,12)
43 FORMAT (1X,E12.3)
WRITE(6,46)
46 FORMAT(/3X,"UI",8X,"UA",5X,"UPO",6X,"UDP",6X,"UPE",6X,"USC",6X,"UI
1N",7X,"UT")
DO 200 I=1,12
T=50.+50.*I
P=(1.29E-2)*C(11)*C(1)*T**2.
U(I,1)=(3.28E+15)*(C(11)**(-0.5)*C(1)**2.)*T**1.5
Q=P+1.
R=X1*(ALOG(Q)-(P/Q))
U(I,1)=U(I,1)/R
U(I,2)=(9.43E+3)*(T**(-0.5))/(C(11)**2.5*(X2**2.*(C(12)**3)))
S=C(3)/T
DO 50 K=1,19
50 IF(S.LT.D(K))GO TO 60
IF(S.EQ.D(K))GO TO 70
GO TO 80
60 CONTINUE
70 E=G(K)
GO TO 90
80 L=K-1
E=G(K)+(S-D(K))*(G(K)-G(L))/(D(K)-D(L))
90 CE=C(1)*C(2)/(C(1)-C(2))
U(I,3)=25.44*CE*E*(EXP(S)-1.0)*(T**0.5)/(C(3)*C(1)**1.5)
U(I,4)=(3.17E+5)*C(4)*(C(5)**2.)*(T**(-1.5))/(C(6)**2.*C(11)**2.5)
H14=C(7)/(C(1)*8.854E-12)
CT=0.2*(C(8)+3.*C(10)-C(9))
CL=0.2*(3.*C(8)+2.*C(9)+4.*C(10))
CTL=4./CT+3./CL
U(I,5)=(2.52E+12)*(T**(-0.5))/(C(11)**1.5*(H14**2.)*CTL)
U(I,6)=(3.2E+9)*(T**(-0.5))/(C(11)**0.5)*X3)
GO TO 150
TS=0.8*S
XM=TS+(1.16E+04)*(-X5)/T
XN=-TS+(1.16E+04)*(-X5)/T
FT1=0.
FT2=0.
F1=0.
F2=0.

```

```

DO 120 J=1,10
ZI=Z(J)-XM
ZK=Z(J)-XM
F1=(ZI**1.5*(EXP(TS)-1.0))/((EXP(TS)*(ZI+XM)**0.5))
F2=(ZK**1.5*(EXP(TS)-1.0))/(ZK+XM)**0.5
F1=U(J)*F1
FT1=FT1+F1
F2=U(J)*F2
FT2=FT2+F2
120 CONTINUE
U7=428.*FT1
U8=428.*FT2
U(I,7)=U7*U8/(U7+U8)
150 U(I,8)=1.0/U(I,1)+1.0/U(I,2)+1.0/U(I,3)+1.0/U(I,4)
+1.0/U(I,5)+1.0/U(I,6)
U(I,8)=1.0/U(I,8)
200 WRITE(6,300)(U(I,J),J=1,8)
300 FORMAT(7E9.3,F7.1)
GO TO 1
END

```

? 0.257 0.595 4.00E+16 0.75 2.70E+04 0.7000

THE COMPOSITION IS X = .257 Y = .595

.132E+02
.106E+02
.430E+03
.523E+01
.490E+01
.679E+01
.445E-01
.102E+13
.535E+12
.478E+12
.568E-01
.588E+01

UI	UA	UPO	UDP	UPE	USC	UIN	UT	
.167E+05	.107E+05	.277E+06	.112E+07	.998E+07	.497E+05	-I 5633.5	100	°C
.252E+05	.877E+04	.569E+05	.611E+06	.815E+07	.406E+05	-I 5058.6	150	
.343E+05	.760E+04	.261E+05	.397E+06	.706E+07	.352E+05	-I 4343.0	200	
.440E+05	.680E+04	.149E+05	.284E+06	.631E+07	.315E+05	-I 3672.1	250	
.542E+05	.620E+04	.971E+04	.216E+06	.576E+07	.287E+05	-I 3102.8	300	
.648E+05	.574E+04	.772E+04	.171E+06	.534E+07	.266E+05	-I 2757.4	350	
.758E+05	.537E+04	.621E+04	.140E+06	.499E+07	.249E+05	-I 2452.0	400	
.873E+05	.507E+04	.541E+04	.118E+06	.471E+07	.234E+05	-I 2246.6	450	
.990E+05	.481E+04	.484E+04	.100E+06	.446E+07	.222E+05	-I 2083.8	500	
.111E+06	.458E+04	.443E+04	.870E+05	.426E+07	.212E+05	-I 1954.4	550	
.124E+06	.439E+04	.409E+04	.764E+05	.408E+07	.203E+05	-I 1841.7	600	
.136E+06	.421E+04	.386E+04	.677E+05	.392E+07	.195E+05	-I 1754.7	650	

Computer Program for Lucovsky's Model

```

10  REM PHOTO-IONIZATION CROSS SECTION*** JOSEPH KU, 1-1-81
20  PRINT "THIS PROGRAM IS TO SIMULATE THE LUCOVSKY MODEL OF"
30  PRINT "THE PHOTO-IONIZATION CROSS-SECTION OF DX CENTER IN"
40  PRINT "GaAlAs MATERIAL."
50  OPTION BASE 1
60  DIM X(9),Y(9),Z(9)
70  INPUT "PLEASE ENTER THE TRAP ENERGY LEVEL",E
80  INPUT "PLEASE ENTER THE COMPOSITION OF ALUMINUM",C
90  INPUT "PLEASE ENTER THE EFFECTIVE MASS",A
100 INPUT "PLEASE ENTER THE BOUND ELECTRON MASS",B
110 FOR I=1 TO 9
120 X(I)=.7+.1*I
130 Y(I)=E.5*C(X(I)-E) 1.5/C(X(I)*(X(I)+E*(B/A-1)).5)
140 NEXT I
150 S=Y(9)
160 FOR J=1 TO 9
170 IF Y(J)<S THEN GOTO 190
180 S=Y(J)
190 NEXT J
200 FOR I=1 TO 9
210 Z(I)=Y(I)/S
220 NEXT I
230 PRINT "THE TRAP ENERGY LEVEL",E
240 PRINT "THE ALUMINUM COMPOSITION",C
250 PRINT "THE EFFECTIVE MASS",A
260 PRINT "THE BOUND ELECTRON MASS",B
270 PRINT "PHOTON ENERGY (eV)", "PHOTO-IONIZATION CROSS SECTION"
280 FOR I=1 TO 9
290 PRINT "      ";X(I);"          ";Z(I)
300 NEXT I
310 PRINT "PRINTER IS @
320 END

```

THE TRAP ENERGY LEVEL	.72
THE ALUMINUM COMPOSITION	.32
THE EFFECTIVE MASS	.58
THE BOUND ELECTRON MASS	1
PHOTON ENERGY (eV)	PHOTO-IONIZATION CROSS SECTION
.8	.141293642331
.9	.366335411464
1	.558334761449
1.1	.706555185716
1.2	.815755639219
1.3	.893368164804
1.4	.946328121355
1.5	.980364653913
1.6	1

Computer Program for Huang & Rhys Model

```

10  REM ***PHOTO-IONIZATION CROSS SECTION*** JOSEPH KU, 1/7/81
20  PRINT "THIS PROGRAM IS USING THE GAUSS-LAQUERE QUADRATURE METHOD"
30  PRINT "TO SIMULATE THE HUANG-RHYS MODEL OF THE PHOTOIONIZATION "
40  PRINT "CROSS SECTION OF DX CENTER IN THE GaAlAs MATERIAL."
50  OPTION BASE 1
60  DIM Ehw(9),Sigma(9),Z(5),W(5),F(5),E(9)
70  C(1)=.26356
80  C(2)=1.41340
90  C(3)=3.59642
100 C(4)=7.08581
110 C(5)=12.6408
120 W(1)=.52176
130 W(2)=.39367
140 W(3)=.07524
150 W(4)=3.31176E-3
160 W(5)=2.337E-5
170 INPUT "PLEASE ENTER THE ALUMINUM COMPOSITION",Wc
180 INPUT "PLEASE ENTER THE ENERGY GAP",Eg
190 INPUT "PLEASE ENTER THE TEMPERATURE",T
200 INPUT "PLEASE ENTER THE FREE ELECTRON FERMI ENERGY",Ef
210 INPUT "PLEASE ENTER THE Penn. GAP",Ea
220 INPUT "PLEASE ENTER THE PHONON ENERGY ",Eph
230 INPUT "PLEASE ENTER THE THERMAL DEPTH",Eo
240 INPUT "PLEASE ENTER THE FRANCK-CONDON SKIFT",Dfc
250 FOR I=1 TO 9
260 Ehw(I)=.6+.1*I
270 Sig=0
280 FOR J=1 TO 5
290 A=EXP(-2+Z(J)/Ea)
300 B=Eo+Dfc+Z(J)
310 C=Eo+Dfc-Z(J)-(Eg+Ea)/2
320 P=Eph/(2*T+.62E-5)
330 Tanh=(EXP(S)-EXP(-S))/(EXP(S)+EXP(-S))
340 U=2-Dfc+Eph/Tanh
350 U1=(Ehw(I)-(Eo+Dfc+Z(J))/2)/U
360 S1=(1-A*(Z(J)^.5)*B+C1+A*(Efc^5)*C1)^2
370 F(I,J)=EXP(Z(J))*(Z(J)^.5)*S1*(U+(-.5)+EXP(-U))
380 Sig=Sig+W(I)*F(I)
390 NEXT J
400 Sigma(I)=Sig/Ehw(I)
410 NEXT I
420 FOR I=1 TO 9
430 PRINT "SIGMA",Sigma(I)
440 IF I=9 THEN GOTO 460
450 D=Sigma(I)
460

```

```

460 NEXT I
470 FOR I=1 TO 9
480 ECI=SigmaI/D
490 NEXT I
500 PRINT "THE ALUMINUM COMPOSITION",Xc
510 PRINT "THE ENERGY GAP",Eg
520 PRINT "THE TEMPERATURE",T
530 PRINT "THE THERMAL DEPTH",Eo
540 PRINT "THE FRANCK-CONDON SHIFT",Dfc
541 PRINT
550 PRINT "THE PHOTON ENERGY (eV)", "PHOTO-IONIZATION CROSS SECTION"
560 PRINT
570 FOR I=1 TO 9
580 PRINT "          ";Eh(I);"          ";ECI
590 NEXT I
600 PRINTER IS 0
610 END

```

```

SIGMA          1.90300655800E-04
SIGMA          6.38079809220E-03
SIGMA          .106862553506
SIGMA          .890938092037
SIGMA          3.68901750538
SIGMA          7.57276416263
SIGMA          7.69663702031
SIGMA          3.86902380127
SIGMA          .9611688051

```

```

THE ALUMINUM COMPOSITION          .37
THE ENERGY GAP                    1.92
THE TEMPERATURE                    90
THE THERMAL DEPTH                  .2
THE FRANCK-CONDON SHIFT            .8

```

```

THE PHOTON ENERGY (eV)          PHOTO-IONIZATION CROSS SECTION
.7                                2.47251696160E-05
.8                                8.29037159392E-04
.9                                1.38843176863E-02
1                                  .115756802573
1.1                                .479302518184
1.2                                .983905586641
1.3                                1
1.4                                .502690177679
1.5                                .124881659686

```